Effect of H-ZSM-5 acidity in methanol-to-olefins conversion

Beatriz Estevens Castelo Branco

Thesis to obtain the Master of Science Degree in

Chemical Engineering

Supervisors:

Professor Doctor Maria Filipa Gomes Ribeiro (IST)

Engineer Marie-Elisabeth Lissens (UGent)

Examination Committee

Chairperson: Professor Doctor Sebastião Manuel Alves

Supervisor: Engineer Marie-Elisabeth Lissens

Members of the Committee: Professor Doctor João Miguel Alves da Silva

October 2021

This master thesis was performed in collaboration with

Declaration

I declare that this document is an original work of my own authorship, except where otherwise indicated and properly referenced, fulfilling all the requirements of the Code of Conduct and Good Practices of the University of Lisbon.

Furthermore,

I, Beatriz Estevens Castelo Branco, student number 96955 at the Instituto Superior Técnico, author of the dissertation for obtaining the Master's Degree on Chemical Engineering, with the title Effect of zeolite acidity and topology in methanol-to-olefins conversion, grant Instituto Superior Técnico a perpetual license, not exclusively for, to use this dissertation for teaching or research purposes and I authorize its publishing, as well as its extended summary, on the website www.tecnico.ulisboa.pt in pdf. Format, in order to allow its dissemination to all who access that page, and, with the same purpose of dissemination, to respond favourably to requests from educational or research institutions and Documentation Centres or Libraries, referring them to those same files in pdf. format but making an express mention, either on its website or when referring back, to the obligation of those who access the present dissertation and its respective extended summary to safeguard my copyright on these documents, which are conferred on me by the Copyright Code and the Related Rights Code.

Lisbon, October 28th, 2021

Student nº 96955

Beatriz Estevens Castelo Branco

Acknowledgements

To my supervisors, Prof. Doctor Filipa Ribeiro and Eng. Marie-Elisabeth Lissens, for the vote of confidence to perform my studies abroad, for receiving me and supporting right from the start. For all the knowledge shared, availability and patience throughout every trial, dedication, freedom, and guidance that allowed me to reach further.

To Dr. Prof. Pedro Mendes, for all the time spent teaching everything he could, for facing with me all adversities found throughout this work, for all the effort, for tirelessly giving me feedback and helping me feel supported throughout all this. A big thank you for all the support beyond the scope of this work and for the chapters that come next.

I would also like to thank my dear co-workers. Maria Herrero, Geovani de Freitas, and Nebojsa Korica. For your friendship and for your and availability for helping me with anything I needed. To Ilaria and Arij, my laboratory mates, for your friendship, support and time spent together. Thank you for bringing a sense of home to the place where I worked.

A thank you to every Professor, Doctor, person, in IST and UGent, that helped achieve this work. Being able to work with you all was the best experience I could have imagined.

To my closest and dearest and loved ones, there is not enough space to express my gratitude.

To my mother, Skellington, Rafael, and Sara. Although far away, there was not a second that my heart was not with you. Thank you for making me feel loved even at a great distance, for all the long calls, the visits, the trust, and for granting me your support and presence in this great journey. Thank you for helping me in every way you could when I returned, for keeping me sane. For all the prepared meals, coffees, advice, patience and help in my darkest hours. For all the understanding for putting plans on-hold for the next week, every week. Your love moved me the entire time, and so it will continue to. To my father, whom I know would be proud.

Abstract

From environmental awareness to the energetic transition, nowadays society faces one of its biggest challenges in order to prosper in a sustainable path. Methanol-to-olefins process arises with the promise of a circular economy and carbon neutrality in the battle against fossil fuels in the propylene market. With increasing projects on green methanol pathways, it is essential to study and optimize this industrial technology in terms of reaction conditions, kinetics, and catalyst design to maximize propylene yielding.

The present work studied the effect of acidity in commercial H-ZSM-5 catalysts (Si/Al of 25, 40 and 140) in the reaction pathways of MTO within the dual-cycle mechanism concept. Elemental, textural, and acidic properties were investigated. Catalytic studies were carried out at constant 0.4 bar methanol partial pressure, steady-state, and under intrinsic kinetic regimes, between 350-450º C on an isothermal tubular reactor.

Increasing temperature favoured higher propylene yields by promotion of the alkene cycle up to 375º C. At higher temperatures, the effect of acidity was manifested through the increasing promotion of the aromatic cycle due to the decrease in $Brønsted_{strong}/Lewis_{total}$ acid sites ratio. A maximum of contribution of the aromatic cycle was determined to occur in a catalyst with a Si/Al ratio between 40 and 140. Lewis acid sites were linked to the stabilization of poly-aromatic intermediate species and to higher apparent activation energies, which established MTO as a two-site reaction mechanism kinetics. Catalysts with lower acid site density, higher relative mesopore volume, and higher external surface area presented lower deactivation rates and improved propylene yields. H-ZSM-5 with Si/Al of 140 displayed the best performance with a good propylene maximization and a high catalytic lifetime. Future studies on the effect of acidity should aim to validate these results through more studies (H-ZSM-5 with Si/Al ratios above 100).

Keywords: methanol-to-olefins; MTO; intrinsic kinetics; steady-state; H-ZSM-5; acidity; Brønsted; Lewis.

Resumo

Da consciência ambiental à transição energética, hoje em dia a sociedade enfrenta um dos seus maiores desafios a fim de prosperar num caminho sustentável. Com o fim de travar a batalha contra os combustíveis fósseis no mercado de propileno, surge o processo metanol-para-olefinas (MTO). Este apresenta-se como uma promissora forma de criar uma economia circular e de alcançar a neutralidade de carbono. Assim sendo, e a par do aumento de projetos no âmbito de produção de metanol através de vias verdes, é essencial estudar e otimizar esta tecnologia industrial em termos de condições de reação, cinética e de conceção de catalisadores que potenciem a produção de propileno.

O presente trabalho estudou o efeito da acidez nos catalisadores comerciais H-ZSM-5 (Si/Al de 25, 40 e 140) nas vias reacionais de MTO na extensão do conceito do mecanismo de ciclo-duplo. Foram investigadas as propriedades elementares, textuais e ácidas dos catalisadores. Desta forma, realizaram-se estudos catalíticos a uma pressão parcial constante de metanol de 0,4 bar, em estado estacionário, e sob um regime de cinética intrínseca, entre 350-450º C, num reator tubular isotérmico.

O aumento da temperatura proporcionou um aumento da produção de propileno favorecimento do ciclo alceno até aos 375º C. A temperaturas superiores, devido à diminuição de centros ácidos de Brønsted/Lewis do catalisador, os efeitos da acidez manifestaram-se através do aumento da promoção do ciclo aromático e tornaram-se predominantes. A máxima contribuição deste mesmo ciclo foi projetada para um catalisador com uma razão Si/Al entre 40 e 140. Os centros ácidos de Lewis, uma vez correlacionados com a estabilização de espécies poliaromáticas intermediárias assim como com energias de ativação aparente superiores, permitem chegar à conclusão de que a MTO segue uma cinética de reação com dois centros ativos. Foi verificado que catalisadores com menor densidade de centros ácidos, maior volume mesoporoso relativo e maior área superficial externa, conseguem alcançar uma menor velocidade de desativação e uma melhoria de rendimento de propileno. Estudos futuros sobre o efeito da acidez deverão validar estes resultados através da continuação destes estudos com H-ZSM-5 (com razões Si/Al superiores a 100) e com o desenvolvimento de um modelo cinético fiável.

Palavras-chave: metanol-para-olefinas; MTO; cinética intrínseca, estado estacionário; H-ZSM-5; acidez; Brønsted; Lewis.

Table of Contents

List of Tables

List of Figures

Nomenclature

Abbreviations

A/A	**Yield ratio between alkane and alkene hydrocarbons**
ACN	Acrylonitrile
AL_{EF}	Extra-framework aluminium
AL_{F}	Framework aluminium
BAS	**Brønsted acid site(s)**
BET	Brunauer, Emmett, Teller
Bz	Benzene
C_1	**Hydrocarbon with 1 carbon in its structure**
C_2	Ethylene and ethane
$C_{2=}$	Ethylene
C_3	Propylene and propane
$C_{3=}$	Propylene
C_4	Hydrocarbon with 4 carbons in its structure
C_{4-5}	Sum of hydrocarbons with 4 and 5 carbons in their structure
C_{i-j}	Sum of hydrocarbons with i to j carbons in their structure ($i<j$ and $i,j \in N_1$)
C_i	Hydrocarbon with i carbons in its structure ($i \in N_1$)
C_x	Olefins with x carbons in its structure ($i \in N_1$)
C-C	Carbon-carbon
CAGR	Compound annual growth rate
CO	Carbon monoxide
CO_2	Carbon dioxide
CTO	Coal-to-olefins
DICP	**Dalian Institute of Chemical Physics**
diMCP+	Dimethylcyclopentenyl cation
DME	Dimethyl ether
DMTO-I/II/III	Dimethyl ether/methanol-to-olefins -I/II/III process
E/2MB	**Yield ratio between ethylene and 2-methylbutane + 2-methyl-2-butene**

E/Isob	Yield ratio between ethylene and isobutane
EU	European Union
FCC	**Fluidized catalytic cracking**
FID	Flame ionization detector
FMTP	Fluidized bed-methanol-to-propylene process
FTIR	Fourier Transform Infrared Spectroscopy
GC	**Gas chromatography**
GHG	Greenhouse gas
HCP	**Hydrocarbon pool**
HMMC	1,2,3,3, 4,5-hexamethyl-6-methylene-1,4-cyclohexadiene
hexaMB or HMB	Hexamethylbenzenes
hexaMB+	Hexamethylbenzenium cation
hexaMB	Heptamethylbenzenes
heptaMB+ or 7MB+	Heptamethylbenzenium cation
Honeywell UOP	Honeywell Universal Oil Products
HTK	High throughput kinetic
HVC	High value compounds
Isob/E	**Yield ratio between isobutane and ethylene**
ICP-OES	Inductively coupled plasma - optical emission spectrometry
ktpa	**kilo tonnes per annum**
LAS	**Lewis acid site(s)**
MB	**Methylbenzenes**
MeOH	Methanol
MOGD	Methanol-to-olefin-to-gasoline and distillate process
MTG	Methanol-to-gasoline
MTH	Methanol-to-hydrocarbons
mtpa	million tonnes per annum
MTO	Methanol-to-olefins
MTP	Methanol-to-propylene
NH_3-TPD	**Ammonia temperature-programmed desorption analysis**
OCP	**Olefin cracking process**
PBR	**Packed bed tubular reactor**

pentaMB	Pentamethylbenzenes
PDH	Propane dehydrogenation
PO	Propylene oxide
polyMB	Polymethylbenzes
PP	Polypropylene
Py-FTIR	Pyrdidine Fourier Transform Infrared Spectroscopy
SASOL	**South African Synthetic Oil Limited**
Si/Al	Silicon to aluminium molar ratio
S(25/40/140)	H-ZSM-5 samples used during the present work with Si/Al of 25, 40, and 140
TAS	**Total acid sites**
tetraMB	Tetramethylbenzenes
triMB	Trimethylbenzenes
triMCP+	trimethylcyclopentenyl cation
USD	**United States Dollar**
XRD	**X-ray diffraction**

Mathematical Notation

$\boldsymbol{F_{DME}}$	**Molar flow of DME in the effluent**
$E_{A,app}$	Apparent activation energy
F_{DME}	Molar flow of DME in the effluent
F_k	Molar flow rate for the hydrocarbon species k in the effluent
F_{MeOH}	Molar flow of methanol in the effluent
F_{MeOH}^0	Molar flow of methanol in the feed
$\boldsymbol{k_0}$	**Pre-exponential factor**
k_{app}	Apparent reaction rate constant
$\boldsymbol{M_{DME}}$	**DME molar mass**
M_k	Molar mass of species k
M_{MeOH}	Methanol molar mass
M_O	Oxygen atomic molar mass

$\dot{m}_{H_2O}$	Mass flowrate of water in the effluent
$\dot{m}^0_{MeOH}$	Mass flowrate of methanol in the feed
$\boldsymbol{nC_k}$	**Number of carbon atoms for the hydrocarbon species k in the effluent**
$\boldsymbol{O^{in}}$	**Number of oxygen atoms in the feed**
O^{out}	Number of oxygen atoms in the effluent
O^{out}_{DME}	Number of oxygen atoms in DME in the effluent
$O^{out}_{H_2O}$	Number of oxygen atoms in water in the effluent
O^{out}_{MeOH}	Number of oxygen atoms in methanol in the effluent
$\boldsymbol{P_{MeOH}}$	**Methanol partial pressure**
P^0_{MeOH}	Methanol partial pressure in the feed
$\boldsymbol{R}$	**Perfect gas constant**
$-r_{MeOH}$	Observed reaction rate of product formation as a measure reactant change
$\boldsymbol{T}$	**Temperature**
TOF	Turn over frequency
TOS	Time on stream
$\boldsymbol{W}$	**Catalyst mass in the reactor**
W/F	Space-time
$WHSV$	Weight hourly space velocity
W/W	Contact time
$\boldsymbol{x_i}$	**Mass fraction of component i**
x^*_{DME}	Corrected mass fraction (with Dietz et al. correction factors) of species DME
x^*_k	Corrected mass fraction (with Dietz et al. correction factors) of species k
x^*_{MeOH}	Corrected mass fraction (with Dietz et al. correction factors) of species methanol
X_{oxy}	Oxygenate (methanol and DME) conversion
ε_{BAS}	Molar extinction coefficient for BAS
ε_{LAS}	Molar extinction coefficient for LAS

1 *Introduction*

In 2020, the European Commission set the target goal of reducing 60% of carbon dioxide (CO_2) emissions (with respect to the approximately 5 720 million metric tons of CO_2 equivalents registered in 1990 in the EU space alone) by 2030 and voted in favour of the law of Carbon Neutrality for each member state by 2050 **[1]**. Data shows that, on average, the "Sector of Energy Resources and Coupled Industries" is responsible for almost 79% of the global greenhouse gas (GHG) emissions **[2]**, where the cement industry alone is responsible for 8% of the total **[3]**. This industry is of extraordinary relevance when discussing the future of environmentally sustainable alternatives to fossil fuels since it is the most carbon-intensive industry, with the process emissions accounting for over 50% of the global CO_2 emissions **[3]**. Moreover, the European Cement Association set the objective of reducing 80% of this number by 2050 or even achieving carbon neutrality, as foreseen by the European Green Deal which provides major economic incentives for projects with these guidelines in mind, **figure 1 [3,4]**. The critical approach of EU relies on a swift and targeted, change on how resources are exploited and discarded. The sectors of chemicals and energetic production are faced with the opportunity and challenge to incorporate the principles of circular economy and turn pollution into a new raw material as the current society is heavily dependent on primary sources of feedstock, namely fossil fuels.

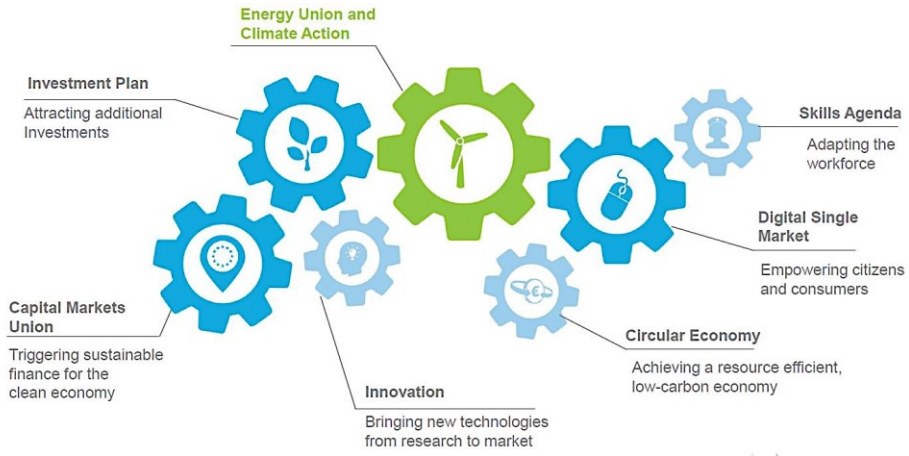

Figure 1 – EU approach on economic modernisation and climate action for the next decades [5].

Research suggests oil and natural gas reserves to last 50 more years and coal reserves to last up to 90 years as a result from the distressing increase of exploration of natural resources – with a global demand expected to keep rising 1.3% every year through 2040 with China and India leading this growth **[6,7,8].** This data is particularly alarming since coal exploration is the most pollutant source of energy in terms of stack gases and less pollutant resources, such as natural gas, raise several environmental risks regarding leaks during the extraction processes (with 34 times stronger greenhouse effect than CO_2) **[9,10]**.

Plastics is one of the biggest fossil fuel derivative markets and is expected to grow at a rate of 3.2% annually for the next decade, presently evaluated at over USD 568.9 billion (2019) and worth USD 1.2 trillion (2020) **[11,12]**. Polyolefins are the most common type of plastics (thermoplastics). This category of plastics includes polyethylene and polypropylene, the most ubiquitous plastics, obtained through polymerization processes of olefins (ethylene and propylene, respectively) **[13]**. In general terms, plastics can be derived from any of the basic petrochemicals (olefins, aromatics, and methanol), nevertheless, olefins are the most relevant source. They are considered the *"major building blocks of the petrochemical industry"* as they represent 90% of the raw materials of petrochemical end products with a market that is estimated to keep rising in the next years at a rate of 4.5% compound annual growth rate (CAGR) **[14,15]**.

Crude oil, natural gas, and coal are the primary sources for the production of the feedstocks for basic petrochemicals: ethane, propane, butane, naphtha **[15,16]**. In the specific case of olefins, these can be obtained from three major pathways: steam cracking, catalytic reforming, and on-purpose processes. The principal on-purpose-processes encompass propane dehydrogenation, metathesis of ethylene and butylene, fluidized catalytic cracking (and high severity fluid catalytic cracking), and methanol to olefins, as represented by **figure 2 [17]**.

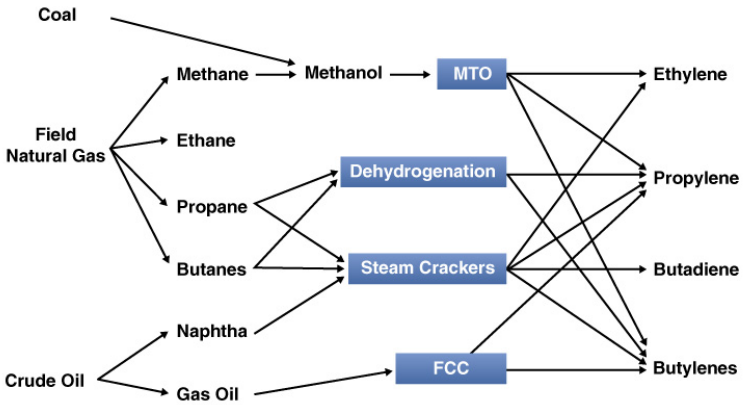

Figure 2 – Most relevant upstream industrial pathways to the production of light olefins. Retrieved from [17].

Steam cracking is considered the most efficient and viable process, employed for nearly all ethylene's and propylene's supply **[18]**. In recent years processes where ethane is used as feedstock have overtaken the industry (to the detriment of naphtha), making this process mainly ethylene selective. At the same time, it is one of the higher energy-consuming processes in the chemical industry, responsible for 8% of the sector's primary energy use, with approximately 75% of exergy loss **[16]**. Fluidized catalytic cracking, FCC, is a refinery process that has as principal aim the production of gasoline but also produced propylene and heavy olefins, responsible for over 50% of olefin production making it the second most utilized process **[19,20]**. Propane dehydrogenation (PDH) is a propylene selective process, with yields up to between 80-90%, but only accounts for about 5% of propylene's production as this technology presents great challenges regarding the efficient

adsorption/activation of propane and desorption of propylene on the surfaces of heterogeneous platinum catalysts **[21,22]**.

The great challenges faced by the shift in steam cracking selectivity and the propane dehydrogenation process caused a great instability in propylene's production which resulted in the development of the methanol to olefins (MTO) process. From all the viable technologies (figure 3), MTO conceptually represents a great promise in order to solve this matter, being able to reproduce an average selectivity of 60% towards propylene, with variations possible depending on the operating conditions and choice of catalyst **[23,24]**.

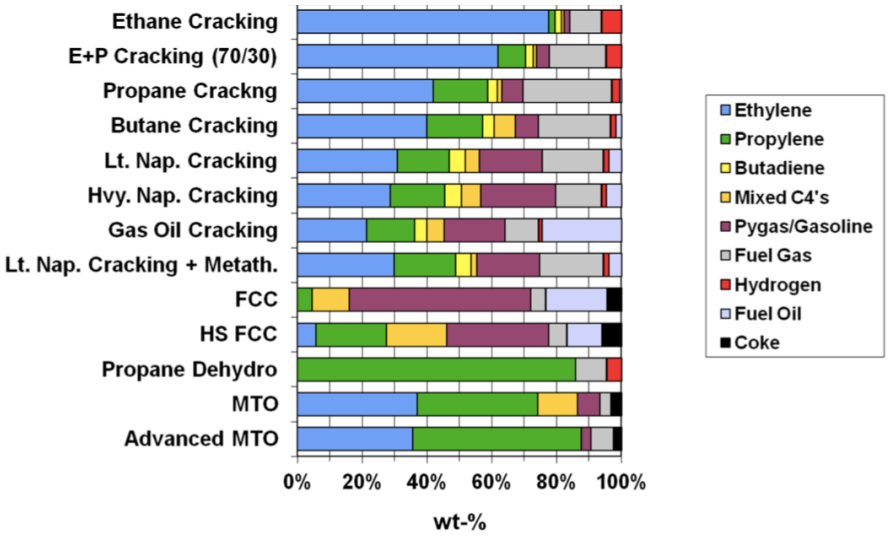

Figure 3 – State of the art olefin production technologies with relative yield concerning the major olefin products. Retrieved from [24].

The necessity of this investment is solidified when propylene's demand keeps increasing. In 2019, propylene global capacity was estimated at 130 mtpa where ethylene registered approximately 192 mtpa **[25,26]**. The market for both products presents a positive trend with the addition of new capacities worldwide, predominantly in Asia (China and India) where the rest of the transforming chemical and petrochemical industry have also been settling in **[27]**. Until 2030, propylene market growth is expected to increase by 48% (in respect to 2019) to a global capacity estimated to reach 192 mtpa, with China accounting for 48% of this investment **[25]**.

The primary application for propylene is polypropylene (PP), the second most produced plastic in the world, responsible for almost 70% of propylene's production, followed by propylene oxide (PO), acrylonitrile (ACN), acrylic acid, cumene, and other chemicals **[28,29]**. Different production methods produce different propylene grades. These can range from a refiner grade between 60-70% (40% of the total propylene production), the steam cracking processes (46% of the total production) lead to either the minimum chemical purity of 93-94% or a polymer grade purity with a minimum of 99.4% (which can also be obtained via PDH, metathesis, and MTO) **[30]**. On-purpose-processes investment is centralized in the technologies of PDH, and MTO **[31,32]**.

MTO appears in this context as an emergent technology. One of the biggest setbacks is its economical competitivity compared to other sources of propylene **[33]**. Most commonly, methanol is produced by catalytic reaction of syngas obtained by steam reforming of natural gas (petroleum residues, or naphtha). Having a green production of methanol and having it as the raw material of propylene would not only present itself as a way of overcoming our society's dependency on fossil fuels but also presents the direct application of a solution that aims to solve our climatic crisis **[33,34]**. This presents a great opportunity for industries with large carbon dioxide/monoxide streams to turn their carbon footprint into a product by of added value (supported hydrogen clean-production sources). Industries of cement, iron, steel, biomass, biogas, and natural gas are currently looking forward to expanding their units to fulfil the carbon neutrality commitment. This is the foundation of a circular economy. In Belgium, the project to be "*largest renewable hydrogen-to-methanol complex in the world*", North-C-Methanol (**figure 4**), has been launched, able to generate up to 44 ktpa of green methanol locally, serving as a landmark for many others to follow **[34]**.

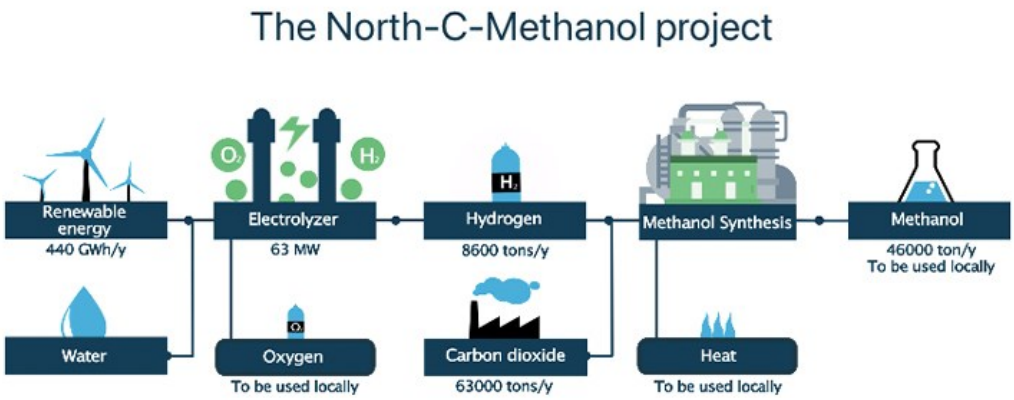

Figure 4 – North-C-Methanol, first large-scale green methanol synthesis demo plant as part of the North-CCU-Hub program, located at the Rodenhuize peninsula in North Sea Port (Ghent, Belgium). Retrieved from [34].

Although several plants are already in place with almost 1 mtpa of capacity **[35]**, the MTO reaction has demonstrated to be challenging both in scientific and industrial fields. Methanol starts by having a very complex mechanistic pathway to form hydrocarbons. The difficulty in both control and understanding of the reaction, quick deactivation and selectivity over acidic zeolites is still presently a great challenge **[36]**. The major lack of intrinsic kinetic data (studies in the absence of mass transfer limitations at steady-state) is the main cause for the inconsistencies found literature which prevent the indubitable knowledge of the real mechanistic pathways and struggle to make efficient, safe and economical reactor designs on industrial scale to make the existent processes economically viable **[36]**. The large-scale industrialization of the MTO process has also made fundamental the overcoming challenges in catalyst design, process energetic optimization and overall environmental requirements to guarantee the longevity, competitiveness, and low waste emissions for this technology **[37, 38]**.

1.1 *Objectives and outline*

With the increasing demand of olefins, propylene production technologies stand out with the need of further improvements. The main industrial MTO technologies so far developed use different catalysts, reactors, operating conditions, and present distinct olefin yields. Today, the dual-cycle concept is widely accepted as the steady-state mechanism involving a balance between catalytic cycles with both alkenes and aromatics as hydrocarbon intermediates.

Different operating conditions and catalysts have been studied in the past decades but with a major lack of concern for intrinsic kinetic data acquisition. This can be attributed to the difficulty to study these reactions in the absence of mass transfer limitations at steady-state and quick deactivation of the catalysts, and it is responsible for the setbacks in finding reliable rate expressions for a selective production of olefins, energetic optimization, and reliable construction of kinetic models – which are fundamental for an efficient reactor design and a competitive process.

The scope of the present thesis is to study the effect of H-ZSM-5 acidity on the mechanistic pathways of MTO within the dual-cycle concept. Data will be acquired at different operating conditions, under steady-state and intrinsic kinetics regimes. Experiments will be used as a descriptor for catalyst activity, product distribution and reaction mechanism. In this work, characterization of the catalysts will be a powerful tool to bring insight and support to the formulated hypothesis and conclusions.

This dissertation shall be divided in 5 parts. The first chapters will aim to introduce the topic under study within the social-economic context of the chemical industry and market, followed by an in-depth overview of MTO as an industrial process with environmental concerns and as an exceptionally complex reaction with the state of the art. Fundamentals regarding past and contemporary hypothesis on the mechanistic pathways, catalyst properties, and catalyst performance, will also be covered.

In the third chapter procedures on catalysts preparation and characterization will be addressed as well as a thorough description of the different components of the High Throughput Kinetic setup used for the catalytic studies, the essential parts of troubleshooting faced, and the reaction conditions utilized.

The last two chapters will comprehend the zeolite characterization and the catalytic studies' results. The thesis will culminate with the hypothesis and conclusions gathered from the discussion of all the data, together with the prospects on the subject. A distinct focus will be given to the formulation of mechanistic implications from H-ZSM-5 acidity effect.

2 *State of the Art*

2.1 *History of the Contemporary Industrial Technologies*

The early stages of MTO process were a result of the firstly developed technology of conversion of methanol to gasoline. Almost a half a century ago, in the early 70s, researchers at Mobil Corporation (currently ExxonMobil) started testing a newly synthesized zeolite, H-ZSM-5, and soon after accidentally discovered a process to convert methanol to gasoline and olefins (MTG, 1977) **[35, 39]**. A few years later, in 1981, Union Carbide (later UPO/Norsk Hydro joint venture and currently Honeywell UOP) introduced the current methanol to olefins process (MTO) with SAPO-34 as catalyst showing a particular selectivity and control over the light olefin product distribution (C_2–C4) **[40, 19]**.

The MTG (also known MOGD, olefins-to-gasoline and distillate process) was conceived to produce octane gasoline through the oligomerization of light olefins from refinery streams, more precisely, streams obtained from steam reforming of natural gas to synthesis gas. Initially, by attempting to alkylate isobutane with methanol into different oxygenates, this technology resulted in the yielding of liquid hydrocarbon fractions with higher molecular weight olefins in the range of gasoline, distillate, and lubricants **[41, 42]**.

Process conditions are adjusted according to the water content of methanol during the dehydration reaction that forms an equilibrium of dimethyl ether (DME), methanol, and water in the first reactor (over a gamma-alumina catalyst). To suit the highly exothermic conversion of the effluent to hydrocarbons (1480 $kJ/kg_{methanol}$), the MTG reaction zone that follows is composed of multiple fixed bed reactors with an H-ZSM-5 catalyst in parallel to prevent the formation of hotpots and fast catalyst deterioration (as well as the formation of undesirable products or unfavourably changed product distribution). Process conditions ensure 100% of methanol conversion, yields up to 90% towards gasoline, 75% selectivity for liquid fuels (C_{12} and lower olefins), and the remaining 25% reflecting gaseous products (largely C_3 and C_4) at an adequate proportion for higher octane gasoline **[43-46]**.

At the end of the century, this (unproven commercially) technology was chosen for a new plant over the commercialized SASOL Fischer-Tropsch process by the New Zealand's government to convert natural gas to gasoline in a fixed bed reactor in a capacity of 600 ktpa - a big investment that eventually resulted in the shutting down of the unit due to the lack of competitivity of production prices comparing to the global gasoline barrel **[42]**. During the 80s, an experimental 4 ktpa plant was built with a similar process scheme utilizing and the same catalyst but for Mobil's MTO process, whereas a fluidized bed reactor is utilized instead, proving its efficiency **[42]**.

Union Carbide's MTO process differs from the first technology by aiming for the production of ethylene and propylene, where crude methanol streams can be used without further purification (unlike the previous), under conditions ranging from 400-450° C and low pressures (around 3 bar). It

utilizes a fluidized bed reactor and a continuous catalyst regeneration cycle in parallel as the mildly acid SAPO-34 presents severe deactivation by the building of coke **[35, 47]**. Yields up to 80% are possible achieve for the aimed olefins (with higher selectivity to ethylene), where ratios can be adjusted by varying the reactor's conditions in a range from 0.75 to 1.5 (propylene/ethylene) **[40, 19]**.

A plant with 250 ktpa of production capacity plant been constructed in Nigeria, but China holds the biggest global capacity and higher plant number, with productions over 1 mtpa. The latest collaboration with Total Petrochemicals provided the optimization of this technology on the olefin cracking process (OCP) to even higher selectivity towards lower olefins **[41, 42, 48].** Furthermore, the MTO technology has evolved towards the utilization of the industrially modified SAPO-34 catalyst, named MTO-100, by UOP and Norsk Hydro which presents a higher attrition resistance and stability, able to handle multiple regeneration steps and fluidized-bed conditions **[19, 42]**.

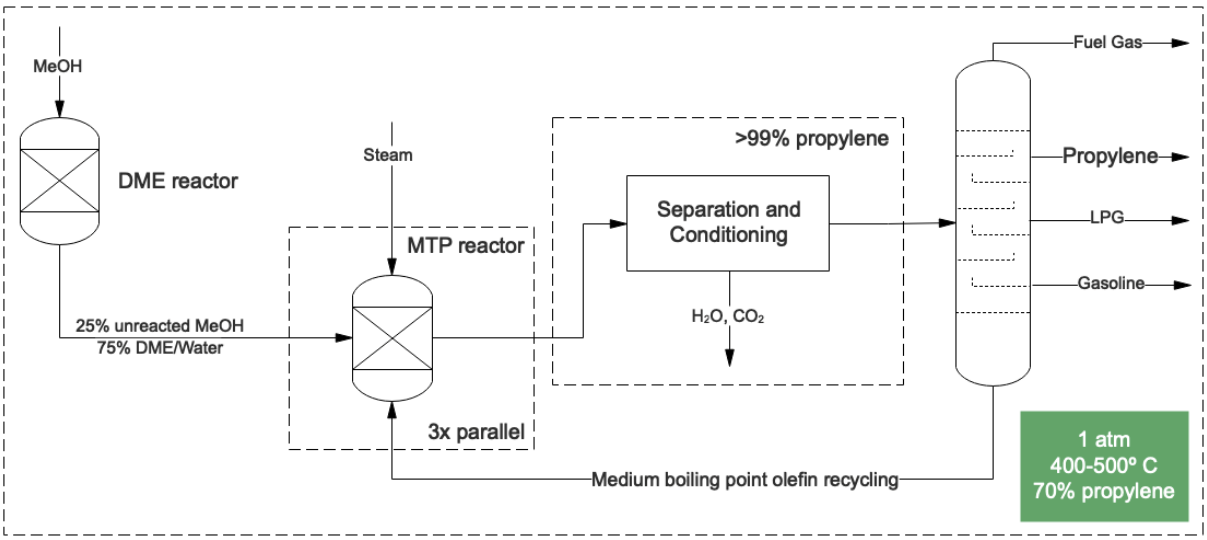

Figure 5 - Lurgi's MTP process. Adapted from [35, 48, 49].

Recently, Lurgy further optimized these technologies by developing an methanol to propylene process (MTP) in a fixed bed reactor over a high silica H-ZSM-5 catalyst **[37]**. The process is very similar to Mobil Corporation's described previously. It encompasses a methanol dehydration step, followed by a hydrocarbon conversion stage with three MTO reactors in parallel (2 functioning and one in standby mode to remove the formed coke by introducing air for catalyst regeneration) operating at atmospheric pressure and higher temperatures **(**represented in **figure 5**) **[37, 48, 49]**. This technology reflects an accumulated dry propylene yield as high as 70% at 100% conversion of methanol combined with an easier scale-up project with lower investment costs **[48, 49]**.

The Dalian Institute of Chemical Physics (DICP) in China developed a similar methanol/DME to olefins process (DMTO) with the aim of reaching high propylene yields **[50]**. This process operates at low pressures (1-10 bar) and high temperatures (330-723º C), with conversions near 100% for DME predominantly yielding ethylene and propylene (with selectivities of 10.4%, 75%), as well as

butylene and other light gases **[20, 37]**. This technology has been further developed since by DICP, resulting in DMTO-II and DMTO-III, in which the higher olefin by-products (C_{4+}) are separated and recycled back to the fluidized bed cracking reactor **[37]**. The process incorporates a zone for methanol dehydration, alkylation of ethylene by methanol over a SAPO-based catalyst in a fluidized bed reactor, and C_{4+} cracking processes **[36, 37**]. Furthermore, in 2009, Tsinghua University developed another fluidized-bed technology (FMTP) over SAPO-18/34 that demonstrated a propylene selectivity of approximately 67% **[37]**.

Sinopec's S-MTO technology was developed by Sinopec Shanghai Petrochemical Research Institute, Sinopec Engineering Construction Company (SEI), and Beijing Yanshan Petrochemical Company, having as main by-products carbon monoxide/dioxide and hydrogen **[47]**. This technology presents a great opportunity for a coupled industry to recycle these by-products into the main raw material of MTO, methanol.

Currently, DMTO technology has the biggest occupancy in China, accounting for 57% of total coal- and methanol-based olefins with 7.16 mtpa of production capacity by state-owned companies (Shenhua and China Coal group). This technology is followed by a 12% market share occupied by UOP's MTO technology (mostly used by private companies) while Lurgy's MTP mainly licenses Shenhua and Inner Mongolia Datang plants **[35, 37, 51, 52]**.

2.2 *Environmental Outlook*

With the devolvement of this coal-based olefin technology (most frequently observed in China) raises environmental concerns and questions regarding favourable governmental policies **[53]**. MTO requires high capital investment due to the complexity of the process. It presents a high consumption of water, and a high carbon footprint estimated in 5-10 tonnes per tonne of high-value chemicals (HCV, such as ethylene, propylene, and aromatics) produced when coal is the carbon source **[53, 54**].

Discussing specifically CTO (coal to olefins) the settling in the Asiatic zone not only can be attributed to the economic growth of the whole region but also to the high accessibility of the raw material coal at low prices [55]. Simultaneously, the need for high capital investments (2.8-3.5 billion USD for a 600 ktpa) is satisfied by the facility in bank loans and external investment **[55]**.

CTO requires about 29-40 tons of water per ton of olefin produced (which is a scarce resource in several regions of China with abundance in coal) and is responsible for three times the carbon footprint produced in naphtha cracking (around 11 tons of CO_2 per ton of olefin) **[55]**. Even though steam cracking is a very energy-intensive process it has been an industrialized technology for decades but optimized throughout that same period (**figure 6) [53]**.

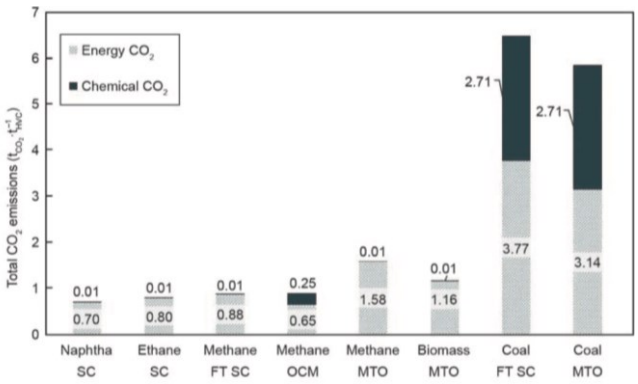

Figure 6 – Total CO_2 emissions per ton of high-value chemicals (t_{CO2}/t_{HVC}) for different technologies. Retrieved from [53].

Comparing MTO to other alternative technologies such as FCC, dehydrogenation, and metathesis the same questions arise **[20, 53]**. The energy use and CO_2 emissions of methane-based routes produce up to 60-85% more CO_2 emissions and energy use than the state-of-the-art ethane cracking **[54]**. Amongst methanol routes, the UOP MTO process is currently the most efficient (despite an energy use almost 150 times higher compared to the state-of-the-art cracking and slightly higher CO_2 emissions than the oxidative coupling of methane, OCM) **[54]**. Data is still being gathered with new experimental plant trials to investigate the potential of using bio methanol or available CO_2 streams/CO_2 capture. A synergy between petrochemical and refinery industries is also fundamental to achieve market competitiveness and environment suitability by integration of resources **[56]**.

Since the early 70s that these technologies have been a target of considerable devotion in academic studies and patenting, driven by successive technological advancements. Scholars have been demonstrating interest in the subject at an escalating pace as environmental concerns rise **[50]**. At the same time, olefins and petrochemical derivates' demand also increases. The need for more precision and formulations regarding basic principles, such as the reaction mechanism, has been pushing scientific studies forward to reduce carbon emissions and energy requirements **[50]**.

2.3 *Reaction and Mechanistic Pathways*

The mechanistic pathways for the MTO process have been under study since very early into the development of the described technologies. The conversion of methanol to hydrocarbons has always shown a high complexity, corroborated by the fact that until now more than 20 direct mechanisms have been proposed to describe the formation of first C-C bond **[42, 57]**.

The dual cycle mechanism is currently the most widely accepted proposal **[58]**. The currently accepted pathway for the MTO reaction involves a 3-step reaction (**figure 7**): first, an equilibrium of acid-catalysed dehydration of methanol to DME, followed by the formation of the initial C-C bond, and then the production of higher olefins from a primary pool of hydrocarbons (through a carbon chain

growth, alkylation and polycondensation of light olefins, and coke formation from hydrogen transfer reactions) **[59-61]**. Currently, it is believed that ethylene might be the first olefin to be formed **[59]**.

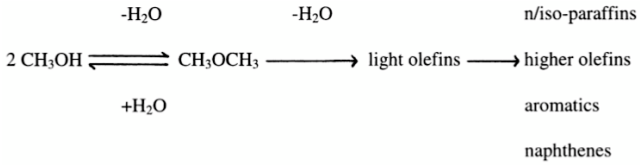

Figure 7 – Simplified scheme of methanol to hydrocarbons process. Retrieved from [42].

Early studies on the MTO reaction presented a well-known autocatalytic evolution with an S-curve shape: the methanol conversion rate starts very slowly for low residence times (known as induction period), right before an exponential growth until full conversion (passing first through a small intermediate phase named acceleration period) with space-time as it is further accelerated with the increase of hydrocarbon products in the medium, observed in **figure 8 [58]**.

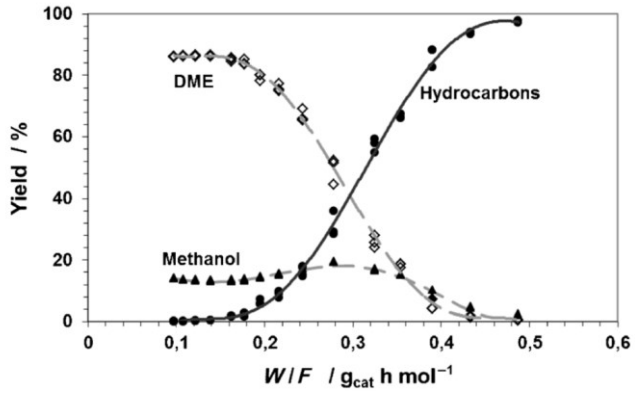

Figure 8 – Evolution of MTH reaction in terms of MeOH, DME, and hydrocarbon yields on a carbon base (%) concerning the space-time, W/F (g_{cat}.h/mol), expressing the typical S-shape curve in autocatalytic reactions. Retrieved from Olsbye et al. (2012).

Therefore, besides being an extremely exothermic reaction that takes place at moderate temperature over acidic catalysts, MTO was found to be an autocatalytic reaction where at least one of the reaction products is also the catalyst for the same or a coupled reaction **[62]**. For low conversions (<50%), the olefin conversion to aromatics can be neglected and the autocatalytic step is much faster than the formation of the first olefin from the oxygenates [42, 58, 63]. Several kinetic models have found the latter reaction to be accurately described by a first-order behaviour (concerning both oxygenates and olefins) **[42, 58, 63]**.

Methanol dehydration (as well as alkylation and methylation reactions) is thought to occur in the weak acid sites of the catalyst. The slow induction period that follows is believed to be explained by the formation of the first C-C bond (difficult due to the high energy barrier) initiated at the strong acid sites **[60, 64]**. Once a small amount of bonds has formed, the rapid formation of active aromatic

species (poly-methylbenzenes, which are considered to act as co-catalysts), together with the acid sites of the catalyst, give the exponential reaction of methanol into light alkenes **[64**].

The induction period is observed to be shortened at higher temperatures, resulting in a shift to the left of the conversion curve and an increase of exponential growth period **[65]**. DME has been identified as a faster alkene/arene methylation agent than methanol over H-ZSM-5 **[66]**. The nature and origin of the first C-C bond, as well as the first product formed by it, and whether ethylene is the first olefin formed are still subjects under intense debate **[67]**.

The proposed pathway follows the first dehydration of methanol to DME in an equilibrium (inversely favoured by a rise in temperature) between methanol, water, and DME (where the protonated catalytic surface suffers a nucleophilic attack by methanol), and only then the conversion to hydrocarbons takes place, starting with the formation of lower olefins and lastly, paraffins, aromatics, naphthenes, and higher olefins (**figure 9**) **[42, 65]**.

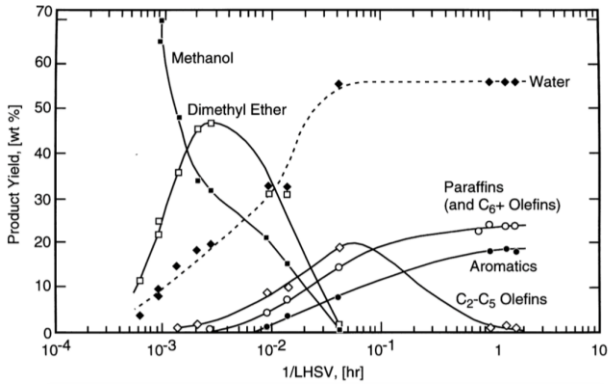

Figure 9 – Reaction path (wt. % product yield vs. contact-time) for the conversion of methanol into hydrocarbons at 371º C. Retrieved from [68].

The findings by Chang and Silvestri (**figure 9**) at the time of the development of the MTG process were considered a landmark in the formulation of the MTO process. The interruption of the reaction path by control of temperature and space velocity, allowed a greater light olefin yield to be obtained rather than mainly gasoline **[68]**. Mobil Corporation researchers (Chang, Schoenfelder, Tshabalala, Squires) focused their studies on ZSM-5 in fixed bed configurations whilst Union Carbide researchers invested in researching and developing the technology over SAPO-34 **[35].**

Several proposals have been made to explain the pathway from which the first C-C bond forms from methanol/DME **[36, 42, 69]**. Direct mechanisms (i.e., include the oxonium ylide, carbocation carbide) were first studied but could not explain the initial stage of the “dynamic induction period” due to the high activation energy barriers, only describing the very early stage of methanol conversion **[57, 69, 70, 71]**. The presence of traces of organic impurities (on the reactant, catalyst, or carrier gas) **[57]** and infinitesimal small quantities carbon monoxide (acting as the nucleophilic species) were also investigated **[73-76]**. Although it remains an unanswered scientific question, it has been considered to be of little practical importance.

2.3.1 *Hydrocarbon Pool Mechanism*

In the early 90s, Dahl and Kolboe proposed the most widely accepted mechanism, known as hydrocarbon pool (HCP), described as a "catalytic scaffold with organic molecules adsorbed onto the zeolite structure" **[77]**. The study, performed over SAPO-34 catalyst due to its mild acidity and topology (which results in narrower product ranges of C_2-C_4), determined that the HCP should be mainly formed through methanol-originated species **[58, 78]**. Since then, the HCP mechanism has been proven to be dominant at steady-state **[59]**. However, the velocity of the secondary reactions and unsuitable monitoring techniques have prevented further progress **[59]**.

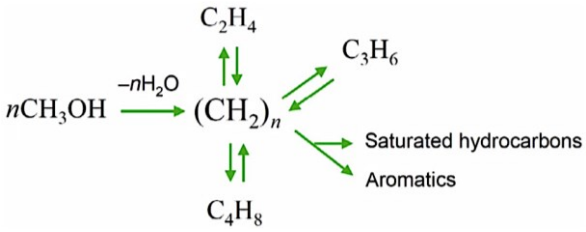

Figure 10 - Hydrocarbon pool mechanism proposed by Dahl and Kolboe. Retrieved from [58].

Dahl and Kolboe also proposed that this pool of hydrocarbon species would have a similar structure to coke (poly-methylated aromatic molecules) and suspected them to be the catalyst deactivation precursors **[62]**. The current state of the art mechanism by which the HCP is assumed to be formed is called side-chain methylation and paring routes. These HCP species (**figure 10**), represented as $(CH_2)_n$, adsorb in the molecular sieve and go over successive methylations, subsequent elimination of side-chain, to produce light olefins such as ethylene and propylene **[58]**. This allows the regeneration of said species to close the cycle while also acting as co-catalysts in the same reaction **[58]**.

Three reaction stages started to be clearly distinguished in the induction period: the formation of the primary C-C bond, HCP species formation, and the start of the autocatalytic reaction stage **[59]**. The light olefins then follow a series of condensation, alkylation, cyclization, and hydrogen transfer reactions to form higher olefins **[42, 58]**.

The premise of the HCP concept only failed to properly describe the formation of propylene as it was concluded that most parts had to have been formed directly from methanol and only a minor fraction from the addition of methanol to ethylene **[42, 78]**.

2.3.2 *Paring and side-chain routes*

More relevant questions arose with the formulation of the HCP mechanism. Several studies have since then been conducted over ZSM-5 and SAPO-34 catalysts in order to determine the actual nature and number of hydrocarbon species in said hydrocarbon pool **[42]**.

Tools such as ^{13}C MAS NMR spectroscopy have been used to get past the complexity of the reaction mechanisms that arise from rapid secondary reactions and mass transfer limitations **[42]**. Studies by Anderson and Klinowski found almost 30 species in the adsorbed phase over H-ZSM-5 **[74,75]**. Derouane found evidence that supports the carbenium ion mechanism since these molecules were revealed to be strongly stabilized on the acidic and highly polarizing surface of ZSM-5 **[74,75**].

Evidence on methanol and DME reacting on aromatic species inside the catalyst active porous scaffolds for the assembly of light olefins (avoiding the high high-energy intermediates present in all direct mechanisms) have been presented. Svelle et al. (in accord with Haw and affiliates' work) confirmed that the most active of these hydrocarbon-pool species are predominantly polymethylbenzenes (PMB) and concluded ethylene is mainly formed from xylenes and triMB (whereas higher MB favour propylene) **[79, 80]**. This led to supplementary progress in the understanding of the main mechanistic contribution in the HCP hypothesis: the side chain (exocyclic methylation) and the paring mechanism **[81, 82]**.

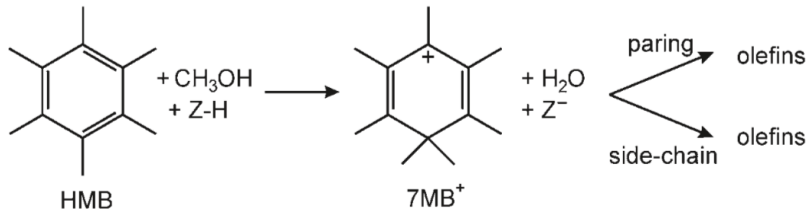

Figure 11 – Initiating step for the formation of olefins from hexamethyl-benzene (HMB). Z=zeolite. Retrieved from [81].

Both mechanisms start from the one-step geminal methylation (by methanol) of hexamethylbenzene (hexaMB) in order to give an heptamethylbenzenium cation (heptaMB+) (**figure 11**) **[81]**. MB and respective protonated counterparts are central for the formation of reaction intermediates. for the production of alkenes. The paring and side-chain methylation models appear as the rationalization for alkene formation from these species – adapted from the proposed work by Sullivan et al. (1961), Mole et al. (1983) and Haw and co-workers (2001).

In the paring mechanism, the carbocation species is thought to undergo a ring contraction in order to give a methylated five-ring. These structures undergo the elimination of olefins (mainly propylene and butadiene) through cracking reactions to having their structure restored by an expansion of the ring **[33, 81]**.

In the side chain mechanism, heptaMB+ is supposed to be deprotonated into HMMC, creating an exocyclic double bond, that through several methylations result in the elimination of ethylene (and propylene to a certain extension) **[81]**. A general scheme for the described can be examined in **figure 12**.

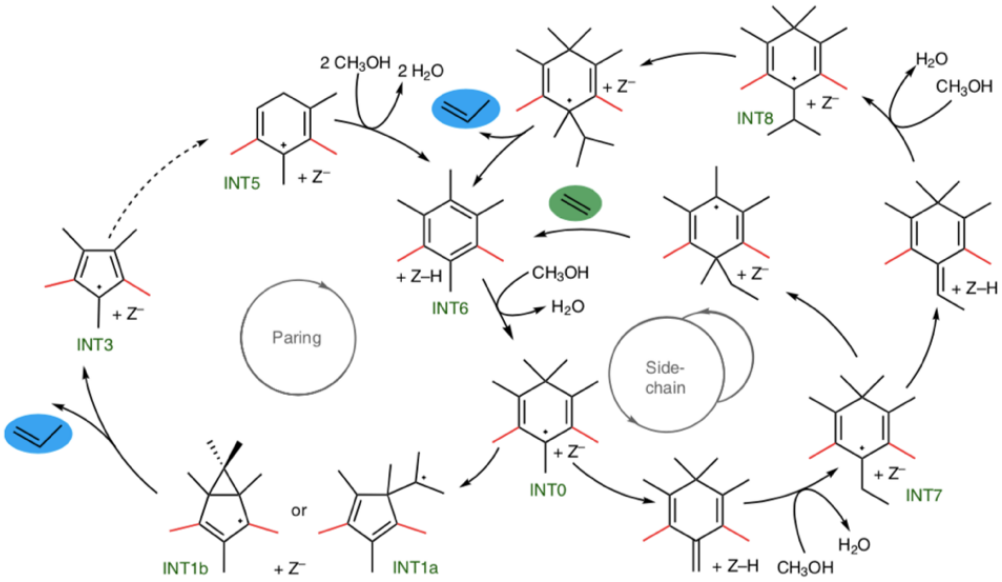

Figure 12 – Proposed hydrocarbon pool mechanisms for the MTO reaction, including the paring and side-chain routes [33].

Although the formation of the first C-C bond was implied to be a high energy barrier step, in recent years, the formation of HCP species has been under study as MTO's rate-determining step **[59, 83]**. In order to rationalize the formation of isobutene on H-ZSM-5, the catalytic cycle from the pairing route was proposed **[84]**. Starting from the methylation of toluene (as the rate-determining step in this route), pentaMB and 1,3-dimethylcyclopentadienyl were considered the reactive intermediates, and the complete catalytic cycle was established **[84]**. This proposal is per the observation that less substituted MBs have higher reactivity over H-ZSM-5 **[58]**. These calculations and HCP mechanism do not yet explain the full product distribution over this zeolite.

Penta- and hexaMB species also manifest the most activity as intermediates over SAPO-34, whereas hexaMB and tetraMB demonstrate the most activity over SAPO-18 and SAPO-35, respectively, which evidences how the catalysts' cavities play a key role in the type of HCP species formed and product distribution **[58]**. More substituted MB (pentaMB and hexaMB) are more favourable for propylene formation whereas less substituted MB (di, tri, and tetra-MB) have ethylene as the main product **[58]**.

Fečík (2021) work with the catalyst H-SSZ-13 studied the tetramethylbenzenes species as the co-catalyst for the rate-determining step motivated by their earlier work where hepta, poly, and tetramethylbenzenes (hexaMB, polyMB, and tetraMB) were found to be the most thermodynamically stable species adsorbed under the same catalyst **[85]**. It was found that the highest energy barrier was related to ethylene formation in the methylation step of an hexaMB cross-conjugated intermediate, which led to the formation of an ethyl group that follows a methyl shift and an eventual elimination of ethylene **[85]**. Previous reports mentioned that, for both paring and side-chain routes, the elimination of propene was found to be the rate-determining step for the paring and side-chain catalytic cycles with activation energies of 153.4 and 107.3 kJ/mol, respectively **[58, 86]**.

2.3.3 *Dual-cycle concept*

With the new millennium several pieces of evidence started to point out the real contribution of the direct mechanism (the work of Copéret, Lercher, Liu), after Haw's work, a time that further advancements on the indirect mechanisms were made. In 2006, Svelle and co-workers formulated the latest experimental data fitting mechanism up to date, called dual cycle-mechanism **[57, 79]**.

Up until that moment the prior art suggested two main routes for the formation of reaction products: either a sequence of hydrogen transfers, alkylations, polycondensations, and cracking or, the proposed HCP mechanism (alkylations and dealkylations of hydrocarbon scaffolds) **[50]**. With the observations that the trapped aromatics referred to as hydrocarbon pool species in small pore/channel catalysts (like ZSM-5 and SAPO-18), the dual-cycle mechanism was formulated, combining both approaches during steady-state operations **[62]**.

The dual cycle mechanism is considered the most recent state-of-the-art, describing the best experimental data fitting, although, with yet unfold some unclear interpretations. In **figure 19** it can be found a representation of said mechanism in a simplified manner with the olefin cycle on the left and the aromatic cycle on the right - the latter representing furthermore both the less methylated aromatics and the heavier compounds trapped in the zeolite structure **[62]**.

The dual-cycle mechanisms suggest that the two cycles occur simultaneously over H-ZSM-5 and can be considered essentially a refinement of Dahl's and Kolboe HCP mechanism. It was first suggested to explain the difference in the formation of ethylene and higher olefins over this zeolite as the first is generally attributed to the aromatic cycle (based on HCP mechanism) and propylene and higher olefins is thought to follow olefin methylation and cracking route, as depicted in **figure 13 [36]**.

There is consensus in the preposition that the aromatic-based mechanism is the primary describer of cage type SAPO's and H-Beta zeolites selectivity for lower olefins being as larger molecules persist retained in the internal framework; thus, being responsible for the very quick deactivation of the catalyst **[36, 87]**.

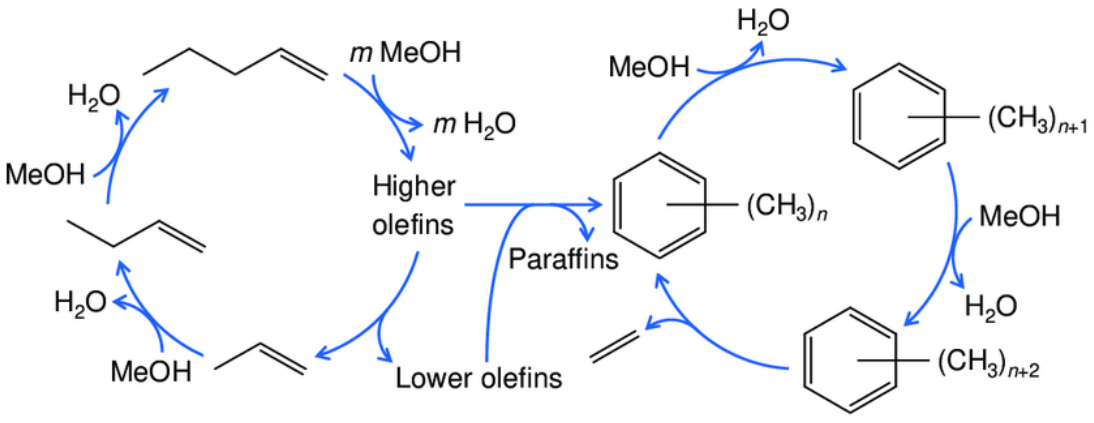

Figure 13 – Representation of Svelle et al. dual-cycle for MTO over ZSM-5 catalyst. Retrieved [62].

From the aromatic cycle, ethylene and propylene are formed from less substituted MBs, followed by re-methylation and methylation/cracking reaction that only involve C_{3+} alkenes **[87]**. The alkene cycle involves mostly C_{3+} which undergo a series of methylation/cracking reactions in H-ZSM-5's framework, which pores' architecture allow for higher alkenes to be released into the gas phase compared to SAPO's narrow pores **[87]**.

Current studies aim to further understand the complex mechanistic pathways behind MTO, specifically, the exact contribution of each cycle (aromatic-based hydrocarbon pool or olefin methylation and cracking route) for the olefin product distribution (of primary interest ethylene and propylene) in different reaction conditions, zeolite topology and acidity, and whether these cycles operate completely independently or intertwined **[36, 87, 88]**.

2.4 *Zeolite Topology and Acidic Properties*

ZSM-5 and SAPO-34 are the only two zeolite based catalysts employed until now in the MTH/MTO industrial processes, but several other catalysts and catalyst modifications have been under study since the discovery of this reaction **[87]**. Zeolites are crystalline materials, with an aluminosilicate base, with well-defined microporous structures and intrinsic properties **[89]**.

Topology (framework, channel network, and dimensions, internal cavities), composition (acidic sites, defects), and morphologies (crystal dimensions, and micro/meso-porosities) are considered the most important properties regarding catalyst performance **[87]**. Some of the properties of the two principal MTO catalyst can be observed in **table 1** and **figure 15**.

Table 1 – Principal physical properties of ZSM-5 (zeolite) and SAPO-34 (Phosphorus aluminum silicate).

Material	Topology	Channel structure	Typical Composition	Total Acidity (mmol/g)
ZSM-5	MFI	3D, 10-ring	Si/Al=[10,∞]	**Si/Al=30** 0.42-0.52 [a,b] **Si/Al=40** 0.25-0.33/0.31/0.14 [b,c/d/e] **Si/Al=140** 0.10-0.13/0.09/0.11 [c/d/e]
SAPO-34	CHA	3D, 8-ring	Al(50), P=[30,45], Si=[5,20], Si/Al=[0.05, 0.5]	**Si/Al=[0.23, 0.5]** 1.20-1.35 [f,g]

[a, b, c, f, g] Catalyst surface acidity studies by desorption of ammonia (NH_3-TPD), data retrieved from [72], [90], [91], [94] and [95], respectively. [d)] Measured Brønsted acid site density of ZSM-5 by sequential calcination/titration (with isopropylamine and t-butylamine, respectively) cycles, data retrieved from [92]. [e)] Measured Brønsted and Lewis acid sites density of ZSM-5 by pyridine-FTIR method, data retrieved from [93].

The knowledge of zeolite's structure, window dimensions, and internal channel systems, is fundamental in other to understand shape-selectivity and product selectivity. Channel dimensions are typically denoted according to their number of T atoms forming the window, which for most configurations translates into 12, 10, and 8-membered ring windows **[87]**.

Catalytic reactions occur inside the pores. Space requirements for intermediates species (higher olefins and polysubstituted methylbenzenes) and coke are larger than window dimensions,

so these molecules remain trapped in the cavities inside the internal framework of the catalyst causing its deactivation (poisoning of active sites and blocking of pores) **[37, 87]**.

All zeolites of interest to the MTO present a medium-high relative Brønsted acidity. These sites (BAS) are able to donate protons and consist of aluminium atoms connected to silicon by bridges between hydrogen and oxygen atoms (hydroxyl groups) connected to the zeolite's framework. They contribute with a negative charge in order to compensate the charge of a hydroxyl proton and are responsible for the catalyst's activity and lifetime, **figure 14 [87]**.

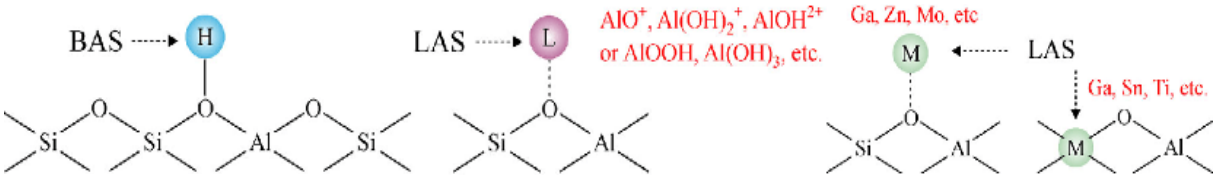

Figure 14 – BAS and LAS on zeolites. Adapted from X. Zhao et al. (2020) [96].

Lewis acid sites (LAS) are electron acceptors and, in H-ZSM-5, they appear in three main types. Primarily, Lewis acidity may be present as aluminium atoms with low coordination number, also referred to as extra-framework aluminium, Al_{EF} (Al^{3+}) **[90]**. These can also be found as charge-balancing extra-framework cations, providing a much weaker acidity than Brønsted sites **[90]**. Ultimately, they can also be created upon zeolite modifications such Mg, Ca, Cu, Ag, Zn, atom insertion in the zeolite's framework at T positions - which generally translates in the suppression of the aromatic cycle as they promote catalytic reaction **[97]**. Dealumination is known to lead to the formation of mesopores and Al_{EF} species and have been shown to lead to a significant decrease in coke deposition (one of the first reasons for zeolite's deactivation) in the MTO reaction **[97]**.

In this reaction, Brønsted sites are believed to be the main catalytic centres, and to be directly connected to a higher propylene selectivity **[57, 90]**. As high numbers of Lewis sites have also been demonstrated to be of most importance to increase the lifetime of the catalyst, a compromise between acidic strength and acid density in both Brønsted and Lewis sites should consequently be considered **[97, 99]**.

When changing Si/Al ratio (e.g., by substituting a silicon atom with aluminium in the tetrahedral zeolite framework), a proton is usually required to replenish the overall charge **[97]**. Thus, decreasing the Si/Al ratio results directly in an increase in the acid density, despite the acid strength of the sites decreasing as the hydroxyl bonds get stronger **[97]**. The acidity of H-zeolites is mainly attributed to the protons compensating the negative electronic charge of the framework caused by the incorporation of silicon atoms into the neutral framework **[100]**.

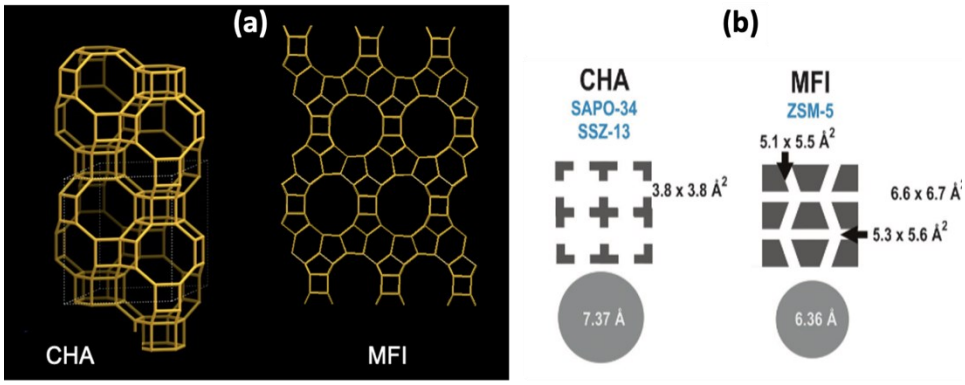

Figure 15 – (a) Framework topologies for CHA and MFI zeolites. Adapted from IZA 3D drawing. (b) Representation of several literature MTO catalysts, with pore sizes, pore openings, and the maximum diameter of a sphere (in grey). Adapted from [39].

Both ZSM-5 and SAPO-34 are 3D structured, they differ from each other in terms of framework structure and cage size. SAPO-34 presents a CHA structure with an 8-membered ring molecular sieve which translates into a structure that presents large cages (10×6.7×6.7 Å) and small pore ring openings (3.8×3.8 $Å^2$) **[39]** (**figure 15**). This channel arrangement has been demonstrated in the literature to have a higher shape-selectivity towards light olefins (ethylene and propylene) attributed directly to the higher diffusion limitations of larger reaction intermediates **[37]**.

On the other hand, ZSM-5 presents an aluminosilicate MFI framework type, with medium-sized pores, channel intersections, an interconnected tube arrangement, 10-membered ring cavities, and a network of sinusoidal (5.1×5.1 $Å^2$) and straight channels (5.3×5.6 $Å^2$) **[39]** (**figure 15**). In catalysts with channel intersections, both aromatic and olefin-based mechanisms are verified **[37]**.

Furthermore, the predominance of the alkene cycle can be promoted by decreasing the acid density of the catalyst, resulting in the selectivity propylene (40-50% propylene selectivity with propylene/ethylene ratios between 5 and 10, for Si/Al catalysts near 400 at 450º C and 1 bar) **[101]**. This catalyst presents a higher acid strength than H-SAPO-34 with a much lower acid density (H-ZSM-5: Si/Al=100, and SAPO-34 Si/Al=0.6) **[99, 102]**.

It is thought that the acid strength and topology of the catalyst have a major influence on the reaction route. Lower acid strength has been linked to the favouring the side chain mechanism and, regarding topology, some reaction steps only become possible when the molecular environment is considered **[81, 82].** Less acid densities together with high surface area and mesoporous catalyst, promote higher catalytic lifetime by minimizing the effect of deactivation due to coke deposition from diffusion resistance and pore blocking **[60]**.

ZSM-5 is significantly more stable (i.e., can undergo acid, alkaline, or hydrothermal treatment for construct hierarchical frameworks and adjust acid properties) than SAPO-34 **[103]**. Furthermore, SAPO-34 zeolites with low silicon content (moderate acidity) have a very complicated synthesis, resulting in mixed crystal phases, varied porosity, and low crystallinity **[103]**.

Lesthaeghe et al. extensively studied the reaction of methylation of hexaMB by methanol to form the heptaMB+ cation over CHA and MFI topologies **[104]**. A significantly higher reactivity by CHA framework was reported and attributed to the cage dimensions, as they provide an ideal electrostatic surrounding for the highly substituted MBs **[39, 104]**. The correspondent transition states of ipso-methylation of hexaMB are depicted in **figure 16**.

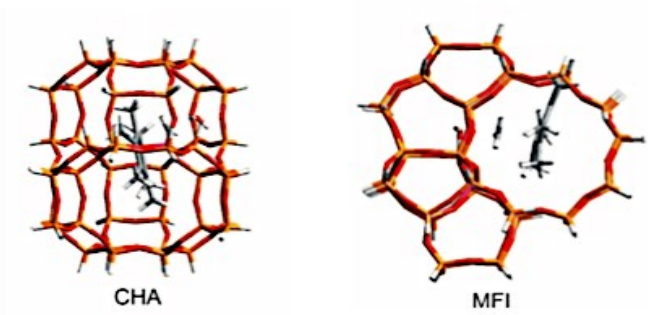

Figure 16 – Transition state geometries for the formation of the heptaMB+ cation in CHA and MFI frameworks (52T and 44T cluster models, respectively). Adapted from [39].

Several attempts searched to study one of the cycles by surprising the other through diffusion limitations. In principle, this can be accomplished by choosing an adequate catalyst topology capable of suppressing, for instance, the aromatic-based cycle, leaving methanol to be converted exclusively by the alkene cycle, yielding considerably lower amounts of ethylene **[88]**.

From H-ZSM-5's topology considerations, it has been strongly argued that the complete independent operation of cycles is not the case with ethylene and propylene formation. Product distribution yields high amounts of aromatics which are constantly produced as a result of the aromatization reaction of higher alkenes (formed by the alkene methylation/cracking cycle) which suggests that the alkene cycle is not completely independent **[88]**. Still, the formation of propylene from MB cannot be accessed at this point, even though ethylene displays a low reactivity for methanol for the formation of C_3-C_6 alkenes in comparison with propylene and butylene **[88]**.

H-ZSM-22 has been used for insight on this matter due to the steric properties of the catalyst topology. This is a high Si/Al ratio, with a framework with 5/10-ring openings, with a 1D linear, unidirectional, and non-interconnecting channel system slightly smaller than those found in ZSM-5 **[104]**. The aromatic cycle was successfully suppressed with aromatic species retained in the framework exhibiting no reactivity towards methanol and yielding C_{5+} olefins, with negligible aromatic content by the alkene methylation/cracking cycle and high propylene/ethylene ratio **[87, 106, 107]**.

H-SAPO-34 product distribution, due to shape selectivity from its narrow pore structure and shape selectivity, exhibits a predominance of ethylene, propylene, and linear pentenes **[87]**. Studies have confirmed that the product distribution in this catalyst is ascribed to the shape selectivity, which makes the mechanistic information difficult to analyse from the diffusion-controlled system **[87, 108]**.

Even though H-ZSM-5 will be the catalyst to be studied in the present work, understanding the elementary differences in the pathways that topology creates within the MTO reaction is relevant for the understanding of the mechanisms behind the future results.

2.5 *H-ZSM-5 Performance on MTO*

Effect of Operating Conditions: Temperature

As previously overviewed, due to its framework arrangement this catalyst presents an affinity towards both aromatic and olefin-based mechanisms, displaying reaction products from lower olefins (C_2-C_8) to aliphatics (with over 90% corresponding to C_{4+} olefins, such as butane), paraffins, aromatics, and coke – where C_{5+} aliphatics and paraffins in industrial processes are often recycled back into the MTO reactor in order to achieve higher olefin yields and lower coke deactivation rates **[109, 110]**. Operating conditions are a fundamental aspect towards achieving maximum yield and energy efficiency and are normally situated in temperature ranges between 300-500º C and pressures up to 4 bar.

A very thorough study of the different effects of MTO has been made by Sun (2013) and Losch (2016), both in the scope of their master thesis for operating temperatures between 350-500º C. The reaction temperature shows a distinct effect on the reaction rate, namely, in the shortening of the induction period of the autocatalytic reaction resulting in a shift of the curve towards lower contact times as reaction temperature rises **[73, 110]** (**figure 17-(a)**).

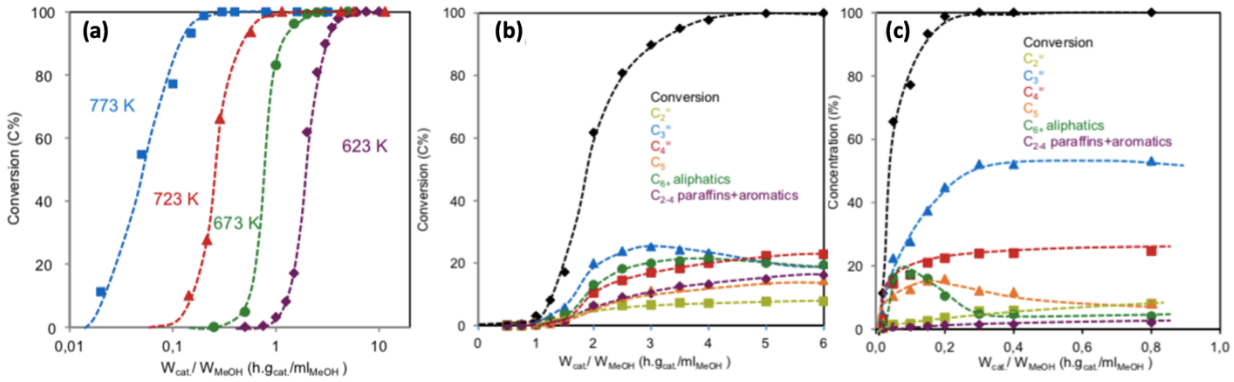

Figure 17 – MTO's (a) methanol conversion at reaction temperatures of 350, 400, 450 and 500º C; and (b) product distribution at 350º C and (c) at 500º C, as functions of space-time over H-ZSM-5 Si/Al=90 (P_{MeOH}=0.017 bar methanol diluted in N_2) Retrieved from [110].

From Sun's observations, with a temperature rise a significant increase in selectivity towards propylene and butadiene is observed **[110]**. At low conversions, it is verified a period predominantly composed by propylene production, followed by a period where olefins undergo homologation and oligomerization-cracking reactions (which results in the rise in selectivity C_{6+} aliphatics) that reach a

maximum value in average at 80% conversion of methanol and subsequently verify a sudden decrease in production as cracking reactions take place to form C_3-C_5 olefins (olefin cycle prevalence) **[110]** (**figure 17-(b,c)**).

Losch's studies over H-ZSM-5 (Si/Al=140) at 100% methanol conversion found no substantial influence of temperature on propylene selectivity between 440-560º C, and that at this temperature range, the catalysts suffer an exponential deactivation at lower TOS when compared to lower reaction temperatures **[73, 110]**. These observations denote the necessary prudence at interpreting and comparing product distributions at 100% conversion.

Ibáñez et al. (2017), proposed two stages of deactivation of the catalyst (Si/Al=140) that would occur in the first 1-2h of reaction (the fastest stage, with methanol and DME equilibrium with high production of methane) and then a slower stage which leads to steady-state conversions over time, each stage associated to the strongest and weakest acid sites, respectively **[109]**.

The same work presents a decrease in light olefin selectivity at higher reaction temperatures which is attributed to the occurrence of secondary reactions (oligomerization-cracking that result in higher yields of C_{5+} aliphatics, hydrogen transfer reactions, and/or re-adsorption of products that led to the formation of paraffins and aromatic species, and condensation reactions responsible for the formation of coke – thus resulting in the quicker deactivation of the catalyst **[109]** (**figure 18**).

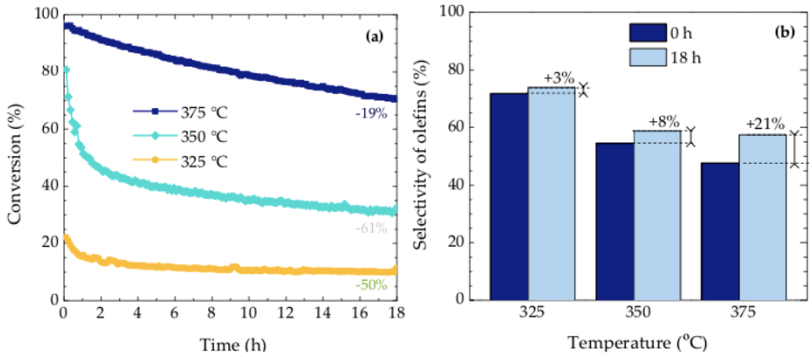

Figure 18 – Effect of reaction temperatures (325-375º C) on (a) methanol/DME conversion and on (b) olefin selectivity, over 18h TOS (fixed bed reactor, H-ZSM-5 Si/Al=140, pure DME feed 18 mL/min, 1.5 atm, at space-time 4 g.h/mol). Retrieved from [109].

This discrepancy highlights that, at the full conversion of methanol, contact times play a relevant role especially in data comparison and interpretation between different sources as, with increasing space-time, the product distribution would further change as a result of a predominance of secondary reactions **[109, 110]**.

Furthermore, higher deterioration of the specific BET and micropore surface area has been correlated as the preferential deposition of coke cause in the meso/macropores of the matrix (obstructing the active micropore centres) **[109]**. This explains the higher deactivation rates for higher temperatures, despite higher total amounts of carbonaceous species in the deactivated catalysts at

lower temperatures (verifying higher degradation of the textural and acid properties as well) - making the external coke deposition the major responsible for catalyst deactivation **[109]**.

Moreover, it has been found that at higher temperatures higher concentrations of water in the reaction medium are found, which have been known to attenuate coke deposition **[109, 111]**. Therefore, water is hypothesized to be responsible for a shift of the coke precursors from the micropores to meso and macropores of the catalyst (where they are transformed into bulky polyaromatics) **[109, 111]**.

Regarding the actual nature of carbonaceous species trapped inside the catalyst's pores, temperature appears to have influence thereon. With increasing temperature, an increase in alkyl-benzenes and polyaromatics (predominantly 5+ ring aromatics) has been verified **[109]** (**figure 19-(a)**). In the case of lower temperatures (325º C), the aromatic cycle is dominated by polyalkylbenzenes (predominantly pentaMB and tetraMB) that despite presenting a lower activity than alkylbenzenes and lower DME conversion, lead to higher olefin selectivity.

At higher temperatures alkylbenzenes, as the predominant pool species quickly suffer condensation at the strong acid sites resulting in their obstruction, thus changing the reactive sites to the medium strength ones with lower olefin selectivity (also due to the higher amounts of water in the medium as DME conversions increases, as previously mentioned).

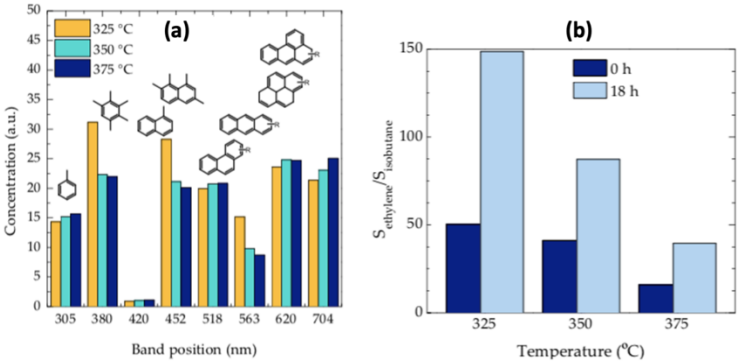

Figure 19 – Effect over temperature on the (a) concentration of the coke species trapped inside the over the deactivated catalyst (H-ZSM-5 Si/Al=140) by means of UV-vis spectroscopy. (b) Correspondent ratio of aromatic/olefin cycles. Retrieved [109].

This finding helps to answer one of the main objectives of these studies, to further understand the predominance of each cycle in the dual cycle mechanism – which is frequently measured through the ratio between ethylene and isobutane (E/Isob) as a representation of the proportion of aromatic/olefin cycles **[109]**. According to **figure 19-(b)**, the aromatic cycle is significant both at longer TOS and lower temperatures and predominant in the production of lower olefins over H-ZSM-5 catalyst, responsible to produce alkylbenzenes (in the acidic micropores of zeolite), and the olefin cycle responsible for the higher concentration of 5+ ring aromatics and higher amounts of coke **[109]**.

A study by Ilias et al. (2013) of H-ZSM-5 Si/Al=42.6 sheds light on many of the observations discussed before **[112]**. To determine the relative propagation of the aromatic and alkene cycle, the ratio between ethylene and the sum of the yields of 2-methyl-2-butene and 2-methylbutane (2MB) was used, respectively.

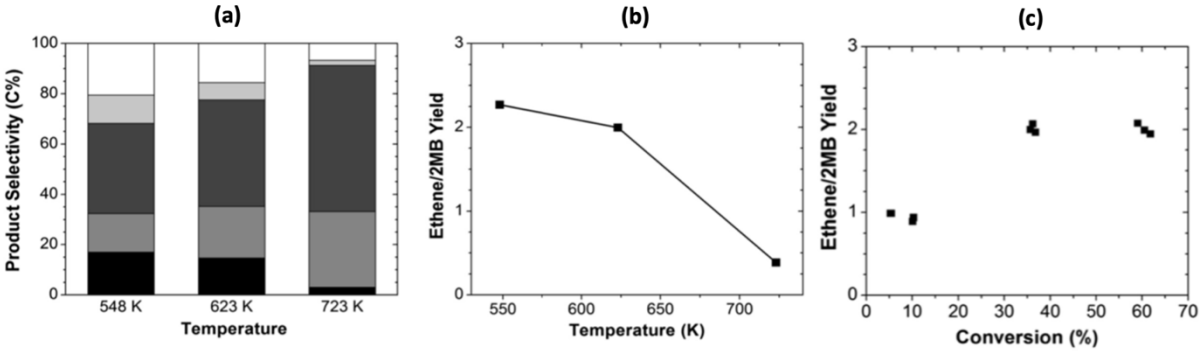

Figure 20 – For the feeding of P_{DME}=0.7 bar for the conversion of olefins over H-ZSM-5 Si/Al=42.6 on a carbon basis at iso-conversion (59.4–60.7% DME conversion): (a) product distribution (black: C_2; medium grey: C_3; dark grey: C_4-C_7; light grey: MB; white: others) and on (b) ethylene/2MB ratio as functions of temperature; (c) ethylene/2MB ratio as a function of conversion at 623 K. Adapted from [112].

An increase in reaction temperature observes higher propagation of the alkene cycle by increasing the selectivity of C_3-C_7 hydrocarbons (**figure 20-(a,b)**) and decreasing ethylene and MB yields at iso-conversion. For the temperatures studied, it was found that the aromatic propagates more relatively to the alkene cycle at higher conversions (**figure 20-(c)**).

Overall, these studies appear to indicate that temperature is responsible for promoting C_{3-4} olefin production by favouring the alkene cycle, while secondary reactions also proliferate. Furthermore, the effect of temperature observes deactivation with lower contact times from coke deposition at the catalyst's strong acid sites.

Effect of Operating Conditions: WSHV and Conversion

M. Zhang et al. (2016) also studied the effect on the catalytic performance and reaction intermediates through the variation of methanol weight hourly space velocities (WHSV) **[113]**. The catalytic tests verified that for the highest WHSV (**figure 21-(c)**), the lowest conversion (1.4%) was achieved. During the first minutes of reaction, C_2-C_6 and methane were the primary reaction products. After 30 minutes the reaction pathway quickly achieved 100% methanol conversion with increasing selectivities towards C_4-C_8 and xylenes. For reaction times higher than 30 min, it was observed a transition of selectivities towards C_2-C_3 and triMB and a drop in methanol conversion up to 55%.

For the remaining WHSV evaluated values, for the same reaction temperature, the reaction path exhibited higher induction periods with low carbon species predominant in the first reaction minutes (mostly methane). This was attributed to the deposition of aromatic compounds in the zeolite

pores **[113]**. As the reaction proceeds, heavier olefins were formed, registering higher selectivities towards propylene and butylene at the expense of lower selectivities for ethylene and aromatics.

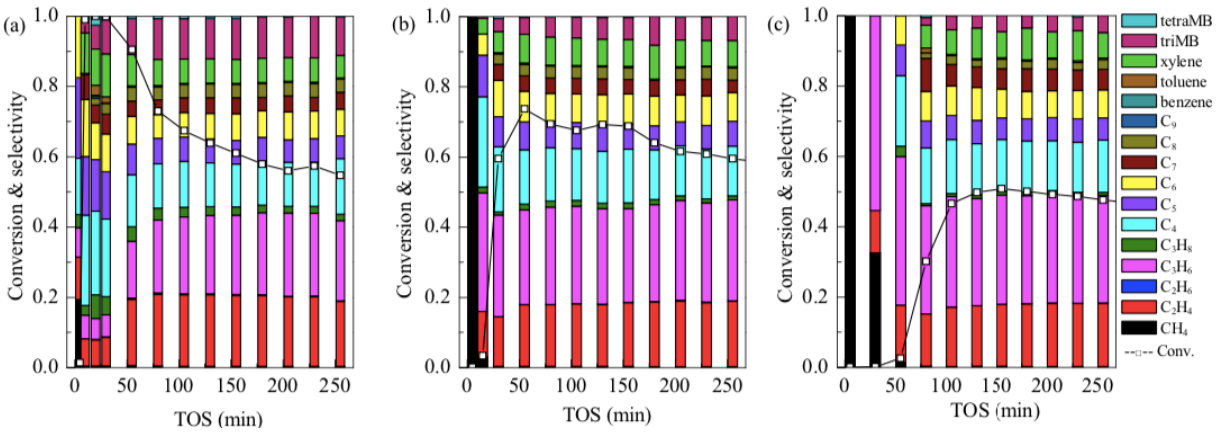

Figure 21 – Conversions and product distributions during of MTO reaction over H-ZSM-5 Si/Al=19 at 300° C at WHSV of (a) 2 h^{-1}(w/w 156 ms); (b) 6 h^{-1} (w/w 31 ms) and (c) 12 h^{-1}(w/w 16 ms). Retrieved from [113].

Moreover, the evaluation of hydrogen transfer indexes (expressed by C_3H_8/C_3H_6 selectivity ratios) for each experiment demonstrated a negative correlation between methanol conversion and WHSV **[113]**. In other words, with higher methanol feeding rates, the greater the amount of unconverted methanol and lower the maximum conversion achieved **[113]**. Hydrogen transfer reactions were also promoted at low WHSV (**figure 22-(a)**) – resulting in a different reaction path.

Furthermore, since an increase in WHSV relies on an increase in methanol feed, catalyst penetration might become a factor uncertainty as the methanol feed cannot be totally converted (resulting in inexact conversion levels) especially during the induction period **[113]**. As a result, it was investigated the absolute conversion of methanol normalized to the unit mass of catalyst (**figure 22-(b)**). Conversely, it was observed that the conversion capacity of the catalyst increases with increasing WHSV whilst increasing the induction period as well **[113]**.

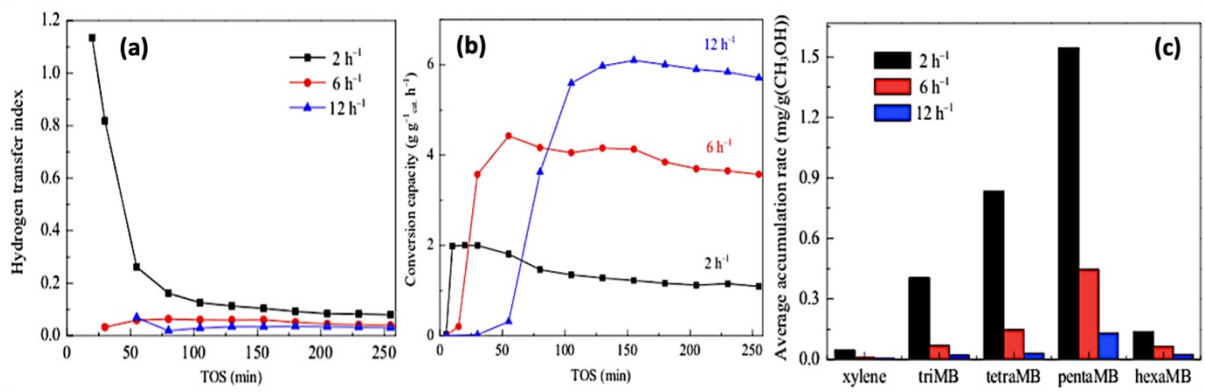

Figure 22 – (a) Hydrogen transfer indexes and (b) conversion capacity over TOS. (c) Average accumulation rates of retained aromatics, at different methanol WHSV over H-ZSM-5 Si/Al=19 at 300° C. Retrieved from [113].

For high contact times the side reactions dominated by aromatic methylations and hydrogen transfer are favoured. This resulted in the accumulation of active aromatic species inside the zeolite (coke); thus, a faster deactivation as well. Relevant to note that, at conversion higher than 80%, olefin methylation (propylene methylation in a greater extent) become responsible for an increase in C_4 olefins and decrease in propylene selectivity.

Shorter contact times (high WHSV) restrict the generation of aromatic species, limiting the extent of hydrogen transfer reaction (**figure 22-(a)**). Inherently, a lower conversion capacity at the initial stages of reaction is observed and explains the increase in propylene and butene selectivity as these olefins are preferentially formed by methylation and cracking reactions on the alkene cycle.

At high WHSV the reaction path follows with more active intermediates in the medium as methanol feeding increases, increasing the overall methanol conversion capacity and olefin production over time, driving the predominance of alkene methylation and cracking reactions cycle in the dual cycle mechanism.

The main retained species found (**figure 22-(c)**) were xylene and polyMB, with a higher predominance of pentaMB and tetraMB (likewise found in Ibáñez's work). These species resulted from the referred hydrogen transfer reactions as well as oligomerization cyclization secondary reactions, are predominantly responsible for active intermediates in the aromatic cycle path at low WHSV, resulting in the product selectivity towards lower olefins **[109, 113]**.

Moreover, the major active intermediates found were pentaMB+, diMCP+ (dimethylcyclopentenyl cation), and triMCP+ (trimethylcyclopentenyl cation), provided that hexaMB and heptaMB+ are too large species to generate and work efficiently in the reduced intersections of the 10-membered ring channels – supported by several works **[71, 79, 87, 113]**.

Losch et al. better formalized the previous conclusions, expressing the linear correlation between the increase in propylene (expressed by the ratio of propylene/ethylene) from 5.5 to 8 by the increase in WHSV (from 1 to 7 $g_{MeOH}/g_{cat}.h$) **[114]**.

As final remarks, higher contact times (i.e., higher W/F and lower WHSV) lead to higher oxygenate conversion, shortened induction periods, and higher proliferation of hydrogen transfer reactions. The predominance of the aromatic cycle reaches a maximum at moderate conversions (inflexion point), which is a behaviour common to the product distribution (e.g., propylene maximization) as well. Furthermore, at high contact times (higher than 80%), propylene selectivity decreases as olefin methylation reactions are promoted, while aromatic methylations and hydrogen transfer contribute to the accumulation of aromatic species inside the zeolite (coke deposition).

Effect of Operating Conditions: Methanol Partial Pressure

Only a scarce number of studies on reaction pressure and methanol partial pressure have been performed. At constant temperatures and fixed contact time, decreasing methanol partial pressures improve propylene yield whilst decreasing selectivities towards ethylene, aromatics, and paraffins **[110]**. This reflects higher olefinic yields as alkene methylation reaction are favoured in detriment of the suppression of aromatization reactions. At the same time, lower methanol partial pressure is responsible for lower reaction rates, higher olefinic yields (**figure 23**) **[110]**.

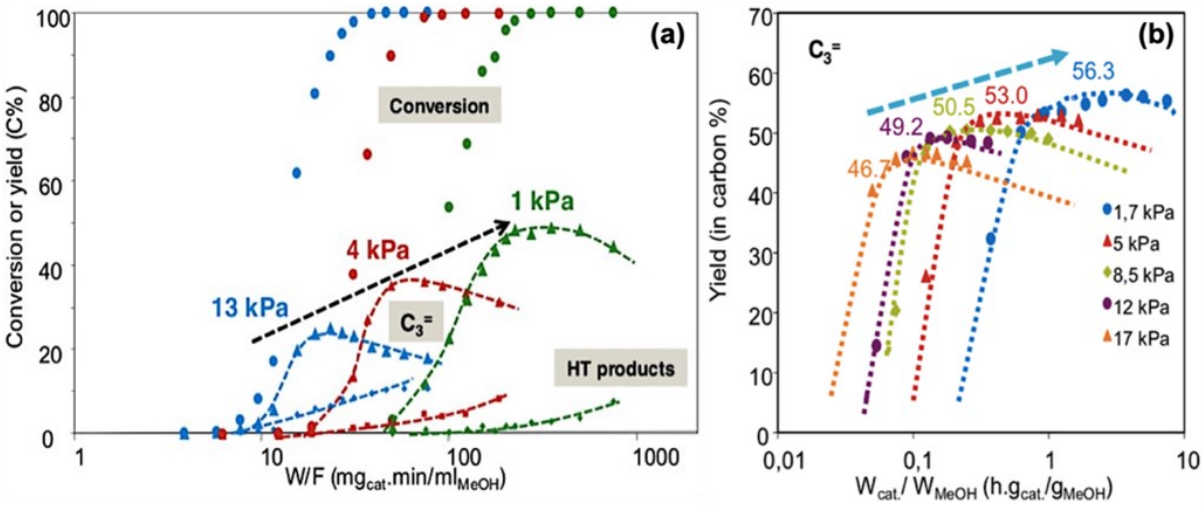

Figure 23 – (a) Methanol partial pressure effect over methanol conversion and hydrocarbon products, (b) propylene yield, as a function of contact time (at 450º C and over H-ZSM-5 Si/Al=90). Retrieved from [110].

Results showed not only higher propylene selectivity but also higher pentene selectivities, along with lower ethylene, butadiene, and C_{6+} products **[115]**.

With the modulation of the previously discussed data, it was possible to correlate methanol partial pressure with the reaction rate constants k_1 and k_2 to olefin formation and aromatization, pointing out to reaction orders of 0.9 and 2.1, respectively **[110]**.

Worth noting that, especially in Lurgi's industrial process, methanol streams are usually diluted in large quantities of water (which is also a reaction product) to facilitate the control over the reaction's temperature **[110]**. Not only this reduces the amount of coke deposition but also shifts the reaction kinetics by reducing methanol partial pressure whilst increasing propylene production **[110, 116]**. Despite higher propylene yield, this effect is accompanied by drawbacks of lower methanol conversion rates and added difficulties in product separation processes **[116]**.

Effect of Operating Conditions: Co-feeding

It has been observed that at industrial process conditions similar Lurgi's, co-feeding small aromatic molecules (16-32% of carbon content in the feed, such as p-xylene, toluene, and benzene), has a negative effect on propylene yield **[110]**. This is attributed to the lower diffusion/transport hindrance of aromatics (especially at low methanol conversions) which decreases the alkene cycle propagation and promotes aromatics methylation, methane, and ethylene formation.

Ilias et al. (2013) further studied the effect of co-feeding hydrocarbons on product selectivity, aromatic/alkene cycle's contribution ratio, and on the alkane to alkene ratios (A/A) **[112]** (**figure 24**). At 275º C (548 K), 5.4% of co-feeding of propylene and toluene, and iso-conversion (17.9–18.6% DME; 52.3 and 40.3% for propylene and toluene), it was found that feeding of light olefin contributes to the propagation of the olefin cycle by increasing in selectivities towards C_4-C_7.

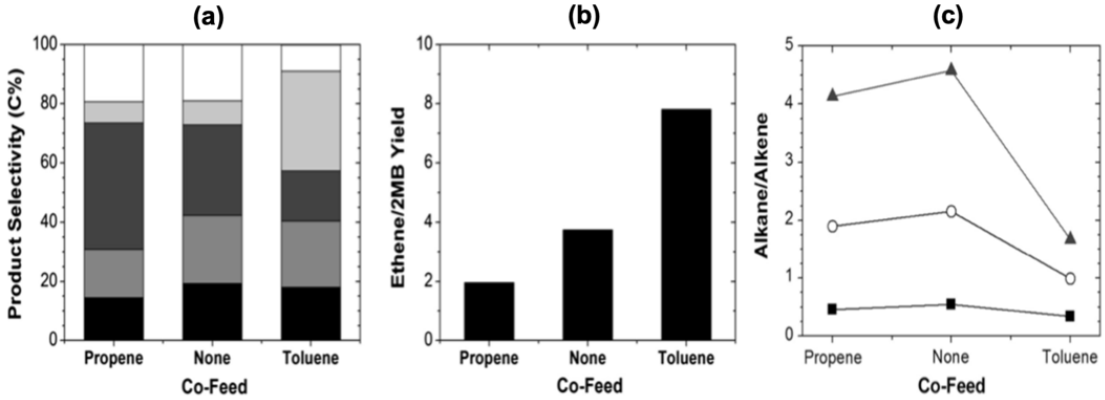

Figure 24 – For the feeding of P_{DME}=0.7 bar and $P_{co\text{-}feed}$=0.04 bar, for the conversion of olefins over H-ZSM-5 Si/Al=42.6 on a carbon basis: (a) product distribution (black: C_2; medium grey: C_3; dark grey: C_4-C_7; light grey: MB; white: others), (b) ethylene/2MB ratio and (c) alkane/alkene ratio (▲: C_6; ○: C_5; ■: C_4) as functions of co-feed at 548 K and 548 K and 17.9–18.6% DME conversion. Adapted from [112].

Co-feeding toluene increased the relative propagation of the aromatic cycle in accordance with the previous discussion, mostly by shifting the production of C_4-C_7 to aromatics. It also verified a very slight reduction in propylene's yield while the co-feeding propylene also contributed to the same effect, alongside lower ethylene selectivity. This observation ponders the premise that the great majority of propylene and ethylene is produced by the alkene and aromatic cycle, respectively, while smaller amounts are produced by the conjugated dual cycle (higher relative formation in the case of propylene). Another relevant scope to analyse is the concept that alkanes are the alkene's cycle termination products (formed by olefin hydrogen transfer reactions) **[112]**.

Alkane species can be formed through hydrogen transfer reactions and present lower reactivity than olefins or aromatics **[112]**. The extent of these reactions may be evaluated from the alkane/alkene cycle which has been observed to increase with increasing DME conversion and decrease with temperature **[112]**. As the extent of this, it was observed that the decreasing ratio of alkanes to C_6-alkenes follows the same trend as decreasing ethylene/2MB (E/2MB) as the aromatic cycle is favoured with co-feeding of toluene (**figure 24**).

Effect of Acidity

According to previously reviewed references, the MTO reaction is thought to occur predominantly in the strongest Brønsted acid sites in the micropores of the zeolite **[109]**. Losch in his studies developed a very representative graphic summary of a literature review from the last works on the effect of acidity in C_2-C_4 selectivity **[73]** (**figure 25**).

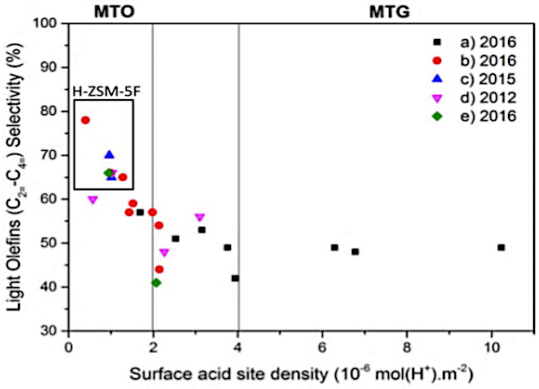

Figure 25 – Correlation between surface acid density and product selectivity towards light olefins ($C_{2=}$-$C_{4=}$) over H-ZSM-5 zeolites. Retrieved from [73].

The results described a trend where lower surface acid site density contributed to a higher light olefin selectivity. This observation led to the conclusion the lower acid site density (in some cases accompanied by larger zeolite crystal sizes) the higher the selectivity of Brønsted acid sites towards lower olefins, suggesting a predominance of the alkene methylation-cracking cycle.

The nature of the acid sites is a relevant parameter. In literature, it is incredibly difficult to find studies that directly compare the performance of purely H-ZSM-5 with different acidities, a controlled synthesis (that is, proposedly synthesized with certain Si/Al ratios rather than dealuminated or passivated), with equivalent reaction conditions.

It has been verified that, for similar crystal sizes and textural properties, with increasing Si/Al ratio the total amount of acid density in the catalyst also decreases but the acid site strength increases **[62, 121]**. Provided that acid sites derive from aluminium centres, the depletion of these atoms in the framework will certainly increase surface electronegativity to favour the acid strength.

Medium Brønsted acidity has also been linked to higher propylene yield and the overall product distribution above all else **[62, 121]** (**table 2**). As strong acid sites increase the formation of coke and lower light olefin production, having, therefore, a better catalytic performance modified catalyst with lower acid strength and higher low/moderate acid sites - due to slower channel blockage by shifting the reaction rate towards the alkene route – and dominance of the aromatic cycle in highly acid catalysts (both in regard to increasing crystallize size and aluminium content) and thus higher ethylene selectivity **[116, 117, 121]**.

Table 2 – Acidic properties of H-ZSM-5 and respective light olefin (C_2-C_4) product distribution with different Si/Al ratios, at steady-state, during multiple pulse experiments at 280º C with a methanol feed per pulse equivalent to twice the number of BAS in each catalyst. Adapted from [121].

Si/Al	MeOH	acidity by NH_3-TPD (mmol/g)			BAS Distribution (%)				Product Distribution (%)		
	Conv. (%)	total	weak	strong	weak	medium	strong	external	$C_{2=}$	$C_{3=}$	$C_{4=}$
20	14.9	0.58	0.31	0.27	16	16	68	7	7.2	41.2	12.1
40	14.3	0.56	0.22	0.34	17	17	66	5	3.7	47.7	16.8
80	13.1	0.24	0.09	0.15	4	20	76	5	9.0	48.9	19.1
160	14.2	0.10	0.02	0.08	16	4	80	-	1.2	43.9	25.5

Recent studies elucidated that, zeolites with different Si/Al ratios show an increase in propylene selectivity with increasing Si/Al ratio which can be studied by the ratio of ethylene and 2MB ($C_{2=}$/2MBu) as a measure of cycle predominance (aromatic/alkene ratio) per **figure 26 [118]**.

Additionally, a critical value of acid density (expressed by $[AS]_S$) has been found as crucial for achieving maximum propylene yields, as well as high strong/weak total acid site ratio, have been found the value of 0.175 μmol/m^2 and 3, respectively, for the H-ZSM-5 Si/Al=1600 (at 450º C and atmospheric pressure), likewise found at 350º C and low conversions (46-52% iso-conversion), **figure 26 [118]**. Conversely, Feng et al. (2020) ascribed a better catalytic performance for propylene to the relatively low content of strong acid sites **[119]**.

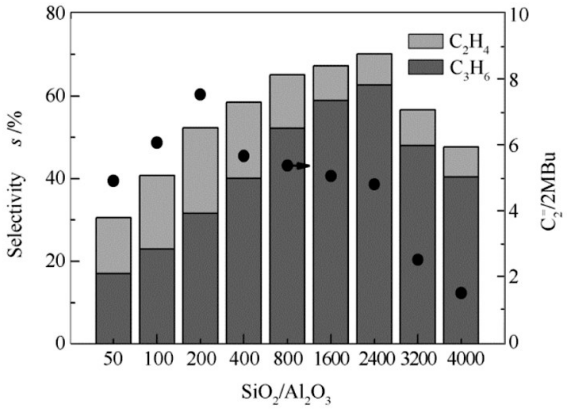

Figure 26 – Selectivity towards propylene and ethylene (bars) and $C_{2=}$/2MBu ratios as functions of SiO_2/Al_2O_3 (near 100% methanol conversion, 450º C, 1 bar, WHSV=9.72 h^{-1}). Retrieved from [118].

Other studies further dived into the nature of Al_F atoms, distinguishing between fractions of single and pairs, and it has been found that (for the same Si/Al ratios and crystal sizes), Al_F pairs promote butylene oligomerisation and hydrogen transfer reactions while single fractions promote butylene cracking **[115, 120]**. Additionally, it was found that the aromatic cycle produces ethylene and propylene in similar amounts whereas the alkene-based cycle appears to have a propylene predominance **[115, 120]**.

Generally, propylene selectivity appears to be improved with increasing Si/Al ratios, but the available catalytic data and catalyst characterization studies do not allow for irrefutable conclusions. Lower catalyst acidity, with has been linked to higher relative strong Brønsted acidity, appears to be

responsible for promoting the aromatic cycle. This trend is observed until a critical Si/Al ratio (i.e., critical weak/strong acidity or strong BAS/total LAS), where the alkene cycle is promoted thereon.

Effect of Zeolite Modifications

Zeolite modification is one of the broadest categories. Modifications can imply different synthesis methods, insertion of metal, dealumination, desilication, etc.

Gorzin and colleagues (2018) dived into the modified H-ZSM-5 to further understand the effect of metal impregnation in high silica catalysts in the MTO reaction **[122]**. Chen et al. (2015) and Zhang et al. (2010) had already dedicated studies to the same, specifically, the study case of H-ZSM-5 (Si/Al=38) with magnesium insertion and calcium insertion, respectively **[123, 124]**.

In Chen's work magnesium impregnation was applied over the hydrothermally synthesized H-ZSM-5 Si/Al=[40, 50] forming different nMg-ZSM-5 (n referring to the loading of magnesium) **[123]** (**figure 27**). With different impregnation loads, a decrease in crystallinity to up to 10% was observed derived from the subjacent framework dealumination. Furthermore, it was found that structural integrity (crystallinity) is not directly correlated with catalytic activity. 4.0 Mg-ZSM-5 showed the best catalytic stability and the highest propylene yield. It was verified an increase in catalyst activity/stability by impregnation, 3.87% higher propylene yield (~53%), and higher stability when comparing to the parent H-ZSM-5 despite framework destruction.

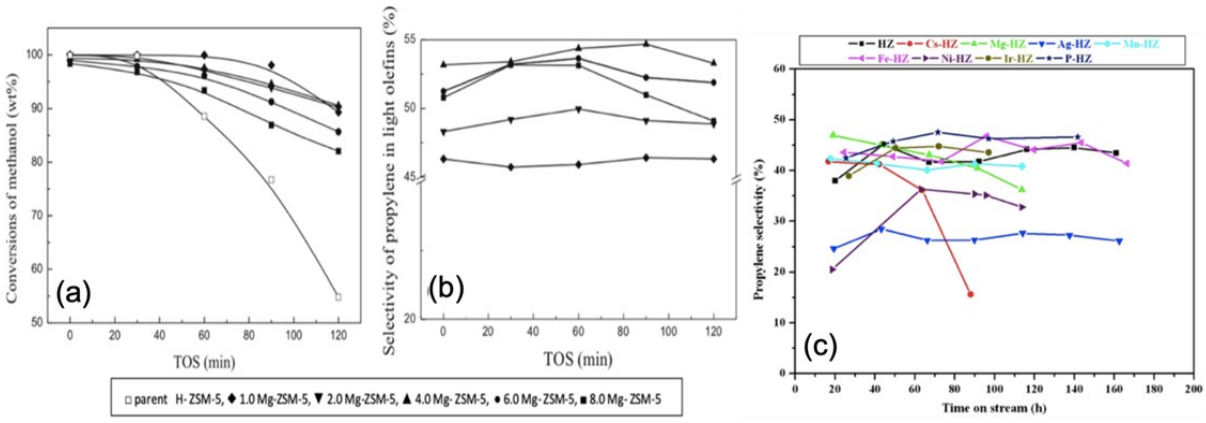

Figure 27 – (a) Conversion of methanol and (b) propylene yield, over parent and modified H-ZSM-5 by impregnation of Mg with different loads (450º C, 1 atm, pure methanol feed, WHSV 9.78 h^{-1}, W=1g, near 100% conversion) [122]. (c) Propylene yield over parent and modified H-ZSM-5 catalysts by metal impregnation (50% wt) (480º C, 1 bar, feed 50% methanol/water wt%, WHSV 0.9 h^{-1}, near 100% conversion) [122].

It was found that these additions in the catalyst's framework mainly interact at the level of Brønsted acidity and decreased both the strength and overall acid density (for weak and strong acid sites). This directly enlightens the increase in the lifetime of the catalyst as coke is mainly formed in the strong active sites.

The catalytic studies of modified H-ZSM-5 catalyst by similar metal impregnations conducted by Gorzin's (2018, Si/Al=200), Mohammadrezaei (2012, Si/Al=246), and Valecillos (2019, Si/Al=40) all found similar catalytic results accounting for a 5% uncertainty interval **[122, 125, 126]**.

The first work found similar crystallinity and surface area (over 95%) on modified catalysts and a similar decrease in acidity and Si/Al ratio with impregnation **[122]**. Gorzin concluded that propylene yield was not only strongly affected by the structure and acidity of the catalyst but also strongly by the texture and type of promoter **[122]**. The best catalytic performances (stability and by-products production) were attributed to the moderate density and acid site distribution.

Valecillos et al. (2019) studied phosphorous (PZ5) and zinc (ZnZ5) modified ZSM-5 zeolites (which aimed for similar ratios of P/Al or Zn/Al). Noticeably, the study showed H_3PO_4 (phosphorous source) slightly alters the zeolite acidy by desilicating framework silanol groups (SiH_4O) and dealuminating part of the Al_F **[126]**. As a result, slower induction, autocatalysis, and deactivations periods are observed whilst maintaining reaction mechanisms. On the other hand, ZnCl (zinc source) exchanges the ammonium cation in Brønsted acid sites with zinc atoms (conferring a Lewis acidity nature) - translated into the predominance of the alkene cycle (with hexaMB as the main intermediate) with a slower degradation of the aromatic species and slower hydrogen transfer rates, resulting in the enhancement of propylene selectivity (+10%), reduced coke formation (-42%), expansion the catalyst lifetime (+80%) (**figure 28) [126, 127]**.

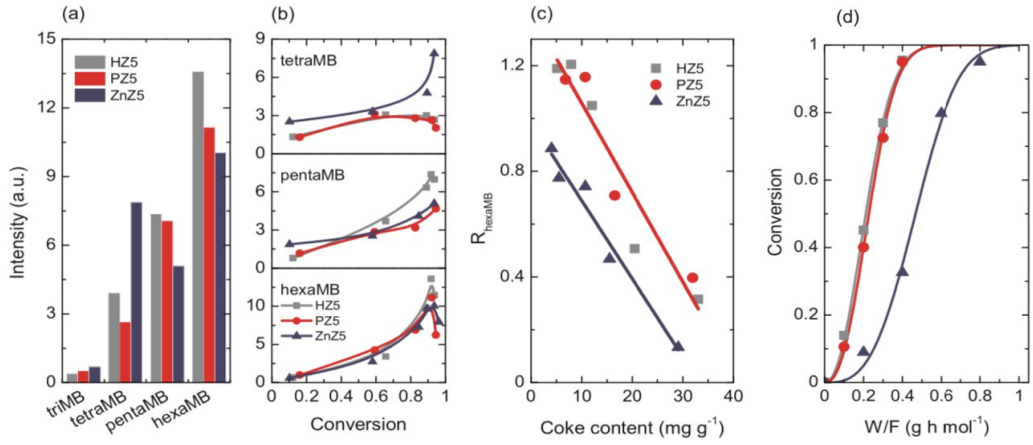

Figure 28 – (a) distribution and (b) evolution of retained species after the MTO reaction at TOS 90min, (c) relationship between coke and ratio of HMB and the rest of the retained species (R_{hexaMB}), (d) autocatalytic behaviour the reaction at initial conversion as a function of conventional space-times (W/F). Adapted from [126].

Concluding remarks should note that, these insertions suppress the aromatic cycle while they are also responsible for the dealumination of the zeolite framework which leads to the introduction of mesoporosity and Al_{EF} species that exhibit a Lewis acidity in their nature (Mg>Ca>Sr>Ba rank in terms of Lewis acid site strength) **[57, 61, 97]**. These verifications support the hypothesis that to maximize propylene's yield, a compromise between Brønsted and Lewis acidity is necessary.

Other works on hierarchical zeolites (materials containing two or more types of pores of different size, typically with less transport/diffusion limitations) have also shown great improvements regarding catalytic performance and reduction of coke deposition as higher specific surface areas, more micro and mesopore volumes, and more medium strength acid sites (in detriment of strong and weak acid sites) and a significant improvement in enhancing the light olefin yield (whilst showing a maximum modification level a decline in these properties is observed) **[119, 128, 129]**. Furthermore, the work of Schmidt et al. resulted in the observation that as microporous zeolites verify a stronger accumulation of coke species in the outer shell of the particle, in hierarchical material it is verified a homogeneous distribution of carbonaceous species over the zeolite's particles **[89]**.

Weissenberger investigated the performance of intracrystalline mesoporous, intracrystalline macropores and a zeolite with intracrystalline meso and macropores-induced modifications on ZSM-5 zeolites maintaining approximately the same Si/Al ratio (101-111) and Brønsted acidity (0.186-0.190 mmol/g) **[130]**. The best performance was found for meso and macropores induced modifications zeolite as it combined both the advantages of mesoporosity and macroporosity. The first is directly related to enhancing the resistance against deactivation by coke (due to increased external surface area) and the latter is associated with reducing the coke formation. This resulted in prolonging the catalyst lifetime with a better lower-olefin and propylene yield over time (**figure 29**).

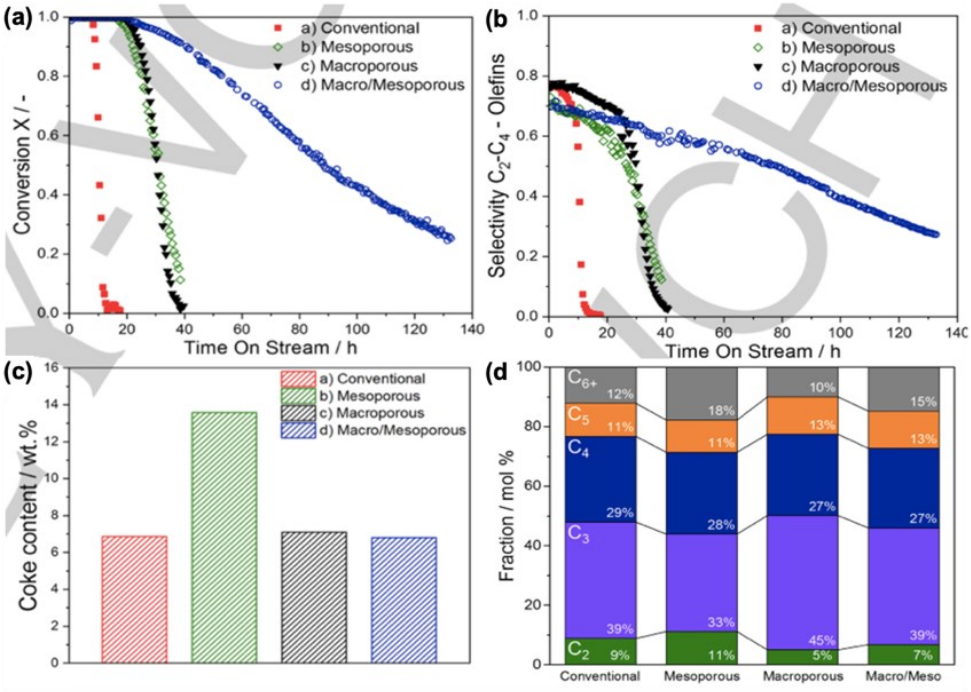

Figure 29 – Catalytic test results at 50 ml/min of helium saturated with methanol at 30º C, WHSV of 11 h^{-1}, 450º C, W=100mg. (a) Conversion of methanol and DME over TOS, (b) selectivity to lower olefins results evaluated by GC-FID, (c) coke content measurements by TGA after the last point in the conversion graph, (d) product distribution after 3h TOS. Retrieved from [130].

Research on the topics of hierarchical zeolites as well as nano and mesostructured materials, zeolite preparation with different synthesis methods and coatings, are on the rise as deeper understandings on MTO mechanisms are needed **[101, 114, 116]**.

2.6 *Overview*

The MTO process evolution across the decades was reviewed, from the most incorporated technologies to the indispensable environmental sustainability viewpoints. MTO appears as an emergent technology to satisfy propylene's increasing demand. Research focuses on the understanding of the complex reaction mechanism and how to improve propylene's yield. That is the groundwork for a great commercial expansion of the process, accompanied by economical-environmental sustainability. SAPO-34 and H-ZSM-5 zeolites are the main catalysts on which the literature focuses more. Contrasting with SAPO-34, H-ZSM-5's framework arrangement, stability, and versatile acidic properties allow for a complete study of MTO's mechanistic pathways.

This reaction has presented an autocatalytic behaviour where the rate of methanol and DME consumption increases with conversion. The dual-cycle mechanism is currently the most widely accepted proposal. HCP species formed at an initial stage react with methanol through a series of condensation, alkylation, cyclization, and hydrogen transfer reactions. These constitute the formally called aromatic and alkene cycles, which are thought to occur simultaneously. The alkene homologation cycle, responsible for producing C_3-C_7 olefins, has been documented to be favoured at higher temperatures and lower zeolite acidities. But this dependency appears to rely in a compromise between Brønsted and Lewis acidity, which can also be linked to strong and weak acid sites.

There is a major gap of studies performed with devotion to intrinsic kinetic data acquisition, in the absence transport phenomena (i.e., diffusion, heat, and mass transport limitations). Furthermore, most data are acquired at full conversion which is also completely undesirable to obtain reliable kinetic parameters in the absence of deactivation and predominance of secondary reactions.

Reliable of data is fundamental to study accurate kinetic parameters, compare experimental data, build reliable kinetic models, and optimize industrial processes. This disregard, risen from the difficulty to study this system and from unlighted objectives, has made data comparison a major challenge and obstructed the understanding of MTO. To maximize propylene's yield and catalyst lifetime, a comprehensive study of the influence of catalyst acidity, topology, and operating conditions on catalytic activity and selectivity is fundamental.

For that reason, in this work experiments will be aimed at oxygenate conversions between 20-80%, at steady-state, under intrinsic kinetics regime. The data acquired will be a descriptor of the effect of operating conditions on selectivity and catalytic activity, but it will also elucidate the mechanistic pathways of MTO by the study of zeolites with different acidities.

This work not only aims to indicate the industrial relevant maximization of propylene yield but also, a deeper understanding of the contribution of each cycle in the product distribution and their interdependence with acid site nature (LAS or BAS) and density. Temperature between 350-450º C will be used as this most industrially relevant range to maximize catalyst activity without a rapid deactivation.

3 *Procedures and Fundamentals*

3.1 *Catalyst Preparation*

During this experimental work ZSM-5 zeolites with silicon to aluminium molar ratios of 25 and 140 supplied by Zeolyst International were selected for the study of the effect of acidity in the MTO reaction. In addition, reference to the previous studies performed in the same investigation group by Bernardo Pessanha (2019), Marie-Elisabeth Lissens (unpublished, 2021), and Tingjun Lei (2020) with ZSM-5 with a silicon to aluminium ratio of 40 will also be mentioned in the results discussion **[131-133]**. **Table 3** indicates the correspondent commercial references for each ZSM-5 zeolite under discussion.

Table 3 – Commercial references of the ZSM-5 zeolites (supplied by Zeolyst International) with different acidities discussed in the present work.

Si/Al	Abbreviation	Commercial reference	Lot. Nº
25	S25	CBV 5524G	2493-98
40	S40	CBV 8014	2493-124
140	S140	CBV 28014	2493-136

All zeolites were studied in their protonic form, referred to as H-ZSM-5, for which calcination was performed under dry airflow. With this process, the removal of all ammonia and ion exchange to H^+ was assured, but also the removal of moisture, water from hydrated ores, volatile impurities, and organic matter **[134-136]**.

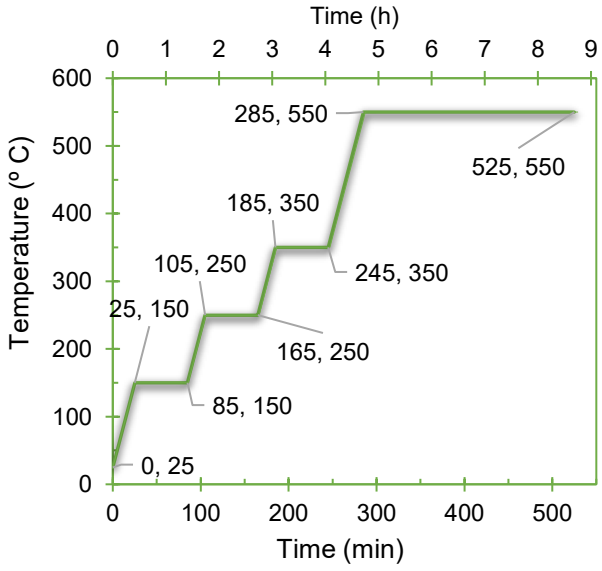

Figure 30 – Calcination program performed to obtain H-ZSM-5 zeolites.

The calcination program encompasses 4 heating steps until the last temperature stage of 550º C maintained for 4h. A constant heating ramp of 5º C/min was selected and 1h stages at 150, 250, and 350º C to ensure the structural stability of the zeolite throughout the calcination (depicted in **figure 30**) reflecting a process with a total of 8.75 h.

3.2 *Catalyst Characterization*

Inductively coupled plasma spectroscopy (ICP-OES) was carried out in IRIS Intrepid II XSP (an equipment from Thermo Scientific) by an outsourced laboratory (at UGent) in order to determine the elemental composition of the zeolites in aluminium, silicon, and sodium.

Powder X-ray diffraction (XRD) pattern was used for the evaluation of the purity and crystallinity of the samples, executed in an outsourced laboratory (at Ugent) with a 2θ range from 0.5° to 90°. Samples were analysed in a Bruker D8 Advance equipment with motorized anti-scatter screen and autochanger, using a LynxEye XE-T Silicon strip Line detector and a CuKα radiation source (Bragg-Brentano geometry).

Nitrogen physisorption (77 K) was performed to uncover information regarding the porosity nature of the catalyst and surface area. All the analyses were performed in the Micrometrics Tristar II apparatus between 0.01-1.00 p/pº. Beforehand, the samples (~0.3 g) were degasified for 8 h at 200º C to desorb any moisture still adsorbed on the surface or inside the catalysts' porous network.

Pyridine Fourier-transform infrared spectroscopy (py-FTIR) was also performed to characterize the acid site density and strength of each catalyst. This technique was executed in an outsourced laboratory (at IST). Succinctly, the experimental procedure consisted of outgassing the sample (~20 mg) under vacuum (lower than 10^{-5} Pa) at 450 °C for 2h, after which the sample IR spectrum was acquired by subtracting the background spectrum of the empty cell. After releasing the vacuum, the sample was cooled down and stabilized at 150º C where a background spectrum was recorded. It followed successive releases of small portions of pyridine, intercalated with outgassing of physiosorbed species. This was repeated until no further changes in the peak intensities were observed in the differential spectra (background spectrum at 150º C subtracted from sample spectrum). Differential spectra were acquired for 150, 250, 350 and 450º C for each catalyst sample.

3.3 *Intrinsic Kinetic Data Acquisition in Heterogeneous Catalysis*

MTO reactions were carried out at constant pressure (system pressure of 3.5 bar and methanol partial pressure of 0.4 bar) in a continuous packed bed tubular reactor (PBR). Catalyst loading varied according to the foreseen experimental conditions (temperature, W/F intervals) and H-ZSM-5 zeolite acidity.

The catalytic reactor was pre-heated overnight under a constant flow of nitrogen (also used as a dilutant). The effluent stream was analysed by an Agilent Technologies 6850 series II network (GC online system), equipped with a flame ionization detector (FID) and a Rtx-DHA-150 column (fused silica). The first analyses were conducted approximately after 90 min on stream. The conversion was defined as the percentage of oxygenates (methanol and DME) consumed during the MTO reaction. The yield of each hydrocarbon product was calculated on a carbon-basis to the molar amount of methanol converted.

3.3.1 *High-Throughput Kinetic Setup*

The high-throughput kinetic setup (HTK) is a heterogeneous catalysis investigation setup designed by Zeton B.V. for intrinsic kinetic studies in a broad range of operating conditions. It consists of four independent reaction blocks that culminate in a common analysis zone. Each block is equipped with a specific feed section and a heating bock with two parallel isothermal reactors. These can be used simultaneously at the same temperature and pressure as they share the same heating blocks and the same pressure regulating system. The entire setup is regulated by both in situ pressure controlling systems (valves and needle valves) and a specific setup software developed by Zeton (NI LabVIEW 2014 and NI MAX). More supportive information can be found in **Annex A1**.

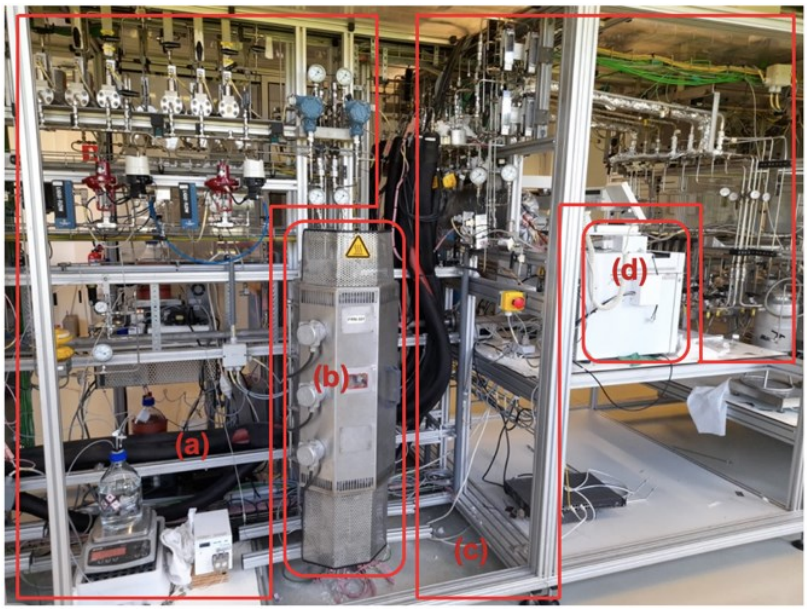

Figure 31 – HTK setup block 2: (a) feed section; (b) reactor block; (c) effluent section; (d) online gas chromatographer (Agilent Technologies 6850 series II network)

During this experimental campaign, block 2 was used and only one reactor (R4) was operated for the experiments due to the malfunctioning of the liquid mass controller in the feed section, problems regarding pressure regulation, and the overall high occupancy of the setup by other users which restricted the analysis frequency and attached specific complications.

The experimental block can be divided into 4 sections: feed section, reactor block, effluent section, and online gas chromatographer (**figure 31**). During catalytic experiments, methanol and nitrogen (as a diluent) were used from the liquid and high-pressure gas feeding lines. The catalytic reactions occurred in the tubular reactor R4 where partial pressure of methanol was kept at 0.4 bar (total pressure of 3.5 bar) while studying the catalysts at temperatures ranging from 350 to 450º C. Heated lines were used in order to ensure temperatures above the dew point of the gaseous mixture from the exiting stream of the tubular reactor to the analysis section.

3.3.2 *GC-FID effluent analysis*

Gas chromatography (GC) is a separation method to detect small components in a gaseous or liquid sample that is vaporized at the injection port. The mobile phase, where nitrogen was used as the carrier gas, moves the analyte throughout the fused-silica column (polar stationary phase) where the separation occurs. The components with higher affinity towards the stationary phase (non-polar components) elute last. The FID coupled to the GC detects the carbon content of the sample as the analyte passes through hydrogen-fuelled flame producing carbon ions, which are then measured by electrodes **[137, 138]**.

The output is obtained in relative peak areas, which are proportional to the carbon mass fraction of the effluent. For every analysis, in the GC software (Agilent OpenLAB), the correction of the method regarding the retention times of some of the split peaks is necessary as the change of small split seconds heavily impacts the relative areas of lower olefins.

To obtain quantitative results, for some of the components a correction factor needs to be multiplied with peak area fraction, according to Dietz et al. (1967), with respect to the function of response of the FID **[139]**. Since water is one of the reaction products, per the dehydration step of methanol to DME, and it is undetectable by this technique, the overall final mass balance takes into consideration this correction for the calculation of the molar flow rates of each component in the effluent, **equation (1-2)**.

$$O^{in} = O^{out} \Leftrightarrow O^{in}_{MeOH} = O^{out}_{MeOH} + O^{out}_{DME} + O^{out}_{H_2O} \Leftrightarrow$$
$$\Leftrightarrow \dot{m}^0_{MeOH}\frac{M_O}{M_{MeOH}} = \left(\dot{m}^0_{MeOH} - \dot{m}_{H_2O}\right)x^*_{MeOH}\frac{M_O}{M_{MeOH}} + \left(\dot{m}^0_{MeOH} - \dot{m}_{H_2O}\right)x^*_{DME}\frac{M_O}{M_{DME}} + \dot{m}_{H_2O}\cdot\frac{M_O}{M_{H_2O}} \quad (1)$$

$$F_k = \frac{x^*_k \cdot \left(\dot{m}^0_{MeOH} - \dot{m}_{H_2O}\right)}{M_k * 3600} \quad (2)$$

where m^0_{MeOH} and $\dot{m}_{H_2O}$ represent the mass flowrate (g/h) of methanol (feed) and water (outlet). Moreover, x^*_k represent the corrected mass fractions (with Dietz et al. correction factors) and the molar mass of species k, respectively. F_k designates the molar flow rate (mol/s) for the hydrocarbon species k in the effluent.

Although the reaction feed is only constituted by methanol, both methanol and DME are considered reactants as the equilibrium between the two species are swift and both participate in the conversion to hydrocarbon species. Therefore, both conversion (X_{oxy}) and selectivity (S_k) regard the transformation of oxygenates into hydrocarbons, the latter calculated on a carbon base, according to the following **equations (3-4)**. Due to the high complexity of the chromatogram, the identification and interpretation of every individual component is unviable so, components were divided in alkane, alkene, and cyclic compounds for selectivity considerations.

$$X_{oxy} = \frac{F^0_{MeOH} - (F_{MeOH} + 2F_{DME})}{F^0_{MeOH}} \tag{3}$$

$$S_k = \frac{nC_k \times F_k}{F^0_{MeOH} - (F_{MeOH} + 2F_{DME})} \tag{4}$$

where F^0_{MeOH}, F_{MeOH} and F_{DME} represent the molar flow (mol/s) of methanol in the feed, and molar flow of methanol and DME in the effluent, respectively. nC_k and F_k symbolise the number of carbon atoms and molar flow rate (mol/s) for the hydrocarbon species k in the effluent.

3.4 *Intrinsic Kinetics*

The acquisition of intrinsic kinetic data is fundamental to find reliable kinetic rate expressions and modelling, which are prerequisites for a safe, efficient, and economical reactor design on an industrial scale. These studies are scale-independent, performed in the absence of mass and heat transfer limitations, which affect both the activity and selectivity of the catalysts under study.

For this purpose, the pressure-drop of the catalyst bed, ideal plug flow behaviour, maximum bed dilution, external mass transport limitation, internal diffusion limitation, radial and external heat transport limitation, and the temperature gradient within the pellet, were considered. To assess these parameters, the EUROKIN spreadsheet for gas-solid fixed beds was used **[140, 141]**.

Feed composition, reaction conditions, properties of the catalyst and dilution, reactor dimensions, and reaction rate, constitute the input data for all intrinsic kinetic calculations with an initial overestimation of the observed reaction rate and activation energy by the correlation between preceding data. In **Annex A2** this unput data is exemplified as well as the range of catalyst bed compositions used.

In order to examine accurate kinetic parameters, not only do the catalytic studies are required to be performed under an intrinsic kinetics regime, but the data also compels an investigation of the state of deactivation of the catalyst throughout the experimentation period. One common approach involves stability studies, where for different conditions (temperature, space-time) it is investigated how much time on stream (TOS) the catalyst retains its unchanged activity. In the present work, deactivation was evaluated by a different method which will be explored in detail in further chapters.

The calculation of catalytic activity coefficients in early stages of the experimental set is relevant as the single analysis of conversion profiles does not always evidence deactivation when short conversion ranges are studied. This analysis is also of special relevance as the first data points allow for the validation of the overestimated parameters used for intrinsic kinetics calculations and stability period to continue with the experimental campaign.

3.5 *Catalytic Activity*

In the present work, the calculation of catalytic activity was used both for the analysis of the effect of deactivation and for the study of kinetic parameters. A first order kinetics (**equation (5)**) was assumed throughout the calculations and the correlations for a continuous fixed bed tubular reactor (neglecting any pressure drop) were used to estimate the kinetic parameters from the linear regression of **equation (6)**.

$$-r_{MeOH} = k_{app} \cdot P^0_{MeOH}\left(1 - X_{oxy}\right) \tag{5}$$

$$W/F = \int_0^{X_{oxy}} \frac{dX_{oxy}}{k_{app} \cdot P^0_{MeOH}\left(1 - X_{oxy}\right)} \Leftrightarrow \ln\left(1 - X_{oxy}\right) = k_{app} \cdot P^0_{MeOH} \cdot W/F \tag{6}$$

With respect to the conversion of oxygenates under a constant methanol partial pressure feeding (0.4 bar) at a given temperature, the regression of $\ln\left(1 - X_{oxy}\right)$ over W/F (space-time) gives the apparent reaction rate constant, k_{app}, as the slope.

This parameter, obtained for different experimental temperatures, allows the calculation of the Arrhenius apparent activation energy ($-E_{A,app}$) and the pre-exponential factor (k_0) according to by the plot of **equation (7)**.

$$k_{app} = k_0 \cdot e^{-E_{A,app}/RT} \Leftrightarrow ln\left(k_{app}\right) = ln(k_0) + \frac{-E_{A,app}}{R} \cdot \frac{1}{T} \tag{7}$$

4 *Zeolite Characterization*

4.1 *ICP-OES*

This emission spectroscopy technique vaporizes and dissociates the analyte sample into its constituents' atoms and ions by using argon plasma to excite these particles to higher stages of energy **[142, 143]**. By measuring the intensity and emission wavelength of the electromagnetic radiation, unique to each element, it is possible to determine the relative molar abundance of each component **[142, 143]**. For the different acidity aluminosilicate zeolites studied, the compositions in silicon, aluminium, and sodium, can be found in **table 4**.

Table 4 – Elemental composition of H-ZSM-5 zeolites with different Si/Al ratios by ICP-OES analysis.

(%mol)	SiO_2	Al_2O_3	Na_2O_3	Si/Al_{ICP}
S25	98.2	1.8	0.01	27.2
S40 [a)]	98.7	1.2	0.01	40.5
S140 [a)]	99.7	0.3	0.01	158.5

[a)] Data retrieved from Pessanha (2019) [130] regarding the same catalyst origins used in the present experiments.

According to the supplier, the molar percentage of sodium should be approximately 0.05% **[144]**. The low content registered by ICP for this soft metal resembles the expected results. This verification ensures that all acid sites are provided by silicon and aluminium with little or no contribution from sodium which was previously discussed to source Lewis acidity.

The molar silicon to aluminium ratios obtained by the characterization technique presents the highest (positive) average positive deviation of 13% for H-ZSM-5 Si/Al of 140 in relation to the theoretical composition for the zeolite. This result is within the 15% uncertainty given for error's associated with the technique and the manufacturer's specifications. During the literature catalytic studies for different acidities, as the effect of acidity presents a hyperbolic behaviour (a decreasing function for lower acidity) the effect of this deviation can be considered negligible; thus, all results were as expected.

4.2 *XRD*

This technique is used for the characterization of crystallinity of the material, sample purity, and measurement of unit cell dimensions by X-ray scattering along with the sample. In principle, when two or more X-ray beams encounter atoms in an organized structure they can either have a destructive interference with each other cancelling out (predominant effect) or constructive interference, producing a diffraction pattern specific to the framework **[145-148]**.

The crystalline structure of ZSM-5 exhibits characteristic peaks which indicate the present MFI framework. At 2θ = 5 to 10º, two high-intensity diffraction peaks characteristic to these zeolites are found, while at 2θ = 23 to 25º the five characteristic peaks can be observed **[149]**, as indicated by **figure 32**. The peak at 2θ=23 was used as the reference peak for the relative intensity in order better distinguish the effect of silicon content in each sample at lower diffraction angles.

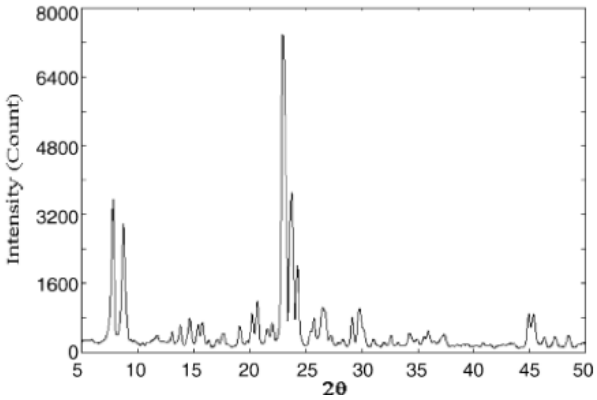

Figure 32 – Typical XRD pattern for ZSM-5 as MFI structure. Retrieved from [149].

Furthermore, the first diffraction peaks are known to be associated with higher silicon abundance, which often reflects a higher order of the mesostructured matrix **[150]**.

Figures 33 and **34** present the comparison between the XRD patterns for the zeolites with different acidities. The lower diffraction angle peaks present a higher intensity for the lower acidity zeolite as well as a higher intensity for the remaining peaks in the spectrum which is consistent with the expected. This effect was predominant for the comparison between Si/Al of 140 and 40 which is in accordance with the higher silicon content of this catalyst.

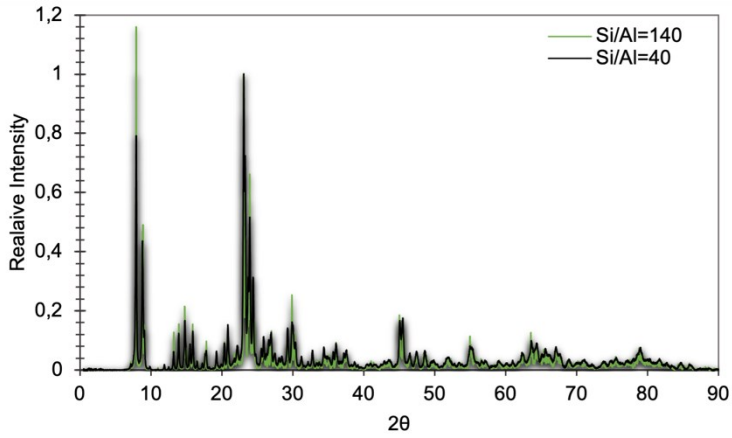

Figure 33 – Comparison of XRD patterns obtained for H-ZSM-5 Si/Al=140 and Si/Al=40.

The study of loss of crystallinity during the calcination is a reasonable hypothesis, but studies performed by Pessanha (2019) using the same catalysts and preparation conditions were performed indicating no effect of the framework of the catalysts as no significant decrease in intensity between

the 2θ = 23 to 25º peaks was observed **[151]**. Concerning the same peaks, the present studies appear to reveal similar crystallinity for Si/Al of 25 in comparison to Si/Al of 40.

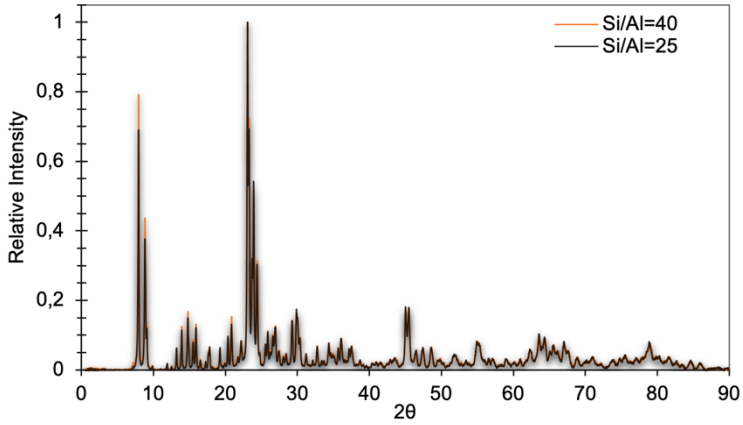

Figure 34 – Comparison of XRD patterns obtained for H-ZSM-5 Si/Al=25 and Si/Al=40.

All the obtained results are therefore as anticipated for this topology. The good resolution of all patterns indicates the high crystallinity of the samples and the absence of impurities.

4.3 *Nitrogen physisorption*

Physisorption is a characterization technique of porous solid or fine powders. Nitrogen sorption (77 K) takes place in the vicinity of the solid surface and outside the solid structure for materials with pores in the range of 0.5 to 50 nm **[152]**. The physical phenomenon occurs first in micropores (d_p < 2) at low relative pressures due to the large adsorption potential (van der Waals forces). At higher relative pressures, multilayer adsorption (> 0.1 p/pº), as well as the filling of the external surface of mesopores (d_p = 2-50 nm) and macropores (d_p > 50 nm), takes place **[152, 153]**.

Furthermore, the microporous volume, microporous surface area, and external area were determined by the t-plot method, whereas the external surface area and average pore diameter were attained by the Brunauer, Emmett, Teller (BET) method as recommend by IUPAC and the state-of-the-art literature **[153-155]**.

Figure 35 shows the adsorption and desorption isotherms for catalysts with Si/Al of 140, 40, and 25. The isotherms resemble both type I and IV which suggests both micro and mesoporosity with low pore volume as well as hysteresis loop type H4 (Si/Al of 140) and H3 (Si/Al of 25, 40). In the latter profile, associated with mesopores (and macropores), metastable adsorption (delayed capillary condensation from metastability of the adsorbed multilayer) is found due to possible pore blocking and cavitation effects which results in the display of a hysteresis loop profile isotherms **[156]**. Furthermore, this is correlated with a complex structure with important networking effects, with narrow wedge-shaped and slit-like pores for H3 and H4 **[152, 153, 157]**.

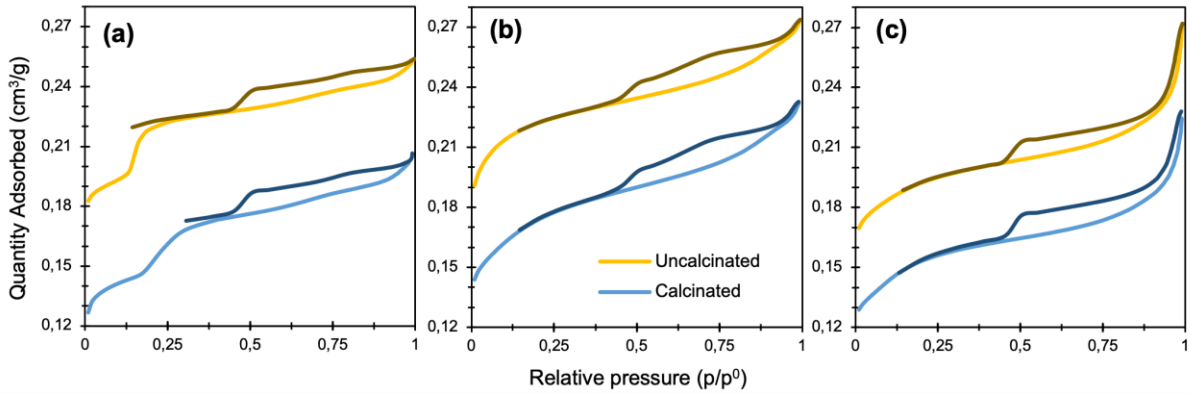

Figure 35 – Nitrogen physisorption isotherms of the commercial ZSM-5 with Si/Al of (a) 140, (b) 40, and (c) 25, for the calcinated (y = "quantity adsorbed" cm^3/g) and uncalcinated (y = "quantity adsorbed + 0.05" cm^3/g) forms.

The comparison between **figure 35-(a-c)** intends the similarity between the physisorption profiles of the calcinated and uncalcined forms of the catalysts (H-ZSM-5 and NH_4-ZSM-5, respectively). Since both forms of the catalysts for each acidity were analysed, the results were summarized in **table 5** with the relevant discrepancies evaluated as the ratio of the two values.

Table 5 – Nitrogen physisorption results for ZSM-5 with different Si/Al ratios, calcinated and uncalcinated forms.

Si/Al (Calcinated / Uncalcinated**)**	**25**	**40**	**140**
Volume			
Total (cm^3/g)	**0.21** / 0.20	**0.24** / 0.23	**0.21** / 0.21
Microporous (cm^3/g)	**0.10** / 0.10	**0.11** / 0.13	**0.07** / 0.03
Microporous (%)	**48** / 50	**47** / 57	**33** / 14
Surface area			
BET (m^2/g)	**349** / 324	**397** / 389	**371** / 393
Microporous (cm^3/g)	**207** / 291	**228** / 263	**141** / 70
Microporous (%)	**59** / 90	**57** / 68	**38** / 18
External (m^2/g)	**143** / 123	**168** / 126	**230** / 323
BJH adsorption average pore width (Å)	**53** / 60	**40** / 45	**29** / 25
BJH desorption average pore width (Å)	**49** / 61	**41** / 44	**40** / 41

Regarding the calcination effect on the catalyst structure, the most appreciable difference registered was the change in the relative microporous area and volume, according to **table 5**. The analysis the results for Si/Al of 140 indicate that calcination was responsible for the decrease external surface area and increase in micropore area and volume. Precisely the opposite observations were observed in the effect of calcination for S25 and S40. Overall, calcination did not substantially impact total pore volume, BET surface area or the average pore width (BJH desorption).

The effect of calcinations was most noticeable in S140, more than doubling the relative amount of micropores when compared to its uncalcinated form. Moreover, the ammonium forms of the catalysts presented a high similarity to the values for the total surface area given by the supplier.

Total pore volume did not fluctuate greatly and higher absolute values for microporous volume and area can be observed between the two forms of the samples.

S25 and S40 present very similar results (under 15% variation). Conversely, S25 (**figure 35-(c)** and **table 5**) presents higher relative (and absolute) microporous volume when compared to S140. Therefore, S140 stands out from the analysed samples with higher mesoporosity, which straightforwardly foresees lower catalytic activity, accompanied by lower deactivation rates and lower deactivation rates.

The physisorption results for protonated forms of the prepared catalyst are directly comparable with the findings in the literature, namely for the surface area of [425, 417, 332], and micropore volumes of [0.12, 0.16, 0.15] for Si/Al = [25, 50, 100] (retrieved from **[145, 118, 101]**, respectively) compared with [349, 397, 370] and [0.10, 0.11, 0.07] from the experimental results.

Deviations can be considered within the uncertainty associated with the technique and the variability of the zeolite calcination process and physisorption sample preparation (degassing, cell cleaning, etc.). The difference in nature of the porous structures (pore size and total pore volume) between the different aluminium content zeolites is fundamental to later explain the different product distributions and relation with associated acid site distribution. Certainly, this data is not enough to formulate a hypothesis or validate data as the strength of acid sites has shown to have a decisive influence; thus, py-FTIR is a fundamental part of the zeolite characterization studies.

4.4 *FTIR Spectroscopy*

FTIR is an absorption spectroscopy technique that gathers the vibrational spectrum of zeolites by the direct measurement of vibrational frequency from the different functional groups present **[88]**. It can be adapted for the adsorption of probe molecules in order to study the acidic properties, structure, and composition of the samples as these molecules adsorb at the surface functional groups (i.e., OH acidic groups) **[158, 159]**.

Among several strong bases, such as ammonia and amines, the application of pyridine (a weaker base than the latter) as a probe molecule enables the characterization of both nature and strength of Lewis and Brønsted acid sites (LAS and BAS). When adsorbed, this sensitive electric field probe causes a red shift on the OH group bands proportional to the acid site in the catalysts **[88]**.

This technique was used to study H-ZSM-5 samples with different Si/Al from the same calcination batch than the zeolite used in the catalytic studies: Si/Al of 25, 40, and 140 (regarded as S25, S40 and S140). This nomenclature will be used throughout the remaining of this work

4.4.1 *Zeolite IR Spectra*

H-ZSM-5's specific acid sites bands can be found positioned between 3800-3000 cm^{-1} – the ν(OH) stretching frequency region, **figure 36**. Lewis acid sites are regarded as cationic extra-framework species (and in some cases framework species, as tricoordinated Al) or as Al_{EF} species (non-tetrahedral Al, generally in octahedral geometry) cationic species such as Al^{3+}, AlO^{+}, $Al(OH)_2^{+}$ and $AlOH^{2+}$, but also AlOOH, $Al(OH)_3$ and Al_2O_3 **[160, 161]**. Brønsted acid sites are beheld as bridging hydroxyl groups **[160]**. The higher the band frequency, the stronger is the hydroxyl bond; thus, lower the Brønsted acidity strength since Al-O(H)-Si sites are less susceptible to release a proton **[160]**.

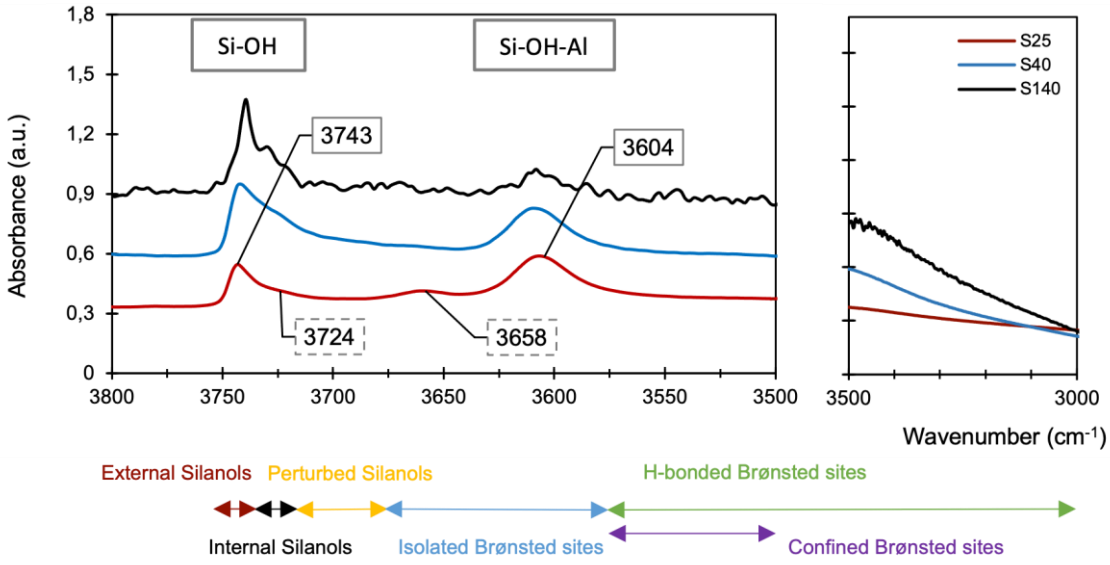

Figure 36 – IR background spectra for H-ZSM-5 samples with Si/Al of 25, 40 and 140, recorded at 450º C (normalized for a 20 mg pellet mass) with functional group attribution (design adapted from [160]).

The IR spectrum consists of essentially four major bands and three minor bands in this region. Due to the lower aluminium content, S140 clearly evidences best the presence of the main families of hydroxyl groups silanol structures, followed by S25 sample.

Firstly, 3600-3620 cm^{-1} presents itself as a high intensity band (comparative to the aluminium content) ascribed to framework (internal) bridging hydroxyl groups Al-O(H)-Si (strong Brønsted acidity) **[91, 126, 162-164]**. The low intensity band at 3660–3690 cm^{-1} is assigned to extra-framework Al-OH species (defect sites) which is by far more significant in the case of S140 and S25 **[162-164]**.

Next, terminal external silanol groups (Si-OH) can be found at 3740-3747 cm^{-1}. These have been demonstrated to hold strong acidity is several cases due to their location in vicinity of Lewis sites formed either by tricoordinated aluminium atoms ($_3$(OH)Al-O-Si(OH)O_3) or by tricoordinated silicon atoms ($_3$(OH)Si-O^--Al(OH)$_3$ or $_2OSi^+$-O-Si(OH)O_2) **[165]**. This band is complemented by the low-frequency shoulder/tail on the main band regarded as free internal silanol groups at 3720-3740 cm^{-1} **[88, 95, 126, 162]**. These bands are present in all zeolites, independent of topology and Si/Al

ratios, but are most evidently present in zeolites with low acidity (i.e., S140) and in higher relative abundance of strong BAS **[160, 165]**.

Ultimately, three bands located at approximately 3575, 3630 and 3700 cm^{-1} are attributed to H-bonded internal silanol groups, silanol nests (silanol groups interacting through extended hydrogen bonding), and Si-O-H--$Si_x(OH)_y$ groups **[164]**. These bands are almost imperceptible for all the catalysts with the exception of S140. The region between 3300−3580 cm^{-1} can be assigned to strong H-bonded Si−O(H)−Al sites or possible trace amounts of water **[162]**.

By observation of the spectra, all samples evidence Brønsted acidity and the presence of external silanol groups. These are the grounds for the use of different probe molecules for acidity quantification. Interestingly, S140 and S25 are distinguished by the greater presence of Al_{EF} species and structural defects (internal silanol groups and silanol nests).

4.4.2 *Pyridine Molecular Probing*

The interaction of pyridine with the zeolite framework results in the decrease of intensity of silanol and hydroxyl bridged IR bands at higher frequencies. As a results, new peaks emerge from pyridine's different aromatic ring stetch modes (υ_{8a}, υ_{8b}, υ_{19a}, and υ_{19b}). In **figure 37** the differential spectra are depicted for the zeolites with different Si/Al ratios at 150º C and 450º C.

The spectra of pyridine (and pyridinium ion) adsorption on H-ZSM-5's acid sites can be found in the region of 1700-1400 cm^{-1} (**figure 37**). The band at 1454 cm^{-1} is attributed to LAS which, as electron acceptor, is coordinatively bonded to pyridine (Py-L) **[95]**. At 1545 cm^{-1} is located the band for pyridine bonded to BAS (Py-B) **[158, 166, 167]**. Pyridinium ions are protonated by BAS and can be correlated with the IR band attribution observed in the OH region at 3610 cm^{-1} **[168]**. Brønsted acidity presents a high dependency with temperature, so it is possible to observe a drastic reduction in intensity from the respective bands, remaining only interactions with strong BAS at 450º C.

Pyridine species also adsorb on LAS and BAS at 1623 cm^{-1} and 1635 cm^{-1}, respectively **[167, 169, 170]**. Due to their proximity, they do not represent accurate measurements for the concentration of acid sites. The band located at 1491 cm^{-1} corresponds to an interaction of the probe molecule with both types of acid sites.

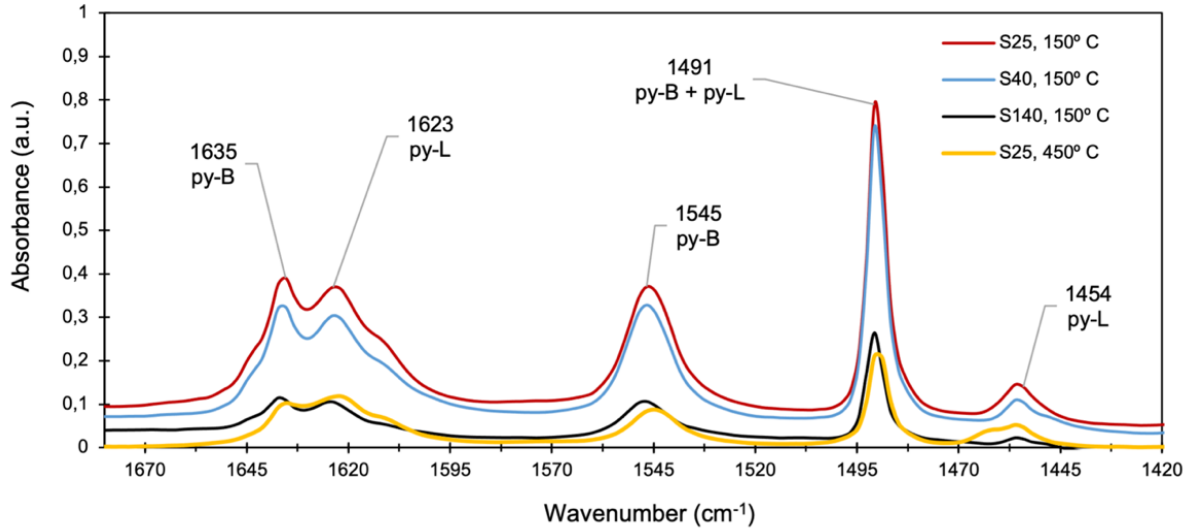

Figure 37 –py-FTIR differential spectra (normalized by the pellet weight) for H-ZSM-5 samples with Si/Al of 25, 40 and 140 (S25, S40 and S140), recorded at 150º C with acid site identification and for Si/Al of 25 (S25) recorded at 450º C.

At 1462 and 1494 cm^{-1} each band exhibits shoulders that become increasingly evident at 450º C. These are ascribed to the desorption of pyridine, more precisely, from C-H bending of aliphatic hydrocarbons bonded to oxygens in the catalysts' framework - which can be originated from pyridine cracking occurring at the acid sites above 323º C **[167]**. According to Barzetti et al. (1996), accurate quantitative results should therefore be acquired and compared below 250º C, always considering an estimation of 15% error for the absolute concentration of acid sites **[167]**.

Less evident peaks can also be found at approximately 1576 and 1397 cm^{-1} attributed to the interaction of the adsorbed species with LAS and BAS, correspondingly **[167]**. The band at 1600 cm^{-1} is attributed to physisorbed pyridine from hydrogen bonding with surface hydroxyl groups **[95, 167, 170]**.

At the characteristic absorption bands for both LAS and BAS, a broadening of the peaks (band shoulders) can be observed. This is usually attributed to electron deficiency at the acid sites, but also from interference from internal defects **[171]**. This effect is generally more evident with increasing silicon content which is not the only case for the zeolites in study. In addition to S140 (as predicted by the high amount of silicon), S25 also evidences higher amounts of silanol groups and structural defects – which was already suggested by the background IR spectra analysis.

The application of ^{29}Si and ^{27}Al MAS NMR would certainly clarify the results attained as a complementary analysis for of structural defects to quantify external and internal silanol groups, and distinguish between Al_{EF} and Al_{F}. Overall, according to the state-of-the-art knowledge, the presence of structural defects has been suggested to improve the catalysts' catalytic properties.

Although not studied, molecular probing with methyl-substituted pyridines (e.g. 2,4,6-collidine) could also of interest in future work as these larger molecules are not able to penetrate in

micropores of smaller dimensions, being inaccessible to SiO(H)Al Brønsted sites and internal silanol groups (including silanol nests) **[160]**. The use of these molecules that are too bulky to diffuse into the micropore cavities, it is possible to study the mesopore location and accessibility, as well as accessibility to active sites.

Acid Site Quantification

To determine the absolute acid site concentration in Lewis and Brønsted acid sites (n_{LAS} and n_{BAS}), the procedure described in Zambare et al. (2019) was used, according to the Beer-Lambert law with the molar extinction coefficients (Emeis, 1993) of 2.22 cm/µmol for LAS (ε_{LAS}) and 1.67 cm/µmol for BAS (ε_{BAS}) **[166, 167, 172]**. **Figure 38** depicts the experimental results regarding LAS and BAS concentration at 150º C (with a 15% error interval depicted) for S140, S40, S25, and corresponding literature values for the same catalysts. Since experimental results for S140 at pyridine desorption temperature 450º C were not possible to retrieve in time, in **Annex B** is described the approach to extrapolate these results, together with the remaining detailed experimental values and literature description.

As expected, an increase in acid density was confirmed with decreasing Si/Al ratios in **figure 38**. At 150º C, S25 presented the highest total acid site (TAS) density (269 µmol/g), followed by S40 (238 µmol/g), and S140 (63 µmol/g) lastly.

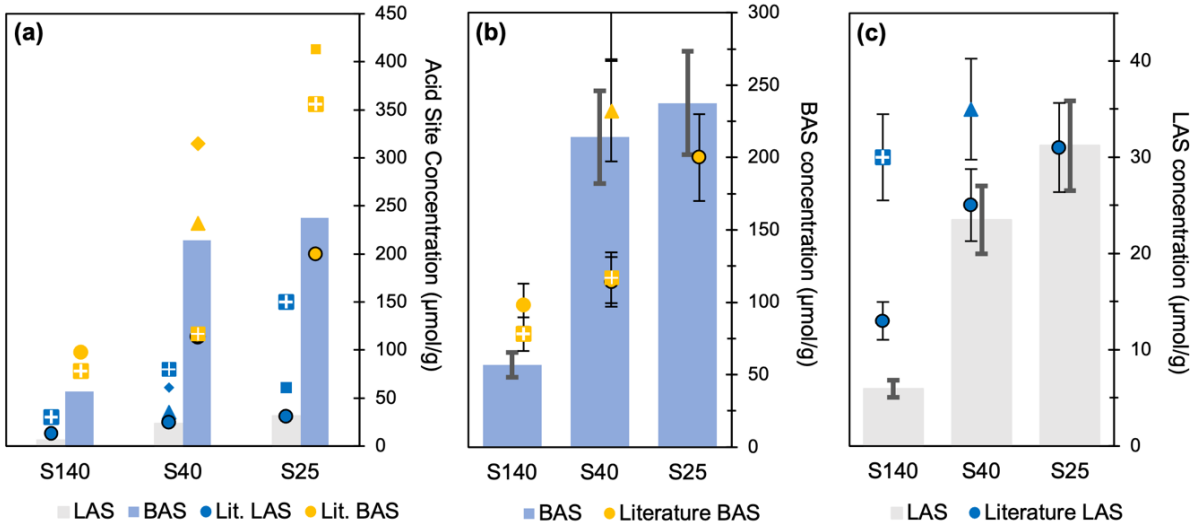

Figure 38 – (a) BAS and LAS, (b) BAS, and (c) LAS density quantification from py-FTIR studies at 150º C, for H-ZSM-5 S25, S40, and S140 samples (bars), with a comparison with literature works (⊞: [173],○: [93], △: [57], □: [149], ◊: [125], yellow filling: BAS, blue filing: LAS, examples better referenced in Annex B).

S40 presented a 10% decrease in BAS density from S25 and a 280% increase from S140. According to the error interval, the differences between S25 and S40 can be considered minor at

150º C. Additionally, S140 verified a decrease in almost 80% for both BAS and LAS density in relation to S25. This result agrees with the expected since 80% also corresponds to the variation in aluminium between the two catalysts.

The determined acid density results were mostly in accordance with the findings by Puértolas et al. (2015), Yarulina (2018) and the experimental data set analysed in the same laboratory previously (Auguste Fernandes, IST, unpublished). Results by Luz et al. (2007), although studied by ammonia TPD (NH_3-TPD), were also aligned with these conclusions.

Experiments of pyridine adsorption at 250º C, 350º and 450º C were also performed, which correspond to medium-weak, medium-strong, and strong acidities, respectively. **Figure 39** depicts the acid density obtained for each catalyst and the corresponding BAS/LAS ratios (with respective error bars). This analysis is of much more significance as not only strong (350-450º C range, which coincides with experimental conditions) and weak acidity (i.e., total acid site density) can be identified, but MTO is known to occur at the strongest acid sites.

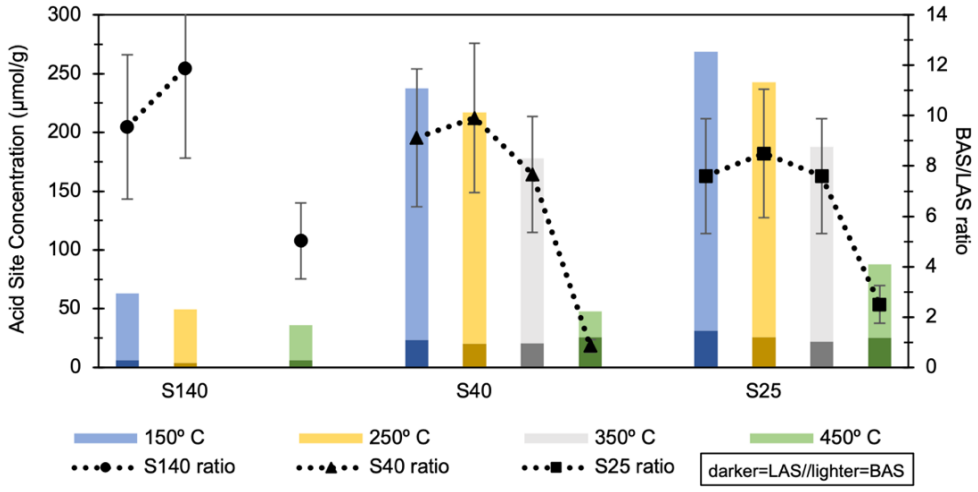

Figure 39 – TAS concentrations (bars, with BAS and LAS referred to with lighter and darker colour) and BAS/LAS ratio (points) from py-FTIR experiments, as functions of temperature and H-ZSM-5 Si/Al ratios

Between 150º-350º C, no significant variations can be observed in acid site density nor on BAS/LAS ratio. Interesting results arise at higher temperatures (450º C). BAS density decreases by 62%, 86%, and 47% for S25, S40, and 140 respectively. LAS density remains distinctly unaltered with increasing temperature. This results in the transition of a BAS/LAS ratio from 7.6 (for both zeolites) to 2.5 and 0.8 for S25 and S40, however, achieved the lowest value for S40. Since S140 appears to conserve most of its acidity, it is possible to say that with increasing Si/Al holds overall stronger acid sites. This result is followed by S25, which shares the presence of structural defects.

The works of Hartanto et al. (2016) and Gabrienko et al. (2010) concluded that increased BAS and LAS can be mainly attributed to the increasing presence of internal silanol groups and silica defects, respectively **[165, 171]**. Silanol groups are found to greatly improve the hydrophilic properties

of zeolites and be extremely influential on catalytic reactions when presented as hydrogen-bonded within the internal pore surface **[174]**.

4.5 *Overview*

The characterization results from ICP-OES and XRD were as expected for these materials. Nitrogen physisorption further elucidated that the calcination process preserved the catalyst's framework whilst also promoting microporosity in the case of S140. The three catalysts displayed similar pore volume and average pore diameter. However, S140 verified a lower percentage of micropore volume, whilst holding a higher micropore area.

From the IR spectra, it was observed that S25 and S140 presented high amounts of silica defects and the presence of Al_{EF} species. Several works on H-ZSM-5 framework properties have found Al_{EF} non-detectable amounts of extra-framework species for Si/Al ratios above 75 through NMR studies **[175-177].** Interestingly, zeolites with Si/Al ratios lower than 40 presented increasing amounts of not only Al_{EF} species but also higher amounts defective sites (inner silanols, interacting OH groups, perturbed framework Al atoms and Al-Lewis sites) **[175, 178]**.

S25 presented the highest TAS density, closely followed by S40. However, S40 displayed the lowest BAS/LAS ratio which was heavily accentuated by the increase in temperature. The high silica catalyst S140 evidenced a decrease in 77% of this number whilst demonstrating a higher percentage of strong BAS. FTIR studies using as probe molecule a poly-substituted pyridine would enlighten the accessibility of these acid sites.

From all the characterized properties, it appears that BAS/LAS ratios and TAS density will be the most determining variables in catalytic activity, catalyst lifetime, and product distribution throughout the catalytic studies.

5 *Catalytic Studies*

5.1 *Deactivation Assessment*

The effect of deactivation and transport phenomena hinders the interpretation of product distribution for the understanding of MTO's reaction mechanism and effect of operating conditions. For a conclusive analysis of the experimental results, not only the catalytic studies are required to be performed under an intrinsic kinetics regime, but the data also compels an investigation of the state of deactivation of the catalyst. One common approach involves stability studies, where for different conditions (temperature, space-time) it is investigated how much time on stream (TOS) the catalyst retains its unchanged activity.

In the present experimental work, deactivation created numerous setbacks during catalytic studies of S25 and S40. As investigated in previous sections strong BAS have been identified as the primary centres for coke deposition **[122, 123]**. With S25 and S40 presenting the highest TAS and BAS density, this result was already expected. Furthermore, it had been found that the deterioration specific BET and micropore surface area was linked to pore obstruction by coke, which is accurate for the observations of S25's lifetime **[60, 109]**.

As previously explored, the severity of deactivation can be associated with known trends, such as higher acid density (and nature of acid sites) and lower mesoporosity. Deactivation evaluation in this work followed a different methodology. This process was aimed at maximizing the amount of information possible to extract from the catalytic experiments. It assesses all data firstly by analysing the individual information at the time of acquisition, followed by the contextualization within the data-set where it is inserted, and then linking all data together within the same catalyst and all catalysts. Hence, it can be divided into three interconnected stages of data assessment and data re-assessment: deactivation profile, catalytic activity, and selectivity analysis.

5.1.1 *Methodology*

Conversion Profile

The data points acquired are required to be obtained under steady-state conditions, which can be identified through steady conversion (within a ~5% experimental error) and selectivities. The effect of deactivation is demonstrated by the impossibility of reaching steady conversion and selectivity conditions over time. Instead, a decrease in conversion is observed in every successive composition analysis (higher TOS) which becomes increasingly evident as the degree of deactivation advances. Furthermore, increasing acid density (lower Si/Al ratios) shortened the necessary period to achieve steady-state.

In **figure 40** are depicted a representation of data points where it was identified the effect of deactivation during the consecutive analyses for each set of conditions by the TOS profile. The behaviour of the orange data set (acquired with the S140) illustrates the typical profile expected in the absence of deactivation.

Furthermore, in the case of S25, the non-deactivated period ranges from 3-4h TOS at 375º C, whereas at the same temperature, S140 demonstrated stability over 20h (TOS). This effect was intensified at higher temperatures, with special prominence for S25. The stability window for this catalyst severely complicated the catalytic studies as only one set of conditions could be studied per catalyst loading.

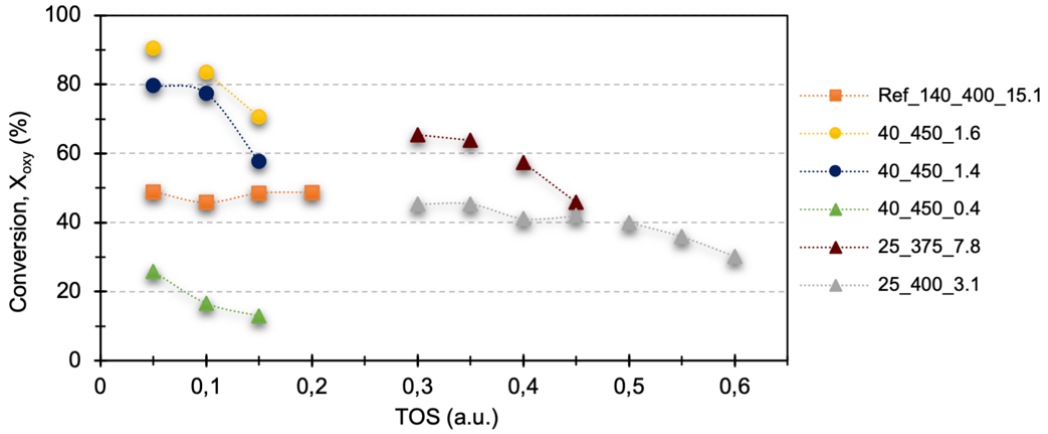

Figure 40 – Oxygenate conversion (X_{oxy}) over H-ZSM-5 Si/Al of 25, 40, 140, as functions of TOS (a.u.) from consecutive analysis of each experimental set at different temperatures and space-times. Legend interpretation: "Si/Al ratio"_"Temperature (° C)"_"space-time ($kg_{cat}.s/mol_{MeOH}$).

The scarcity of data points for S25 and S40 acquired at certain temperatures or acquired without the effect of deactivation, lead the analysis of the conversion profile to be revaluated. The works of Losch et al. (2017) and Palčić et al. (2018) studies indicated approximately 30h and 8h of lifetime for Si/Al of 25 and 12.5, respectively (100% conversion, 450º C, $1h^{-1}$ WHSV) **[179, 180]**. Noting that, at higher temperatures and lower WHSV catalyst lifetime is shortened, Pessanha in his studies found that steady-state conditions could only be only maintained for 2h for S40 (70% conversion, 450º C, $87h^{-1}$ WHSV) **[131]**. This comparison alone demonstrates how studies performed near 100% conversion make reliable data is difficult to extract and stress the necessity to address deactivation under intrinsic kinetic regimes. In these conditions, Pessanha found approximately 8h of lifetime for S40 at 400º C (80% conversion) whereas this work found 4-5h of lifetime for S25 (40-50% conversion). This result is as expected since S25 presents a higher TAS (and BAS) density.

The data set cases presented in **figure 40** were not completely disregarded. Only the first analysis point was considered as the closest value to a non-deactivated reference. This premise can either result in the closest estimation for non-deactivation behaviour or can be an incorrect approximation.

The latter case might be caused by an already too high of a deactivation degree or, in addition to this, the first point was taken before the steady-state was reached; thus, presenting a higher conversion. Nonetheless, this re-assessment allows the assessment of more sizable data sets that may or may not include these points in later considerations so, the first point from each deactivated data set was considered in this assessment stage. This approach was necessary and followed in order to proceed with the analysis of catalytic studies, whilst acknowledging the stage of deactivation of points in every subsequent analysis,

Activity

An important assessment in the analysis of the kinetic parameters of these catalysts is the determination of the catalytic activity at different temperatures. This analysis was essential since, as it will be explored further ahead, S140 exhibited an unpredicted behaviour regarding conversion evolution with space-time, but no deactivation was observed throughout experiments.

Conversely, **figure 41** follows the presentation of a representative data set (experimental points acquired at 400º C for S25 at different space-times) that indicate the presence of deactivation after validation from the previous examination stage.

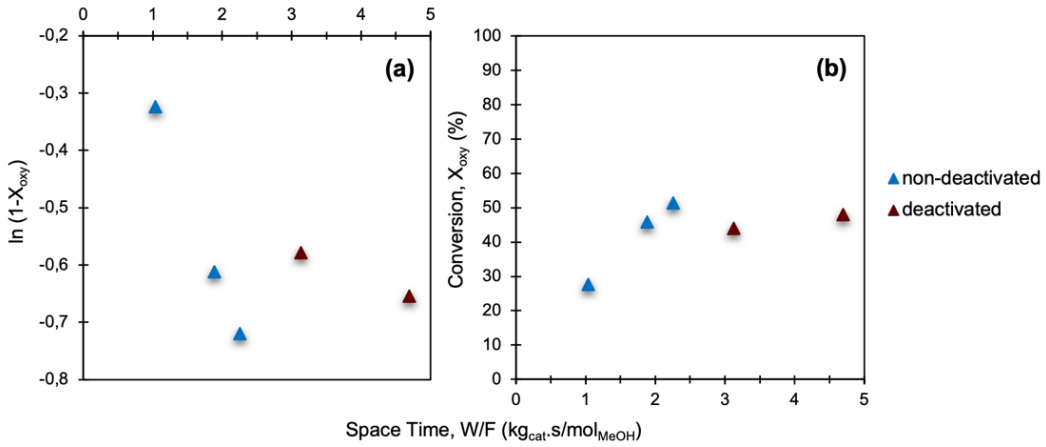

Figure 41 – Plots of (a) ln(1-Xoxy) and (b) conversion of oxygenates (X_{oxy}) over H-ZSM-5 Si/Al of 25 as functions of space-time (T=400º C, P_{MeOH}=0.4 bar, W/F=[1, 5] $kg_{cat}.s/mol_{MeOH}$).

Data points acquired under steady-state in the presence of less severe deactivation (red), once plotted (**figure 41-(a)**), evidence lower logarithmic oxygenate conversion values for that space-time. An evident deviation from the complete data set is marked when determining the catalytic activity of the catalyst at a given temperature. Calculation of activity coefficients is relevant as the single analysis of conversion profiles does not always evidence deactivation when small conversion ranges are studied (e.g., point acquired at the highest space-time in **figure 41-(b)**).

Several of S40's results analysis by Pessanha (2019) did not take into account the steady-state and deactivation evaluation. In addition, the experimental sets were acquired by different

colleagues with different catalyst batches. Catalyst preparation procedures were transversal in all experimentations. Still, visible differences can be observed from the catalytic activity displayed by each data set, **figure 42**. The catalyst batch prepared by Lissens (2021) presents higher catalytic activity than Lei's (2020) and Pessanha's (2019).

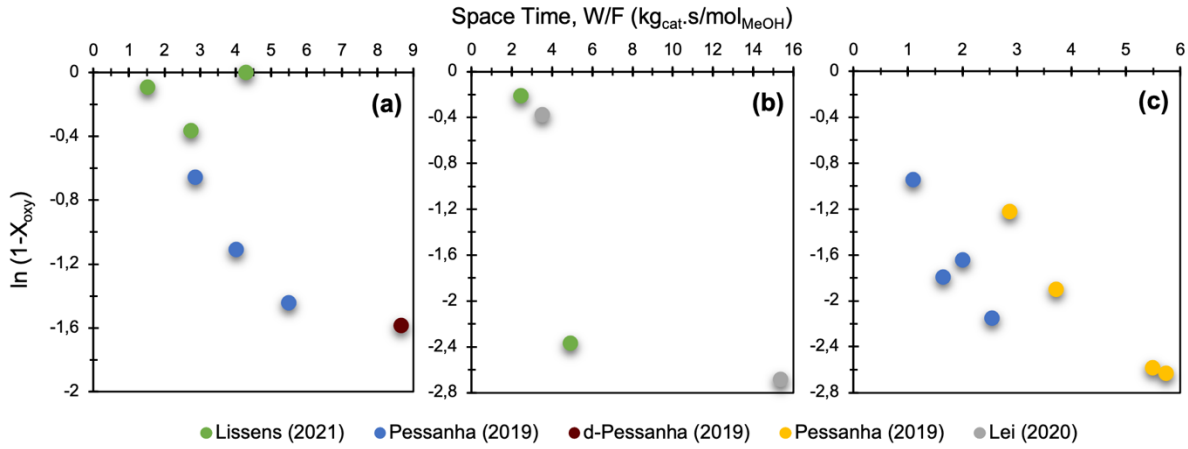

Figure 42 – Catalytic activity plots, with ln(1-X_{oxy}) as function of space time, for H-ZSM-5 Si/Al of 40 from different data sets at (a) 350º C, (b) 375º C and (c) 400º C, at P_{MeOH}=0.4 bar, W/F=[0.5, 16] kg$_{cat}$.s/mol$_{MeOH}$.

The differences in catalytic activity in each catalyst batch present an additional challenge regarding activation energy studies. In the case of the data at 400º C (**figure 42-(c)**), despite being prepared by the same user, the activity from the two data sets (blue and yellow) suggests the possibility of experiments with different batches or experimental error in catalyst loading measurements. Selectivity provides clarity in these matters and so, it ought to be used in parallel. Next, the present example will be further explored. Concerning deactivation alone, it is possible to unmistakably distinguish deactivated points in Pessanha's data set (represented in dark red).

Catalytic activity differences may be attributed to user experimental error (such as poor distribution of samples inside the calcination oven resulting in incomplete calcination) or inadequate sample conditioning after calcination (since all catalysts were attained from the same source). From literature, it had already been determined that both calcination conditions (or crystallization temperature from hydrothermal synthesis) and zeolite modifications affect zeolite's properties, including acid site distribution, mesoporosity and crystallite size **[179, 181]**.

Selectivity

So far, an approach of eliminating steps has been described as a method to access the viability of data with respect to deactivation. Less severe deactivation is distinguishably manifested on activity plots.

It was found that not all cases ought to be discarded when referring to selectivity. Some of these points, with what can be perceived as a smaller degree of deactivation, still retain the expected product distribution. This is required to be a thought-out interpretation as to not undermine hidden information with biased data selection from preliminary hypothesis.

In other cases, due to different catalyst preparation, one set might exhibit higher catalytic activity whilst presenting comparable product distribution. One example is the data acquired by Pessanha (2019) at 400º C. **Figure 43** depicts the activity plots and the selectivities towards C_2, C_3 and aromatics.

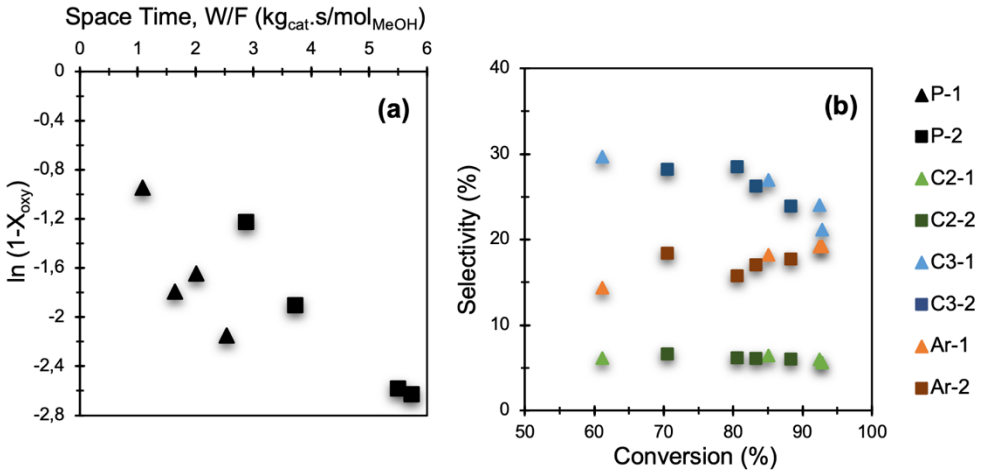

Figure 43 – (a) Catalytic activity plot (with ln(1-X_{oxy}) as function of space time) and (b) selectivity plot as function of conversion (▲: set 1, ■: set 2, colours: different data points) for H-ZSM-5 Si/Al of 40 at 400º C (P_{MeOH}=0.4 bar, W/F=[1, 6] $kg_{cat}.s/mol_{MeOH}$).

In this example, it is clear how deactivation is not the factor that causes the deviations in selectivity. Data set 1 observes a clear a higher catalytic activity than set 2 while preserving the product distribution. Overall, this analysis elucidates the difficulty to assess which points suffered deactivation from those which present different catalytic properties (or experimental errors).

The authors Sun (2013), Pessanha (2019), Ilias et al. (2013), as well as the observations from the present experimental work, indicate that the hydrocarbon products' selectivity does not change within 20-80% of steady-state conversion **[110, 112, 131]**. This analysis is of special relevance in the cases of small data sets or data sets where it was not possible to acquire data in the absence of deactivation. The data acquired at 375º C for S25 contains a pertinent example.

Despite not fulfilling the activity criteria points (**figure 44-(a)**), the product distribution of the remarked deactivated points (triangles) follows a known trend of polynomial behaviour. In addition to hydrogen transfer reactions, higher olefin methylation (most greatly propylene methylation) is observed at conversions above 80% - evidenced by the decreasing presence of propylene and rising aromatic selectivity (**figure 44-(b)**).

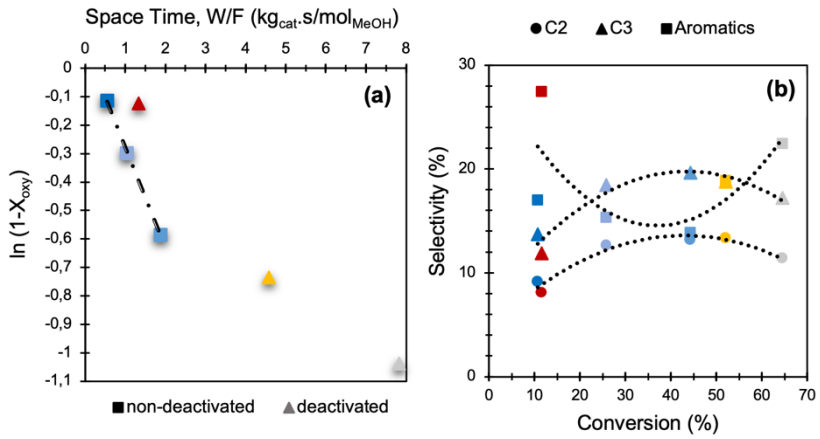

Figure 44 – (a) Catalytic activity plot with ln(1-X_{oxy}) as function of space time and (b) selectivity plot as function of conversion (most generally observed trends within 20-80% oxygenate conversion), for H-ZSM-5 Si/Al of 25 at 375º C (P_{MeOH}=0.4 bar, W/F=[0.5, 8.0] $kg_{cat}.s/mol_{MeOH}$).

At conversions under 20%, the MTO reaction is expected to proceed with a high abundance of aromatics, denoting the induction period, with the expected slow formation of the hydrocarbon poll) These aromatic species react very slowly with the feed (evidencing the propagation of the aromatic cycle) with little data reproducibility. Consequently, data under 20% oxygenate conversion holds relevant information for selectivity analysis in the scope of the conversion effect.

The two other remaining points at higher space-times, initially disregarded as deactivated, also present relevant cases as they hold viable information for selectivity analysis by accurately fitting the plots. Through this analysis, more information can be extracted from the experiments by the comprehension of a larger window of space-times under study. In cases where, at iso-conversion, the data points at highest space-time that evidences higher selectivity towards aromatics (and most of the time ethylene) is considered a completely unreliable point for further studies.

5.1.2 *Summary*

Considerations about data deactivation required a profound study for each case. It was verified that catalytic activity displays a severe dependency on catalyst preparation; thus, deactivation analysis referred to the same batch set for each catalyst.

A thorough process was established in order to access the stage of deactivation of the acquired data, starting with the analysis of the TOS profile, followed by the activity and selectivity analysis. Due to the heterogeneity of the available data, each set was carefully analysed by its individual properties and its significance on the whole.

The study of S25 presented great obstacles with the almost immediate deactivation in the range of experimental temperatures tested. The small degree of deactivation already observed at 350º C was taken into consideration in the subsequent analysis. The data set obtained for S40 at

375º C was considered unreliable for catalytic activity studies due to the scarcity of data points. S140 presented the most reliable data, with over 20h TOS of catalyst lifetime.

Furthermore, the analysis of product distribution evidenced that different catalytic activity does not interfere with selectivity, as it is a consequence of catalyst preparation. It was investigated that data sets presenting a small degree of deactivation still hold reliable selectivity information.

The high activity of the catalyst S25 in parallel with setup limitations (catalyst loading and both liquid and gas feeding flowrates) made data acquisition under intrinsic kinetic regime for S25 a great challenge. At the lowest temperatures (350º C and 375º C), S25 evidenced deactivation after 2-3 conditions tested, an effect that was accentuated with increasing temperature.

Worth noting that, all points considered for catalytic activity analysis of S40 at 450º C derive from the revaluation of deactivated data (consideration of the first analysis point). Furthermore, Pessanha (2019) refers in his work that the activity of this data set is underestimated due to the fast deactivation. Because so, this temperature should not be considered for the calculation of the apparent activation energy. Furthermore, the set S40 at 375º C was found to not be reliable for the following analysis of kinetic parameters (activity and apparent activation energy) due to severe lack of reliable data and small data set per catalyst batch.

5.2 *Catalytic Activity*

Catalyst activity is an essential parameter of investigation in kinetic studies, namely, the apparent reaction rate and activation energy. The following picture (**figure 45**) depicts the data acquired under state-state conditions selected and used for catalytic activity analysis.

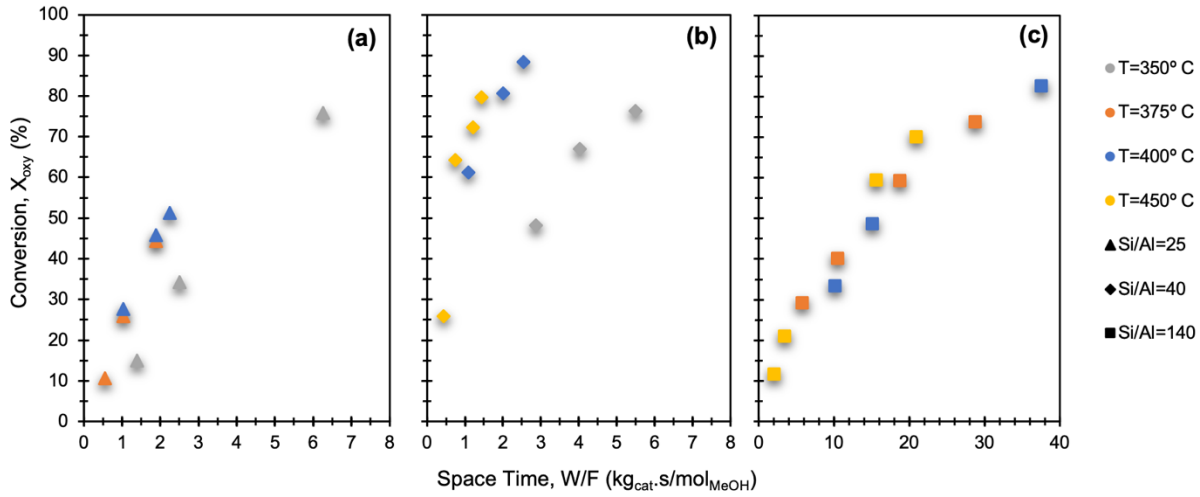

Figure 45 – Oxygenate conversion of MTO as function of space-time of H-ZSM-5 Si/Al of (a) 25, (b) 40, and (c) 140, at different temperatures. Conditions: T=[350, 450]º C, P_{MeOH}=0.4 bar, W/F=[0.5, 40.0] kg_{cat}.s/mol_{MeOH}.

In optimal conditions, catalytic activity is evaluated concerning each catalyst batch and at oxygenate conversions between 20 and 80%. However, data outside these limits were considered as per **figure 45**. A thoughtful analysis determined that the disregard of some of the points outside these limits resulted in regressions with only 2 points. This was the case of S25 (350º C and 375º C) and S40 (400º C). Nonetheless, data accurately fitted the linear regressions of the logarithmic plots of conversion (**figure 46**).

Catalytic activity is expected to increase with decreasing Si/Al ratios. The analysis **figure 46-(a)** leads to the conclusion that the obtained data evidences a certain degree of deactivation in comparison with S40 (**figure 46-(b)**). It is depicted, at comparable space-times (2.3 and 2.0 $kg_{cat}.s/mol_{MeOH}$, respectively) at 400º C, an unmistakable difference in conversion from 51% to 81% (for S25 and S40). Both data obtained at 350º C and 375º C display similar deactivation.

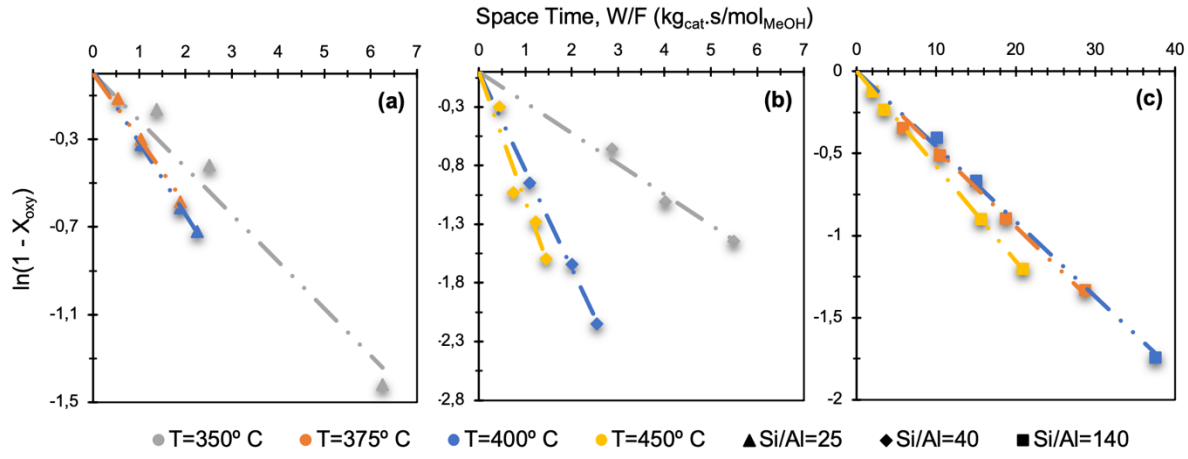

Figure 46 – MTO catalytic activity plot with ln(1-X_{oxy}) as function of space time of H-ZSM-5 Si/Al of (a) 25, (b) 40, and (c) 140, at different temperatures. Conditions: T=[350, 450]º C, P_{MeOH}=0.4 bar, W/F=[0.5, 40] $kg_{cat}.s/mol_{MeOH}$.

Catalysts exhibit an evident increase in activity with increasing temperature since data at iso-conversion observes decreasing space-times. However, a modest degree of overlapping of data is observed at 375º C and at 400º C. Selectivity studies will bring insight into the possibility of a reaction regime transition since reliable kinetic parameters cannot be extracted from S40 at 375º C nor S25.

In the case of S140 (**figure 45-(c)**), a distinctive behaviour is observed, where the induction and exponential period do not follow as expected. No perceptible catalytic activity variation occurs within the studied temperature interval from 375-450º C. In **figure 45-(b)**, it is possible to straightforwardly observe the difference in activity between S40 and S140. At 450º C and similar space-times (1.4 and 2.1 $kg_{cat}.s/mol_{MeOH}$, respectively), the more acidic catalyst presents a steady-state conversion of 80% compared to 12%.

Experimental kinetic parameter studies are scarce in the literature and a transversal method is yet to be established. This makes data comparison a challenge in MTO as many studies also do not disclose important operating conditions.

Table 6 presents the calculated parameters according to the previous formulations. Altogether, the linear regressions and Arrhenius plots accurately fit the data. Kinetic parameter determination is detailed in **Annex C**.

Table 6 – Kinetic parameters calculated for H-ZSM-5 Si/Al of 25, 40, and 140 (T=[350, 450]º C, P_{MeOH}=0.4 bar).

Si/Al	Temperature (º C)	Activity, $k_{app} \cdot P^0_{MeOH}$ (mol/kg$_{cat}$.s)	$E_{A,app}$ (kj/mol)
25	350	0.214 ± 0.020	**45** [a]
	375	0.299 ± 0.018	
	400	0.321 ± 0.003	
40	350	0.26 ± 0.010	**85** [b]
	400	0.886 ± 0.057	
	450	1.105 ± 0.081	
140	375	0.0473 ± 0.001	**10** [c] **19** [d]
	400	0.0458 ± 0.001	
	450	0.0578 ± 0.001	

[a] Considering the data acquired at 350º C and 375º C. [b] Considering the data acquired at 350º C and 400º C.
[c] Considering the data acquired at 375º C and 450º C. [d] Considering the data acquired at 400º C and 450º C.

The similar catalytic activities for S25 to S40 are coherent with the expected deactivation of S25. From the deactivation analysis in the previous section, the catalytic activity of S25 should be considered unreliable. However, it is plausible that activation energy did not suffer a great deviation if a similar degree of deactivation was present in all data sets (i.e., a similar shift in space-time). Since deactivation is unmistakable present in this data set, with no other reference values the validation of intrinsic kinetics cannot be guaranteed. Due to the more severe deactivation effect at higher temperatures, the activation energy was calculated for the two lowest temperatures.

For S140, with similar catalytic activities for 375º and 400º C, the apparent activation energy was calculated for assuming the combination of data of each of these temperatures with data acquired at 450º C. Due to the low standard deviation and particular behaviour of the data, it is uncertain which value is correct. For future reference, a mean of these values will be used. The results regarding S140 stand out as not only was not observed an autocatalytic effect, but both catalytic activity and activation energy are a decimal place and over 4 times, respectively, lower than its predecessor. A change in the control dual-cycle mechanism control due to the catalyst's acidity and topology might be behind this unprecedented behaviour.

Derived from the inquired in zeolite characterization, to understand S140 behaviour, acid site density and mesoporosity were studied. For this analysis, Sun's (2013) reported activation energy of 93 kJ/mol was also used **[110]**.

The relationship between the logarithm of the apparent activation energy and the proportion between BAS/LAS is notable (**figure 47**). The ratio between the mesoporous and microporous volume shares the same behaviour. A strong hypothesis is that there is a dependence between the

activation energy (thus, the catalytic behaviour as well) and one of the other variables under study. Furthermore, this dependence might be expressed by a polynomial function with a maximum activation energy between S40 and S140.

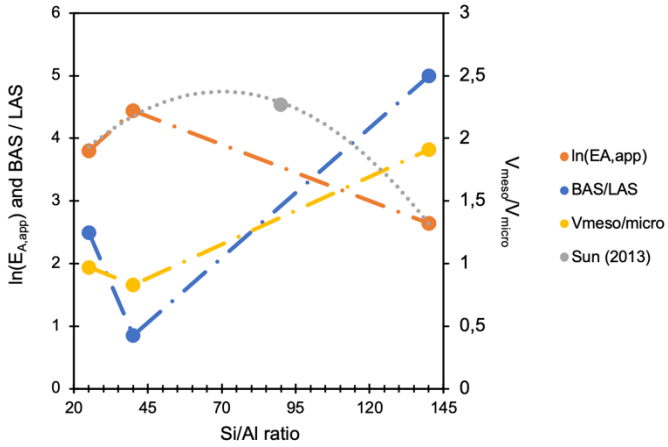

Figure 47 – Plot of ln($E_{A,app}$) of Si/Al of 25, 40, 140 obtained experimentally and of Si/Al 90 from Sun (2013) [110]; plot of the ratio of mesoporous and microporous volume and plot of the ratio of BAS/LAS (py-FTIR at 450º C), as a functions of catalyst Si/Al ratio.

As also explored before, a great change in acid site density and acid site density distribution occurs between 350 and 450º C. This could be primarily hypothesized as the reason behind the shared catalytic overlapping data 375 and 400º C that suggests a regime transition. The acquisition of reliable intrinsic kinetic data at these temperatures for these catalysts is essential to enlighten the occurring phenomena.

Furthermore, investigation of more catalysts with Si/Al ratios between 40 and 140 is also indispensable to determine the critical aluminium value for this regime change. Selectivity analysis will unmistakably shed light on the reaction path that follows these interpretations. In **Annex C** is presented a brief review of some different reaction activation energies calculated by different authors

Summary

Catalytic studies for H-ZSM-5 with different Si/Al ratios were conducted at 0.4 bar methanol partial pressure. Data were acquired under steady-state and intrinsic kinetics regimes in order to determine kinetic parameters. Furthermore, data was studied within the regime where the dual-cycle mechanism is the best descriptor, and the first-order kinetic approximation is valid.

Due to the certain degree of deactivation, S25 presented lower catalytic activity than S40. Nonetheless, activity appeared to decrease with increasing Si/Al ratio and increase with temperature. Apparent activation energies of 45, 85, and 14 (average) kJ/mol were calculated for S25, S40, and

S140. This result was described as a polynomial behaviour, with the inflexion point between Si/Al of 40 and 140, also observed for BAS/LAS and mesoporous/micropores volumes.

5.3 *Product Distribution*

In the present subdivision, the product distribution of MTO reaction over the different acidity H-ZSM-5 catalysts will be studied at different temperatures, throughout a various space-times.

To begin with, the analysis of the effect of space-time will take place, which will then be used as a conduit for the study of the effect temperature and catalyst acidity at iso-conversion. Selectivity will be evaluated according to the number of carbons in the product structure. C_2 and C_3 products might be referred to as ethylene and propylene since these olefins account for about 90% of the yield.

In **Annex D** there can be found supplementary information on this chapter, including the description of the main reactions in the MTO and all selectivity plots. Necessary to note that, S25 data set has been referred to multiple times as deactivated, with unreliable data (most significantly at 400º C).

5.3.1 *Effect of Conversion*

Understanding all the phenomena at different conversions is essential, not only in terms of mechanistic at a given set of conditions but also for data selection and data comparison. Before, data with mild deactivation displayed the retention of an accurate description of product distribution.

When data were acquired at low conversions, typically lower than 20%, evidence of the induction period of the MTO reaction. This period is distinguished by very high selectivities towards aromatics - the initial poly-MB from the hydrocarbon pool, from which the first light olefins are to be formed through cracking reaction. Additionally, data previously considered deactivated for catalytic activity studies was reviewed according to the principles already explored.

Iso-temperature data set comparison was available at 375º C and 400º C. Due to the high influence of deactivation of S25 at 400º C, for the iso-temperature study that follows in **figure 48**, data was compared at 375º C. In the case of S40, due to the scarcity of data available, 2 distinct data sets (totalizing 3 points) were used. From **figure 48**, not only there can be found an increase in conversion with space-time, but it also affects product selectivity with noticeable second-order polynomial trend.

The following figure may be interpreted as representative of the selectivity trends observed for each catalyst. Supportive information (through the entire range of temperatures studied for each catalyst) can be consulted in **Annex D2**.

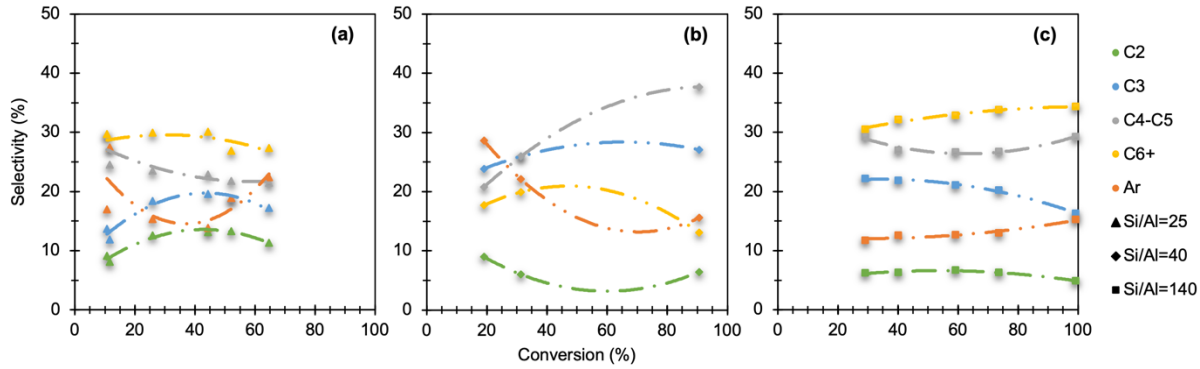

Figure 48 – Selectivity plot as function of oxygenate conversion on MTO at 375º C, P_{MeOH}=0.4 bar, for H-ZSM-5 Si/Al of (a) 25, (b) 40, and (c) 140.

It is indisputably evident how selectivities in S140 remain almost unaltered throughout the entire range of conversion whilst maintaining clear polynomial trends (those also shared by the other two catalysts). Interestingly, this catalyst described a similar behaviour for the remaining temperatures, 400º and 450º C, with selectivity variations of about 5% (absolute value between the maximum and minimum selectivities achieved, represented in **figure 48**). This pattern had already been observed by Sun (2013) for H-ZSM-5 Si/Al of 90 as well **[110]**.

In the range of C_2, C_3, C_{4-5}, and C_{6+} products, a convex curve (negative second-order term) best describes the trend of the effect of conversion. Aromatic hydrocarbon selectivity is best represented by a concave curve and, in most cases, are the most affected by conversion. Naturally, this analysis is reserved for the conversion window from approximately 20-80% where the dual-cycle mechanism (referring to the aromatic and alkene cycles) is a valid descriptor as the aromatic hydrocarbon pool is already fully developed outside the induction period. Higher oxygenate conversions are not aimed due to the difficulty of studying MTO reaction without the effect of deactivation and without reaching near full conversion, where secondary reactions predominate.

Of course, with only one data point for S40 at 375º C, mechanistic information for the effect of conversion relied upon the observation of the remaining temperatures and comparison between catalysts. Not only do the considered data points correspond to different catalyst batches and were acquired by different colleagues, but only one point is truly fitted in the conversion range under study.

Figure 49 refers to the variation of selectivities (difference between maximum and lowest values reached) within the 20-80% oxygenate conversion. Data observes a general trend with an increase in selectivity of C_{6+} and aromatic hydrocarbons with increasing conversion. A negative effect in C_2, C_3, and C_{4-5} selectivities was documented, the latter suffering a higher decline.

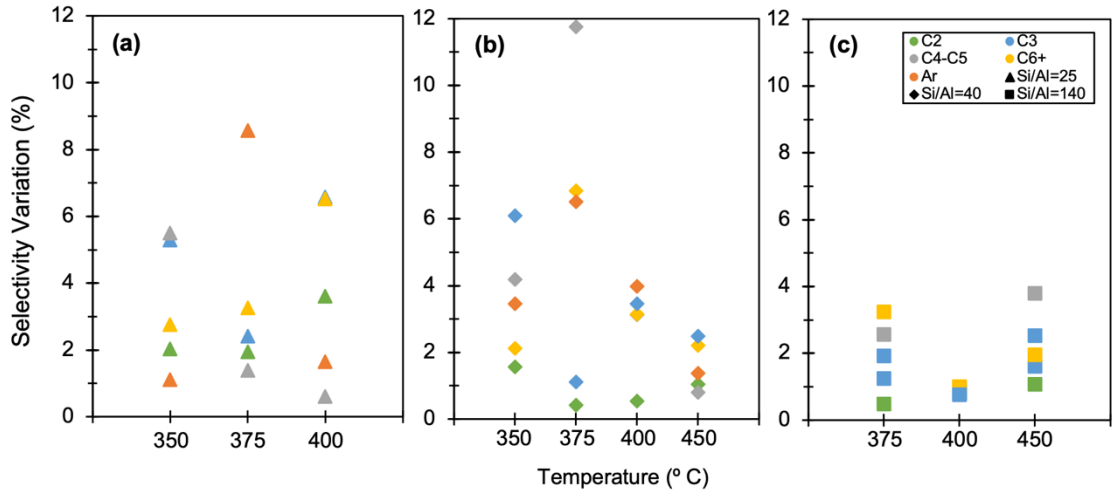

Figure 49 – Variation (difference between highest and lowest value) of selectivity plot as a function of reaction temperature for H-ZSM-5 Si/Al of (a) 25, (b) 40, and (c) 140 (20-80% oxygenate conversion, P_{MeOH}=0.4 bar).

From the analysis of **figures 48 and 49**, aromatics, C_{6+} and C_{4-5} selectivity suffer the most effect of conversion. Selectivity presented the greatest variations with conversion in higher acidity catalysts. However, when referring to the data acquired in optimal conditions (same user, in the absence of deactivation), selectivity did not change beyond 5%. Therefore, an averaged value (within the 20-80% conversion range) can be used in following studies in order to describe selectivity at a each temperature, whilst noting the inflexion point and extreme points of the polynomial functions that describe this tendency. Furthermore, the analysis of **figure 49** also suggests an increasing effect of conversion at lower temperatures.

These observations imply that with increasing conversions, conversion improves by the formation of olefins. The production of olefins reaches a maximum while aromatic selectivity achieves a minimum. Accordingly, the aromatic dealkylation and alkene methylation reactions propagate faster than cracking and aromatic methylation reactions, which is verified by the increases in C_{2-3} olefins and C_{6+} species and the decrease in C_{4-5} and aromatic selectivity, respectively. These reactions appear to be increasingly dominant until a change marked by an inflexion point in the products' selectivity is observed as conversion approaches 70-80%. This inflexion point appears to be shifted to lower conversion with increasing catalyst acidity.

At this stage, the trend is interrupted and the decreasing in selectivity towards C_2-C_3 olefins takes places. This change evidence the rising of alkene methylation, cyclization, and hydrogen transfer reactions. Naturally, the decrease in the selectivity of light olefins through these reactions is directly responsible for the observation of an increase in selectivity towards higher olefins, aromatics, and alkanes.

All the previous statements agree with M. Zhang's et al. (2016) conclusions **[113]**. Furthermore, the product distribution obtained for S25 at 350º C (at approximately iso-conversion of 60%) closely resembles the results obtained by the same study for a Si/Al of 15 catalyst (**figure 21-**

(a)). These effects appear to be amplified by increasing catalyst acidity and at lower temperatures. Moreover, this inflexion point appears to be shifted for higher conversion with increasing Si/Al ratio.

To further explore the effect of conversion on the contribution of the aromatic/alkene cycle, **figure 50** continues the previous conditions with the description of the ratios of ethylene to isobutane (E/Isob) and alkane to alkene (A/A) ratios with conversion at 375º C.

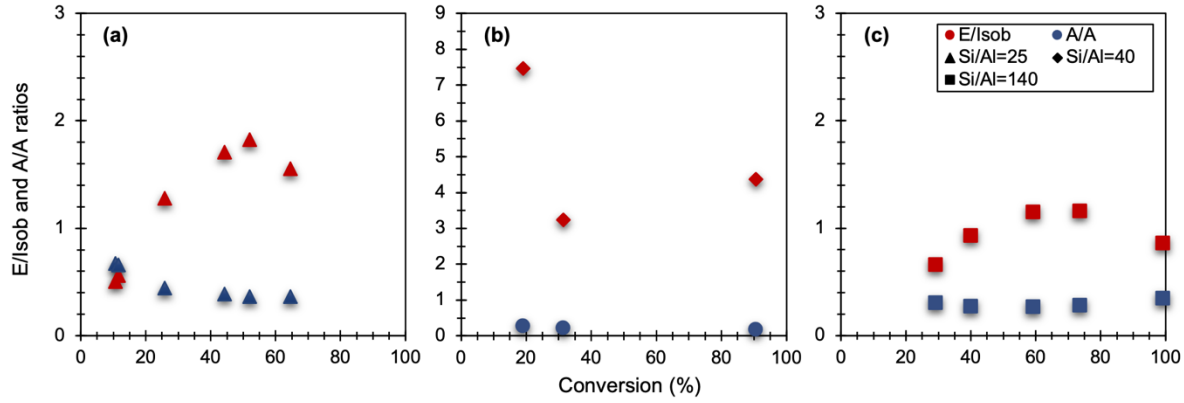

Figure 50 – Ratio of E/Isob and A/A as functions of oxygenate conversion on MTO at 375º C for H-ZSM-5 Si/Al of (a) 25, (b) 40, and (c) 140 (20-80% oxygenate conversion, P_{MeOH}=0.4 bar).

Ethylene to isobutane and alkane to alkene ratios are direct descriptors of the contribution of the aromatic/alkene cycle and the extent of hydrogen transfer reactions (responsible for the formation of alkanes), respectively. In these plots, both functions exhibit the same polynomial behaviour displayed by selectivity. Furthermore, a closer examination establishes that selectivity, E/Isob, and A/A share inflexion points at comparable conversions. The same parameters verify an accentuated effect of conversion with increasing temperature.

In this analysis, S140 (**figure 50-(c)**) is considered the best reference due to not only the higher amount of data, obtained in the absence of a deactivation effect unlike S25 but data acquired for S40 did not have an adequate GC column to differentiate isobutane from methanol. The displayed values were achieved by correlation with the amount of n-butane by Marie-Elisabeth Lissens.

S140 (at 40% conversion) presents E/Isob and A/A ratios of 0.93 and 0.27, respectively. At around 74% conversion, as the aromatic cycle is favoured, these ratios develop to the values 1.16 and 0.28. The regime change (aromatic/alkene cycle dominance) with conversion dependence is confirmed to be greater at higher temperatures by the variations of 0.50, 0.35, and 1.88 in E/Isob ratios at 375º, 400º and 450º C, respectively, within the 20-80% conversion range.

Although S140 has not demonstrated a characteristic autocatalytic effect, together with considerably lower catalytic activity, the three catalysts exhibit similar tends regarding conversion dependency. E/Isob follows the same trend as olefin selectivity.

The previous formulation (regarding the aromatic dealkylation and alkene methylation reactions being dominant until the inflexion point) is verified with the increasing ratio of the aromatic/alkene cycles; ergo, a rising activity of the aromatic cycle. At conversion increasingly higher than 80%, the alkene cycle becomes more prevalent (alkene methylation, oligomerization and cracking reactions) whilst alkanes selectivity also rises through hydrogen transfer reactions – which was confirmed by the increase in A/A ratio with increasing conversion. These phenomena were also discussed by M. Zhang (2016) by the studies of co-feeding propylene and toluene (**figure 24**) **[112]**.

5.3.2 *Effect of Temperature*

Catalysts with different Si/Al ratios were studied in the range of 350º to 450º C. Studies of temperature effect, or the acidity effect in the next section, are ideally performed at iso-conversion. Due to the difficulties encountered during the experimental period and the available data for S40, this was not possible. To compare product distributions, the averaged oxygenate conversions between 20-80% were used. As explored in the last section, in this range of conversion selectivity does not change exponentially, presenting a second-order polynomial behaviour.

Logically, considering such a vast range of conversions might lead to results difficult to compare. Therefore, the lower and upper bound variations of selectivity (in relation to the average) were included in the analysis of product distribution (**figure 51**). The upper and lower error bar values correspond to the lowest and highest selectivities registered in the considered conversion range (inflexion point and extremes of the second-order polynomial functions).

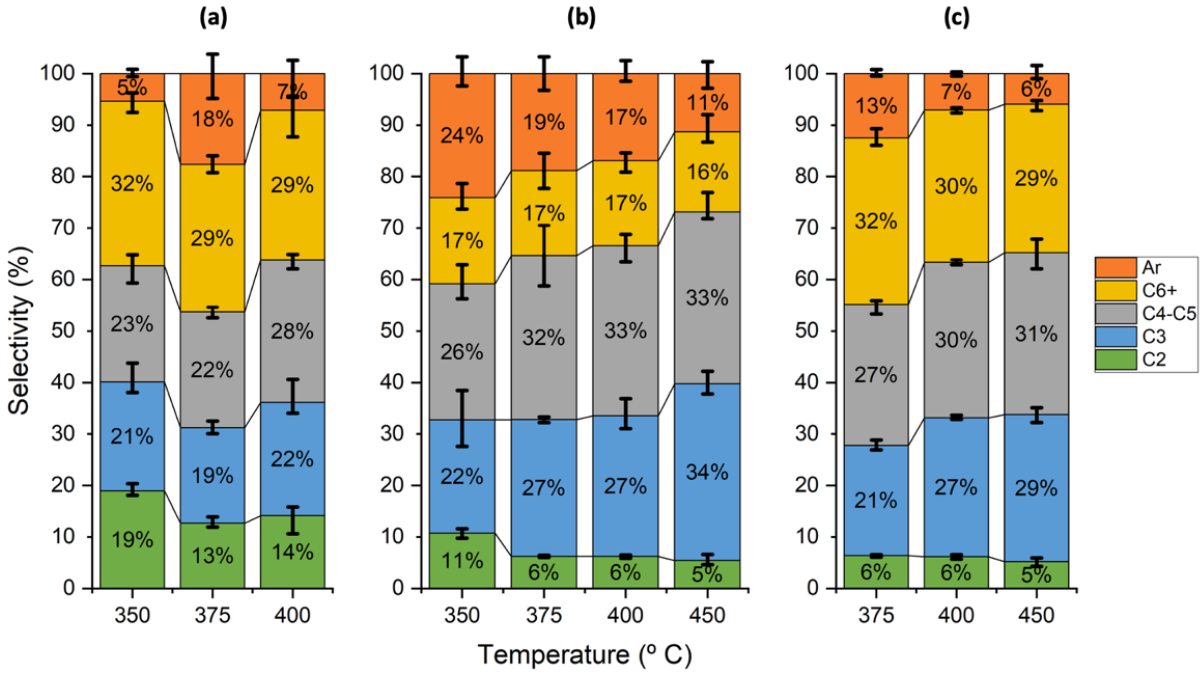

Figure 51 – Averaged product distribution of MTO as function of temperature for H-ZSM-5 of (a) 25, (b) 40, and (c) 140, within the range of oxygenate conversion of 20-80% and P_{MeOH}=0.4 bar.

The distinct trend of S25 can be linked with the effect of deactivation. That effect is clearly increased as aromatic selectivity rises with increasing temperature, together with the increasing high values of the high error bar (which regards the inflexion point of aromatics' selectivity). This higher aromatic content is followed by a decrease in the expected C_3 yield and higher C_{6+} content.

An increase in temperature in **figure 51** clearly depicts a cross trend in product distribution common to catalysts with different acidities. Between 375º C and 450º C, aromatic hydrocarbons display a decrease in selectivity from 13% to 6% for S40 and S140. This translated into a decrease in 42% and 54% of aromatic selectivity within this temperature interval.

For the same catalysts, little to no temperature effect in C_2 and C_{6+} selectivity can be observed. In contrast, C_3 and C_{4-5} products observe an increase in selectivity with increasing temperature. The first registers a rise from 22% to 34% and 21% to 29% for S40 and S140. This translates into an increase of 26% and 38% in selectivity, respectively, whereas C_{4-5} increases at a much lower rate (3% and 15%).

Analogous findings were observed by Sun (2013) **[110]**. Those studies were conducted for Si/Al of 90 (**figure 17**) and revealed an increase in C_{3-5} yield with increasing temperature. The averaged selectivity attained for C_3 was 40% (400º C, P_{MeOH}=0.017 bar). Although the intrinsic kinetic regime is not mentioned throughout these works, the discrepancies in product distribution (i.e., the high propylene yield) are explained by the lower methanol partial pressures (**figure 23**).

Within the range of 400º to 500º C, C_3 yield verified an increase from approximately 20% to 29% (which translates into an increase of 45%). Selectivity towards C_3 attained by Ilias et al. (2013) for Si/Al of 42.5 (P_{MeOH}=0.7 bar) appears to sharply rise with increasing temperature: 88% from 350º C to 450º C to a total of 35% **[112]**. C_{4-7} follow the same trend while ethylene decreases, which agrees with the observations in this work.

From these findings, temperature appears to have a highest impact on aromatics and C_3 selectivity. In **figure 52,** the averaged E/Isob and A/A ratios are represented for the previous conditions.

The rising in E/Isob ratios in the case of S140 (**figure 52-(c)**), together with lower A/A ratio, indicates the prevailing effect of the aromatic cycle with increasing temperature and the restrain in the propagation of hydrogen transfer reactions. Considering the higher range of temperatures studied for S40, and observation of the results of S25, a linear behaviour appears to not be the best descriptor.

A transversal hypothesis for these observations is that the alkene cycle is increasingly more dominant with increasing temperature. The increase in C_{3-5} selectivities and decrease in C_2 (and C_{6+}) hydrocarbons indicate a rising in alkene methylation cracking reactions with increasing temperature. This remark is also supported by Ilias et al. (2013) **[112]**.

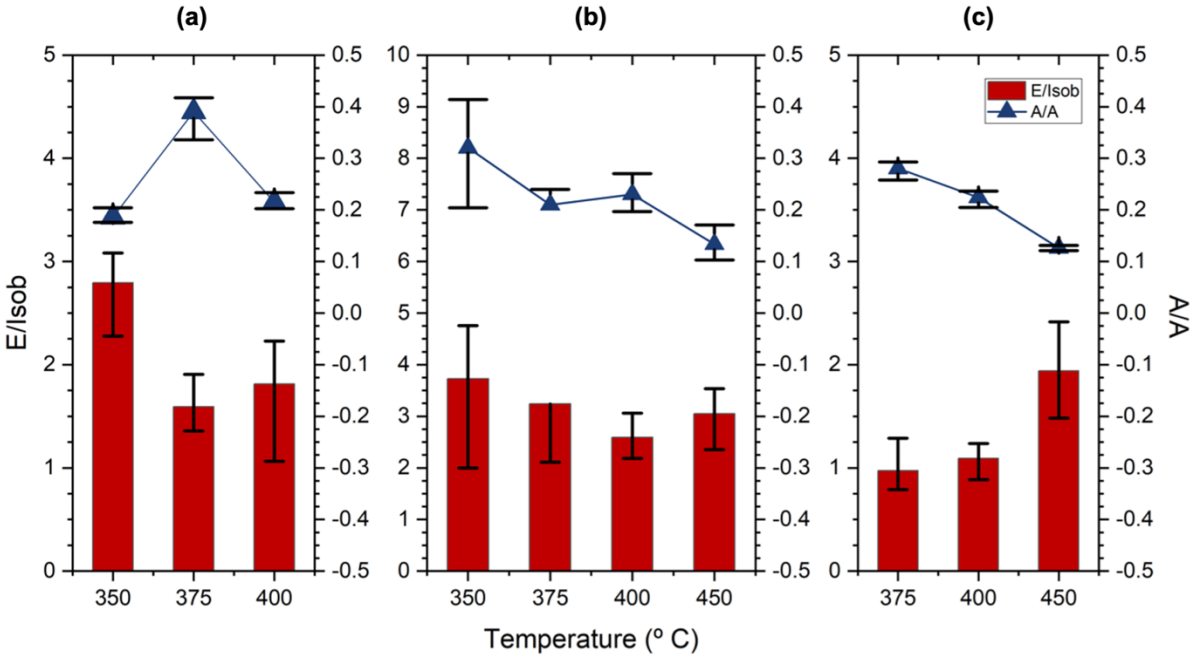

Figure 52 – Ratio of E/Isob and A/A on MTO (as functions of temperature for H-ZSM-5 Si/Al of (a) 25, (b) 40, and (c) 140 (20-80% oxygenate conversion, P_{MeOH}=0.4 bar).

However, it follows that the alkene cycle achieves its maximum of extent between 375º and 400º C, at which point the aromatic cycle begins to be prevalent from thereon. Although data acquired at higher temperatures may not be entirely reliable (i.e., 400º C and 450º C for S40 and S25, respectively), the correlation found with data for S140 is unmistakable.

Thus, it is postulated the increase in temperature (from 350º C to 375º C) is initially responsible for favouring the production of light olefins (except for ethylene) and the decrease of aromatic species in the effluent. The product distribution is an indicative of an increase in lower olefin methylation and cracking reactions at a faster rate than oligomerization and higher olefin methylation reactions. **Figure 52** supports this interpretation with the increase in dominance of the alkene cycle by the decrease of the E/Isob ratio, up until 375-400º C. The decrease in A/A with increasing temperature supports the lower extent of aromatic species being formed. **Figure 51-(a)** observes a contrary trend at 350-375ºC which, supported by great increase in aromatics in the product stream at 375º C which expounds the stage of deactivation of the data.

It had been approached before the behaviour of H-ZSM-5 in the range of temperatures of 375-400º C. Results demonstrated an unusual superposition of catalytic activity. The unpredicted phenomenon was hypothesized to be linked with a regime transition and can now be discussed.

For S40 (**figure 52-(b)**), the product distribution at those temperatures remained unaltered with an accentuated decrease in E/Isob ratio from 3.8 to 2.6 at 375º C and 400º C, respectively. In contrast, S140 data evidence a rise in C_{3-5} selectivities while E/Isob ratio does not change substantially, with E/Isob ratios of 0.97 and 1.09 for the same temperatures. This marks a change in the prevalence of the alkene/aromatic based cycles at these temperatures.

Thereon, an increase in the dominance of the aromatic cycle is evident by the increase in E/Isob ratios. For temperatures higher than 375º C, the product distribution evidences a gradual decrease in aromatics whilst maintaining C_2 olefins. These observations support of the preliminary hypothesis formulated by Pessanha (2019). Although the rate of formation of aromatics appears to decrease by the decrease in A/A ratio, the rate at which aromatic methylation and dealkylation reactions occur might increase substantially with increasing temperature. These reactions being the main precursor for the increase in propylene and ethylene production. This would be translated in the formation of higher poly-aromatic intermediaries at a lower rate, thus, resulting in lower aromatic yielding due to higher diffusion limitations. At the same time, the olefin methylation reactions remain active since C_{4+} hydrocarbons content remains relatively constant.

This observation supports the formation of propylene from both cycles while ethylene appears to be mainly formed from the aromatic cycle, primarily methylated over propylene.

The increase in selectivity of the propylene olefin appears to derive from a compromise between the production from the aromatic and alkene cycles, cracking, and its consumption by alkene methylation reactions to form higher olefins. Moreover, C_3 and C_{4+} selectivities presented an increase in 23% from 350º C to 375º C for S40, where the alkene cycle was favoured in 22%.

From 400º C to 450º C (in S140), selectivity increased 11% and 3% for the same hydrocarbons, whilst the aromatic cycle was favoured in 45%. Thus, it can be said that propylene is formed by the aromatic cycle in a much lesser extent than from the alkene cycle.

5.3.3 *Summary*

Catalytic studies, under steady-state and intrinsic kinetics regimes, for H-ZSM-5 with different Si/Al ratios were conducted at 0.4 bar methanol partial pressure. The product distribution was reevaluated according to the deactivation stage to study the effect of temperature and conversion with respect to the dual-cycle mechanism concept.

A change in the promotion of the aromatic cycle with increasing oxygenate conversion is observed with an inflexion point at approximately 60% where the alkene cycle becomes more prevailing and where propylene reaches its maximum selectivity. This inflexion point appears to be shifted to lower conversion with increasing catalyst acidity and the conversion effect variation greater at higher temperatures. To study selectivity across the different catalysts at different temperatures, data within the range of 20-80% was used as a mean average since it was proven to accurately represent the product distribution.

With a similar behaviour, the effect of temperature is portrayed by an increase in the alkene cycle propagation that changed at 375º C/400º C, from where the aromatic cycle resumed its influence. Furthermore, it was discerned that S40 is most favoured by the aromatic cycle in

comparison to the other two. A more profound analysis of this data suggested that ethylene is primarily methylated to propylene and that the latter olefin is predominantly formed from the alkene cycle.

Propylene yield and propylene/ethylene ratio were maximized at higher temperatures. S40 displayed the best performance achieving 34% selectivity for the reaction temperature of 450º C, with a propylene/ethylene ratio of 5.3.

These findings were in accordance with the expected from other studies.

5.4 *Effect of Acidity*

The study of the effect of acidity resides as the central part of the present work. For that purpose, catalytic studies were performed on H-ZSM-5 zeolites with Si/Al ratios of 25, 40 and 140, as it was covered in previous sections. In addition, the analysis that follows also requires the understanding on deactivation of the catalysts at the different temperatures.

In previous analyses, S140 demonstrated a catalytic activity over ten times lower than S40 and S25, which was accompanied by a much higher stability by the first catalyst. S25 presented similar catalytic activities to S40 at 350º C, although this result is unreliable due to the fast deactivation of the lower Si/Al ratio catalyst. Nevertheless, S40 found a much higher activation energy (85 kJ/mol) when compared to the other two catalysts (45 kJ/mol and 14 kJ/mol for S25 and S140, respectively).

The effect of temperature determined the best propylene yield maximization for S40, achieving 34% selectivity at 450º C (propylene/ethylene ratio of 5.3), with the effect of temperature being most pronounced by S140 and S25. Furthermore, a maximum of contribution of the alkene cycle was observed between 375º and 400º C.

5.4.1 *Iso-conversion comparison*

In the previous section, the effect of conversion was referred to be more evident at lower temperatures and to increase with increasing Si/Al ratio. Moreover, lower Si/Al ratio was also connected to the reduction of smaller period to achieve steady-state (smaller induction periods) - which could be associated to the occurrence of selectivity inflexion points shifted for smaller conversions. Propylene, ethylene, and C_{6+} hydrocarbons display a maximum selectivity at the inflexion point, whereas aromatic and C_{4-5} present a minimum.

The following analysis, **figure 53**, aims to study the effect of acidity at iso-conversion. It is presented the dependency of space-times at which iso-conversions were achieved for each catalyst. Unfortunately, it was not possible to study S25 and S40 at 375º C and at iso-conversion due to the small data set of S40.

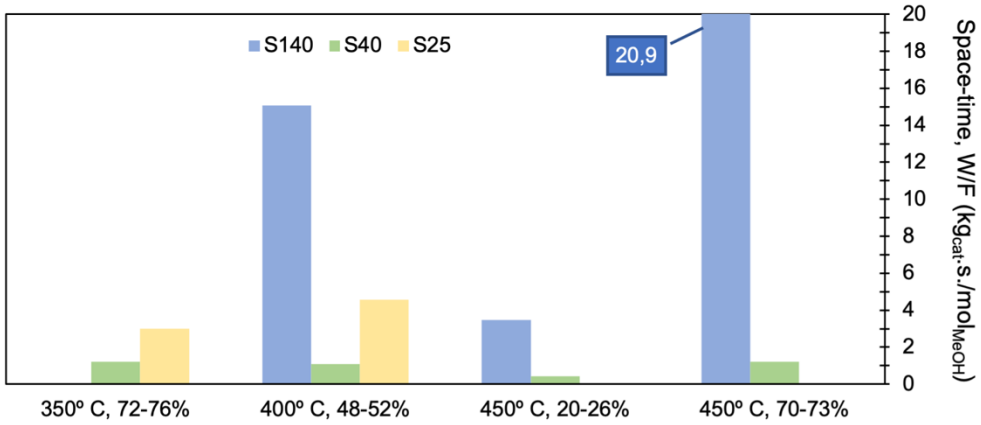

Figure 53 – Effect of acidity of H-ZSM-5 in space-time, at iso-conversion (P_{MeOH}=0.4 bar) at 350º, 400º and 450º C (W/F=[0, 21] $kg_{cat}.s/mol_{MeOH}$). Space-time of S140 (450º C, 70-73%) identified due to the range of the axis.

In line the representations in **figure 45, figure 53** depicts S140 achieving iso-conversions at much higher space-times than S40 a result of its considerably lower catalytic activity. This effect is increased with increasing temperature and with increasing conversion, since S40 presents a well-defined exponential phase. Therefore, comparison of the results for S40 and S140 is according to the expected.

A fundamental observation from **figure 53** is the effect of deactivation of S25. Although presenting higher acid density, S25 observes similar conversions reached at higher space-times than S40. Furthermore, S25 demonstrated higher-space times to achieve lower conversion at higher temperatures. This result is linked with the lower catalytic activity which was purely attributed the effect of deactivation. As greatly remarked already, all data acquired for S25 presents a certain degree of deactivation

These results clarify that in order to compare results for catalysts with higher Si/Al ratios (thus, lower catalytic activity and lower acid density) at iso-conversion, higher space-times must be aimed at. Conversely, similar space-times observe lower oxygenate conversion for increasing Si/Al ratios.

5.4.2 *Product Distribution*

In this analysis, the product distribution was averaged from results obtained within the 20 to 80% oxygenate conversion, according to the same principles described earlier. Moreover, error bars will depict the lowest and highest variation values achieved with the averaged selectivity.

Figure 54 illustrates the comparison of the results between catalysts for each set of temperatures.

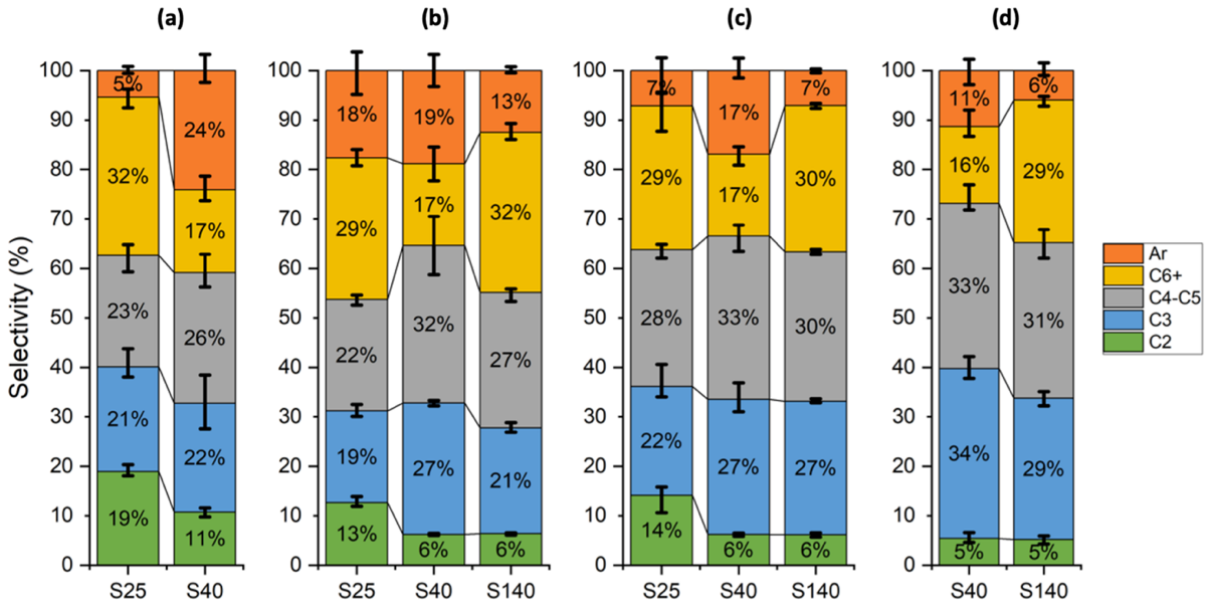

Figure 54 – Effect of H-ZSM-5 Si/Al ratio on the averaged product distribution of MTO at (a) 350º C, (b) 375º C, (c) 400º C, and (d) 450º C, within the range of oxygenate conversion of 20-80% and P_{MeOH}=0.4 bar.

From **figure 54**, ethylene and C_{6+} selectivities display a decrease with an increasing Si/Al ratio. Taking the temperature of 350º C as a reference, a decrease in 42% and 47% of the yield of these hydrocarbons (S25 to S40) is observed. Propylene and C_{4-5} species increase by 5% and 13%, respectively. These variations can be considered minor for they do not remark a substantial change in yields. Aromatic selectivity observes the largest variation, with an increase of 380% in selectivity.

S40 and S140 at higher temperatures observe comparable selectivities for C_2 and C_{4-5} hydrocarbons. Nevertheless, the analysis at 450º C remarks the greatest changes by the increase in 81% and decrease in 46% of C_{6+} and aromatic selectivity, respectively. Here, S40 verified the best performance for propylene yield maximization.

The same trend does not apply when comparing the three catalysts at iso-temperature. When comparing S40 to S140, a new tendency prevails where increasing Si/Al ratio observes higher C_{3-6+} hydrocarbon yields while decreasing C_2 and aromatic selectivity.

It is observed a slight increase of 11% in propylene yield at 375º C, accompanied by increases of 23% and 10% for C_{4-5} and C_{6+} (referring to the difference between S25 and S140). In turn, C_2 and aromatics present a decrease of 28% and 54%.

Overall, the rising and dropping of the Si/Al ratio from 40 appear to be related to higher aromatic and lower C_{6+} selectivities. These changes can be qualified as the most direct result of the effect of promotion of the aromatic cycle. **Figure 55** aims to investigate the mechanistic phenomena by addressing the ratios of E/Isob and AA between catalysts for each set of temperatures.

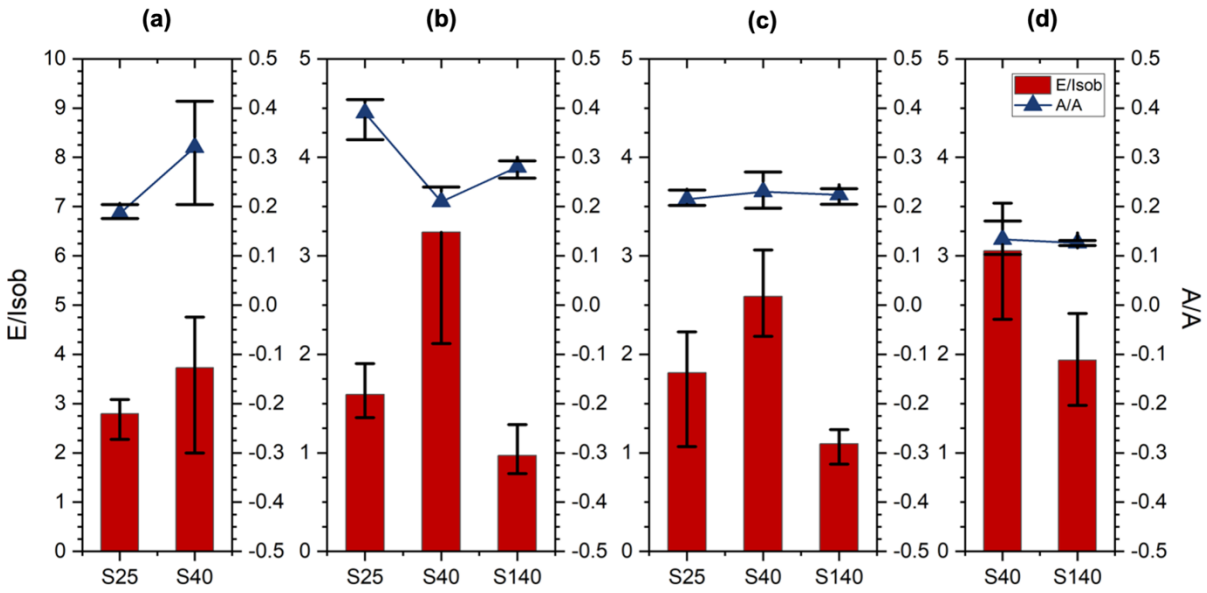

Figure 55 – Effect of H-ZSM-5 Si/Al ratio on the averaged ratio of E/Isob and A/A on MTO at (a) 350º C, (b) 375º C, (c) 400º C, and (d) 450º C, within the range of oxygenate conversion of 20-80% and P_{MeOH}=0.4 bar.

A pattern can be recognised in **figure 55**, where S40 is unmistakably favoured by aromatic cycle compared to the remaining catalysts. Interestingly, this pattern was observed in the activation energy and acid density studies. Hydrogen transfer rates, however, do not present a dependency on catalyst acidity with the only relevant variation occurring at 375º C with S25 and S40, arisen from the effect of deactivation.

When comparing S25 to S40 at 350º C, a rise of 33% of the predominance of the aromatic cycle is observed with an increasing Si/Al ratio. At 375º and 400º C, thus, increasing the effect of deactivation in S25; variations of 139% and 39% were observed. Hence, product distribution suggests an accentuated decrease in alkene methylation reactions in S40, responsible for the formation of higher olefins. With the increased production of aromatics and C_{2-3} olefins through aromatic methylation and dealkylation, the methylation of these olefinic species results in the observation of higher C_{3-5} hydrocarbons and lower C_2 selectivities.

S140 follows the same analysis when assessed in relation to S40. At 450º C it is depicted a decrease of 36% in E/Isob from S40. This effect was previously anticipated by the accentuated decrease in aromatic selectivity and the significant increase in C_{6+} species.

When compared to S25, S140 presents a higher prevalence of the alkene cycle with E/Isob ratios 40% lower for both temperatures. Moreover, the comparison of the results from S25 at 350º C with S140 at 375º C appears to be valid due to the low variation of selectivity of S140 with temperature. From these results, S25 appears to follow faster aromatic formation reactions and S140 higher rates of alkene methylation reaction, resulting in increased ethylene and lower aromatic species in the product distribution of S25.

Discussion

From the characterization studies, S40 presents a BAS/LAS ratio of 7.6 at 350º C, which does not substantially change from the acidity found at 150º C (total acidity). However, this ratio suffers an accentuated drop to 0.9 at 450º C (strong acidity). Overall, S25 and S140 verify higher BAS/LAS ratios compared to S40, with lower variations with increasing temperature (check **figure 39**). At 150º C, S25 and S140 register a BAS/LAS ratio of 7.6 and 9.6, whereas, at 450º C, these values decrease to 2.5 and 5.0.

Lower BAS_{strong}/LAS_{total} ratios appear to be directly linked with the propagation of the aromatic cycle. Since this effect is increasingly dominant with rising temperatures, it can be discerned a link with the prevailing strong Brønsted acidity – where MTO reaction is thought to occur. In addition, strong BAS are considered the primarily centres where coke deposition occurs **[122, 123]**.

At temperatures below 375º C, catalytic activity and product distribution evolve according to the temperature effect as acidity distribution remains unaltered. This effect promotes the propagation of the alkene cycle and has been verified by several works at lower temperatures **[110, 112]**.

As a result of the swift change in the active acid sites, the effect of acidity is expressed by the promotion of the aromatic cycle, which is more prevalent than the effect of temperature. Thus, it is observed an increase in the E/Isob ratios above 375º C with a higher prevalence for S40. The considerable decrease in strong BAS in this catalyst justifies the increased effect of acidity manifested by the promotion of the aromatic cycle.

The effect of acidity can therefore be summarized by the relationship between BAS_{strong}/LAS_{total} and, in the present case, by strong/weak acid sites ratios. These observations can be supported by the observations of several authors. The work of Huang et al. (2019) also verified the promotion of the aromatic up an inflexion point, located at precisely between Si/Al of 50 and 200 (consult **figure 26**) **[118]**. Moreover, Feng et al. (2020) also attributed the better propylene performance to lower strong acid site density (translated in lower BAS_{strong}/LAS_{total} ratios) **[119]**. From the results in present work, Huang et al. (2019), and Sun (2013), it can be hypothesized that the inflexion point for the maximum contribution of the aromatic cycle should occur between Si/Al of 100 and 140 (or 40 and 140 if only considering the present work) **[110, 118]**.

Zeolite defective sites, as encountered in S140 (and S25 in a lesser extent), present little to no acidity, which might implicate the lower relative LAS when compared to S40. Furthermore, defects have been shown to negatively affect coke capacity and coke mobility **[182]**. This, in addition to higher strong BAS, clarifies the results obtained at 350º C where S25 presents a similar catalytic activity to S40 but with a much higher rate of deactivation.

Moreover, the best preservation of BAS_{strong}/LAS_{total} ratio in S25 and S140 compared to S40 result in the hypothesis that structural defective sites stabilize Brønsted acidity – which has already been suggested by other works **[165, 171]**.

In the case of S140, the lower TAS density, higher relative mesopore volume, and higher external surface, result in higher distances between adjacent active centres. In accordance with conclusion by Yarulina et al. (2018), catalysts with more isolated BAS (generally associated with lower acid density catalysts) present improved propylene selectivity and lower deactivation rates **[57]**.

The lower activation energies and the mechanistic pathways observed for S25 and S140 can be correlated with the acid site nature. Similar LAS densities are found for S25 and S40, while S140 and S25 verify higher relative strong acidity.

From this analysis results the hypothesis that strong BAS can be linked with the alkene homologation cycle reactions, more importantly, for the higher rates of alkene methylation and cracking reactions. LAS appear to preferentially stabilize aromatic species from which dealkylation and cyclization reactions occur, providing the higher propylene yields alongside with higher aromatic. Furthermore, it can also be deduced that LAS are responsible for the higher apparent activation energy observed in S40 (consult **Annex C1**).

Of course, it cannot be discarded the possibility that isobutane was considerably underestimated, thus, presenting higher E/Isob ratios, or even that this relationship does not accurately describe the aromatic/alkene cycles as literature has led to understand. However, the previous reasonings were aligned with several works and with the catalyst characterization results obtained by py-FTIR. Additional studies should focus on validating the results of Si/Al of 40 and testing catalysts with higher and lower Si/Al ratios outside the range of these studies.

Several studies that focus on the conversion of methanol to aromatics validate these hypotheses. It has been found that the effect of conversion impacts on light aromatic's selectivity (benzene, toluene, and xylene) is affected by the acid density and by the acidic nature **[183, 184]**. Li et al. (2021) mentions in their work a "synergism" between BAS and LAS to be related to the product distribution **[185, 186]**. Furthermore, Jia et al. (2017) and Barthos et al. (2007) concluded that Lewis acid sites are favourable to the aromatization of olefins from which MB are formed **[183, 184, 187]**.

These findings are aligned with the observations and conclusions in this work, stating that MTO reaction follows a two-site reaction mechanism. However, it is not clear whether both Lewis and Brønsted sites catalyse the same reactions at different rates or whether these are reaction selective.

5.5 *Overview*

Catalytic studies for H-ZSM-5 with Si/Al ratios of 25, 40 and 140 (S25, S40, S140) were conducted at a constant methanol partial pressure of 0.4 bar in the 350-450º C temperature range. Data were acquired under steady-state and intrinsic kinetics regimes in order to evaluate the MTO kinetic parameters, the effect of conversion, temperature, and acidity in the product distribution for the maximization of propylene yield. Ethylene/isobutane (E/Isob) ratio was used as a measurement of the contribution of the aromatic/alkene cycles, whilst the alkane/alkene ratios were used as a representation of the extent of the hydrogen transfer reactions.

A comprehensive process was established to access the stage of deactivation. Data were analysed according to their TOS profile and preliminary catalytic activity studies. The study of selectivity demonstrated that data points with a small degree of deactivation hold reliable product distribution information. Data selection was essential to maximize the available experimental data.

Lower Si/Al ratio catalyst presented a shortening of the period to achieve steady-state. However, deactivation was largely responsible for preventing thorough studies, with S25 presenting deactivation within the first 3-4h TOS at 375º C, compared to over 20h TOS of stability for S140. This effect was increased with increasing temperatures. All S25 data presented a certain degree of deactivation. S40 at 375º C was dismissed for catalytic studies due to the insufficiency of data points available. Due to the high stability (over 20h TOS of lifetime), all data of S140 was considered reliable.

Catalytic studies considered data within the 20-80% oxygenate conversion. Catalytic activity displayed a severe dependency on catalyst preparation; thus, all parameters were compared to the same catalyst batch.

Catalytic activity decreased with increasing Si/Al ratio and increased with rising temperature. S25 presented 18% lower catalytic activity at 350º C compared to S40, which was attributed to the already existing stage of deactivation. S140 presented a catalytic activity 95% lower than S40 at 400º and 450º C. Apparent activation energies of 45, 85, and 14 kJ/mol were calculated for S25, S40, and S140. Although these values resulted from Arrhenius plots with two temperature references, the antecedent regressions were found to accurately describe the system and validated the approximation to a first-order reaction. It can be strongly hypothesized that activity was underestimated for S25, however, if similar degrees of deactivation were present, activation energy might not have suffered a significant deviation. The scarcity of reliable intrinsic kinetic data in the literature prevented the validation of these results.

E/Isob as a function of oxygenate conversion presents a concave polynomial behaviour, with the inflexion point marking a maximum of the contribution of the aromatic cycle at approximately 60% conversion in which propylene, ethylene, and C_{6+} yields are maximized. Nonetheless, as selectivity was found to not change substantially across 20-80% oxygenate conversion, this interval was used thereon as the mean average for product distribution in each experimental condition.

Studies at similar space-times display lower oxygenate conversion for increasing Si/Al ratios and temperature displayed a highest effect on aromatics and C_3 selectivity (**figure 56**).

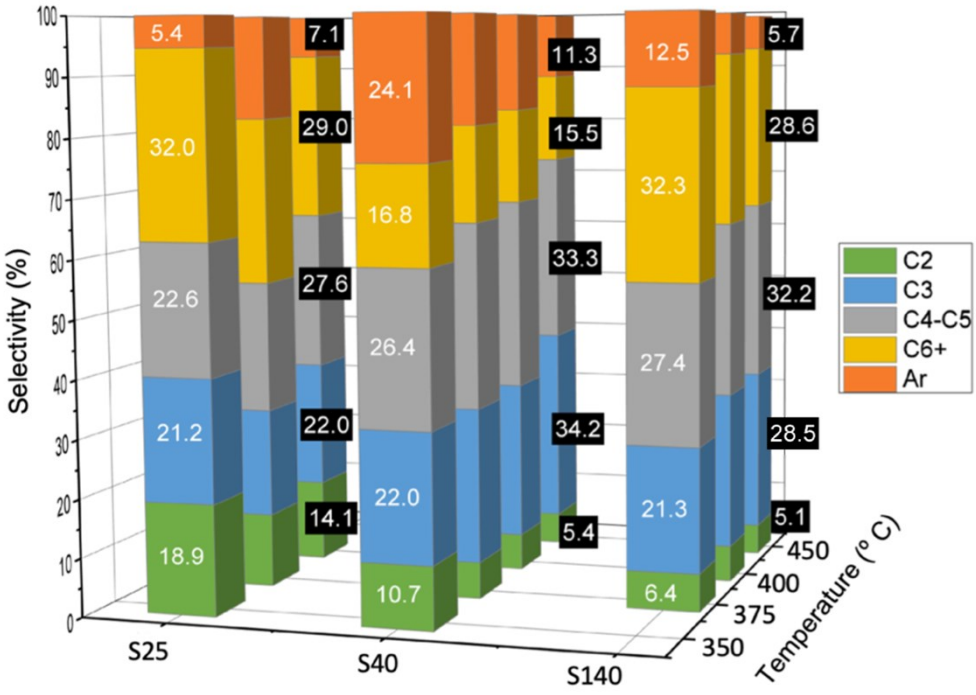

Figure 56 – Effect of H-ZSM-5 Si/Al ratio and temperature on the averaged product distribution of MTO, within the range of oxygenate conversion of 20-80% and P_{MeOH}=0.4 bar.

Increased temperature and Si/Al ratio also presented second-order polynomial behaviours regarding the prevalence of the aromatic/alkene cycles. Temperature displayed a clear change in regime at 375º/400º C where the alkene cycle contribution reaches a high before the aromatic cycle resumes its increasing influence (**figure 56**). Propylene's and C_{4-5} products' selectivity was increased with increasing temperature while aromatic and ethylene selectivity decreased.

Propylene yield and propylene/ethylene ratio were maximized at higher temperatures. S40 displayed the best performance of this olefin, achieving 34% selectivity for the reaction temperature of 450º C, with a propylene/ethylene ratio of 5.3. At the same temperature, S140 presented 29% propylene yielding (propylene/ethylene ratio of 5.2) whilst preserving a much higher stability of TOS.

Lower BAS_{strong}/LAS_{total} ratios were linked with the propagation of the aromatic cycle. This effect is promoted by rising temperatures where stronger acidity prevails. The effect of acidity can therefore be summarized by the relationship between BAS_{strong}/LAS_{total} as well as by the ratio of strong/weak acid sites ratios in the present study.

Below 375º C, where BAS/LAS ratios remain unaltered, catalytic activity and product distribution evolve according to the temperature effect, correlated to the promotion of the alkene cycle.

The effect of acidity prevails over the effect of temperature above 375º C (within the studied range) from the change in the relative acid site distribution (decreasing BAS_{strong}/LAS_{total}). Verifying

the most accentuated decrease in relative BAS density, the aromatic cycle was the most prevalent in the case of S40. Si/Al ratio between 40 (or 100, considering other works) and 140 can be hypothesized as the interval at which the aromatic cycle finds its maximum propagation (inflexion point) **[110, 118]**.

From S25 and S140 studies, the lower LAS by the increase in defect sites was correlated with higher deactivation rates (from the stabilization of strong BAS) and higher diffusion limitations. The lower total acid site density, higher relative volume of mesopores, and higher external surface counteracted the previous effect in S140 by decreasing catalyst activity and promoting diffusion of larger molecules (such as poly-substituted aromatics).

The lower activation energies obtained for S25 and S140 were correlated with the acid site nature, indicating that LAS are responsible for the higher apparent activation energies and better aromatic intermediates stabilization (promotion of dehydrogenation and cyclization reactions); thus, propagating the aromatic cycle. Furthermore, it was determined that MTO is a two-site reaction system, although it is yet not clear the exact contribution of each acid centre for the dual-cycle mechanism. These findings were supported by multiple works in the literature **[110, 112, 113, 118, 119, 183-187]**.

6 *Conclusions and Prospects*

Through zeolite characterization and catalyst studies, the present work aimed to understand the influence of H-ZSM-5 acidity in the maximization of propylene yield. Accordingly, H-ZSM-5 with Si/Al ratios of 25, 40, and 140 (S25, S40, and S140, respectively) were studied.

Zeolite characterization results from ICP-OES and XRD techniques were in conformity with previous reports. Furthermore, nitrogen physisorption studies demonstrated that the calcination process preserved the catalyst's framework whilst promoting mesoporosity. The three catalysts displayed similar pore volumes and pore diameters, with S140 exhibiting higher relative mesopore volume and higher external surface area.

Pyridine Fourier-transform infrared spectroscopy (py-FTIR) characterized the acid sites density and strength. S25 also presented the highest acid site density. Lewis acidity was conserved throughout the studied adsorption temperatures (150-450º C). Strong Brønsted acidity was best preserved in S25 and S140, which was linked to the presence of structural defects. Furthermore, S40 registered the lowest ratio between the strong Brønsted acidity and total Lewis acidity.

In literature, most studies report data studied with a disregard for the influence of transport phenomena and the effect of deactivation. To properly access the effect of H-ZSM-5 acidity on MTO, systematic catalytic studies were conducted at steady-state and all data were acquired under an intrinsic kinetic regime, with a comprehensive study of the data for detection of deactivation.

The MTO kinetic parameters and product distribution were studied by the variation of operating conditions. Conversion and temperature effect on product distribution followed the expected trend from literature, with a maximum selectivity towards propylene at approximately 60% conversion, promoted by increasing temperatures.

The established deactivation assessment procedure resulted in the accurate identification of deactivated data. It was determined that data sets presenting a small degree of deactivation still hold reliable selectivity information which allowed for the preservation of more data. Associated with a lower acid site density, S140 presented the best catalytic stability whilst observing a much lower catalytic activity. Due to the very fast deactivation, the study of S25 faced several challenges. Furthermore, catalytic activity exhibited a high dependency on the catalyst batch.

The findings of this work suggest the MTO reaction follows a two-site reaction mechanism. Lewis acid sites were related to the stabilization of poly-aromatic intermediates (promoting cyclization and dehydrogenation reactions), and linked with the higher apparent activation energy found in S40. These results exposed a correlation between the lower relative strong Brønsted acidity and the propagation of the aromatic cycle, which should peak in catalysts with Si/Al ratios between 40 and 140. The lower acid site density, higher relative mesopore volume, and higher external surface area displayed by S140 resulted in lower deactivation rates and improved propylene yields.

Although S40 depicted the best performance regarding propylene yielding (from the promotion of the aromatic cycle), S140 displayed similar results whilst maintaining a much higher catalyst lifetime. For industry purposes, where operations are continuous and conducted at steady-state, S140 emerges with a much higher interest. Furthermore, the claims presented in this work can be found scattered in several studies in the literature.

From this work, it is not conclusive the reaction pathway ascribed to Lewis and Brønsted acid sites. In order to understand the entirety of the catalysed reactions (reaction selectivity) that occur in the two acid site types, it would be beneficial to proceed with the catalytic studies and acidity characterization with catalysts with different Si/Al ratios. Preferentially, these studies (under intrinsic kinetic regimes, steady-state, and comparable operating conditions) would involve zeolites with Si/Al ratios such as 200, 120. In the range of these ratios, catalyst stability is not expected to present a challenge, resulting in reliable kinetic data acquisition. Furthermore, it would investigate the Si/Al ratio at which the aromatic cycle promotion and propylene yield are maximized. This data could allow the construction of a reaction model and indisputably validate the previous conclusions. Furthermore, these studied could also include the analysis of coke deposited on the catalysts after the catalytic testing.

Moreover, in order expedite the study of reaction kinetics, Lewis acidity can be produced through Al_{EF} species created from dealumination (from hydrothermal/steaming or acid treatment), followed by a controlled desilication (basic treatment) to arrange the mesopore structure. However, in a first study it would be advised to explore the properties of commercial catalyst from the same supplier.

Subsequently, the modulation of catalyst properties in order to maximize stability and yielding would become the next step. Studies with zeolites with different preparation and modification methods, such as commercial zeolites compared to hierarchal zeolites, either hydrothermally synthesized with different crystallization temperatures or modified with metal insertions with different loadings, would allow for controlled exploration of manipulation of zeolite properties such as increased mesoporosity and promotion of lower weak/strong acidity; thus, allowing for improved catalyst design.

References

Introduction

1. Boffey, D. (2020, Oct. 8). EU parliament votes for 60% greenhouse gas emissions cut by 2030. The Guardian. https://www.theguardian.com/world/2020/oct/08/eu-parliament-votes-carbon-greenhouse-gas-emissions-reduction-2030 (consulted in 23/02/2021).

2. Ritchie, H. (2020, Sept. 18). Sector by sector: where do global greenhouse gas emissions come from? Our World in Data. https://ourworldindata.org/ghg-emissions-by-sector (consulted in 23/02/2021).

3. Rodgers, B. L. (2018, Dec. 17). Climate change: The massive CO2 emitter you may not know about. BBC News. https://www.bbc.com/news/science-environment-46455844 (consulted in 23/02/2021).

4. Cementing: the European Green Deal. CEMBUREAU. http://www.atic.pt/wp-content/uploads/2020/05/cembureau-2050-roadmap_final-version_web-1.pdf

5. Clean Energy For All Europeans. European Commission: Communication from the Commission. Brussels, 30.11.2016. COM (2016) 860 final. https://eur-lex.europa.eu/legal-content/EN/TXT/HTML/?uri=CELEX:52016DC0860&rid=5

6. Worland, J. (2019, Nov. 13). Countries Are Falling Far Short on Action to Tackle Climate Change as Fossil Fuel Use Increases. Energy Report. Time. https://time.com/5726917/energy-demand-iea-report/ (consulted in 23/02/2021).

7. Harrisson, T. (2020, Oct. 5). Analysis: Global fossil-fuel emissions up 0.6% in 2019 due to China. Carbon Brief. https://www.carbonbrief.org/analysis-global-fossil-fuel-emissions-up-zero-point-six-per-cent-in-2019-due-to-china (consulted in 23/02/2021).

8. The Freeing Energy Project. (2020, Nov. 25). Fossil Fuel Reserves Will Become Unviable. Freeing Energy. https://www.freeingenergy.com/energy-fact-fossil-fuel-reserves-will-become-unviable-g120/ (consulted in 23/02/2021).

9. Environmental Impacts of Natural Gas. (2014, July 19). Union of Concerned Scientists. https://www.ucsusa.org/resources/environmental-impacts-natural-gas (consulted in February 23, 2021).

10. Comparison Against Other Fossil Fuels. (2018, Sept. 26). Swarthmore. https://www.swarthmore.edu/environmental-studies-capstone/comparison-against-other-fossil-fuels#3 (consulted in 23/02/2021).

11. Grand View Research. (2020, June). Plastics Market Size, Share & Trends Report, 2020-2027. https://www.grandviewresearch.com/industry-analysis/global-plastics-market (consulted in 24/02/2021).

12. Statista. (2021, Jan. 27). Global market value of plastic 2018-2027. https://www.statista.com/statistics/1060583/global-market-value-of-plastic/ (consulted in 24/02/2021).

13. Polymer Solutions News Team. (2016, Aug. 16). Polyolefins are Everywhere! Polymer Solutions Incorporated. https://www.polymersolutions.com/blog/top-types-of-polyolefins-the-most-common-kind-of-plastics/ (consulted in 24/02/2021).

14. Nexant (2014, Nov.). Petrochemical Outlook: Challenges and Opportunities. Executive Summary Report. Prepared for Organization of the Petroleum Exporting Countries (OPEC).

15. Olefins Market | Industry Size, Share & Analysis, 2020-2027. (2020, March). Reports and Data. https://www.reportsanddata.com/report-detail/olefins-market (consulted in 03/03/2021).

16. Petrochemicals Make Things Happen (flowchart). Petrochemicals Europe, CEFIC 2021.

17. How to Make Propylene and Ethylene at the Lowest Cash Cost of Production? (2019, Sept. 17). How To Find The Money. https://www.howtofindthemoney.com/2019/09/how-to-make-propylene-and-ethylene-at-the-lowest-cash-cost-of-production.html (consulted in 11/03/2021).

18. Rent, T., Patel, M., & Blok, K. (2006). Olefins from conventional and heavy feedstocks: Energy use in steam cracking and alternative processes. Energy, 31(4), 425–451. doi:10.1016/j.energy.2005.04.001

19. Hannula, I., & Arpiainen, V. (2014). Light olefins and transport fuels from biomass residues via synthetic methanol: performance and cost analysis. Biomass Conversion and Biorefinery. doi:10.1007/s13399-014-0123-9

20. Zacharopoulou, V., & Lemonidou, A. (2017). Olefins from Biomass Intermediates: A Review. Catalysts, 8(1), 2. doi:10.3390/catal8010002

21. Hisham A. Maddah. (2018). A Comparative Study between Propane Dehydrogenation (PDH) Technologies and Plants in Saudi Arabia. American Scientific Research Journal for Engineering, Technology, and Sciences (ASRJETS) (2018) Volume 45, No 1, pp 49-63

22. Sai Chen, Xin Chang, Guodong Sun, Tingting Zhang, Yiyi Xu, Yang Wang, Chunlei Pei, Jinlong Gong. (2021). Propane dehydrogenation: catalyst development, new chemistry, and emerging technologies. Chem. Soc. Rev. 2021. The Royal Society of Chemistry. doi: 10.1039/d0cs00814a

23. Cai, D., Wang, N., Chen, X., Ma, Y., Hou, Y., Li, X., … Wei, F. (2019). Highly selective conversion of methanol to propylene: design of an MFI zeolite with selective-blockage of (010) surfaces. Nanoscale. doi:10.1039/c8nr10371b

24. National Academies of Sciences, Engineering, and Medicine 2016. The Changing Landscape of Hydrocarbon Feedstocks for Chemical Production: Implications for Catalysis: Proceedings of a Workshop. Washington, DC: The National Academies Press. doi: 10.17226/23555.

25. GlobalData. (2021, Jan. 5). China to lead global propylene capacity additions by 2030. https://www.globaldata.com/china-lead-global-propylene-capacity-additions-2030-says-globaldata/ (consulted in 23/02/2021).

26. GlobalData. (2020, December). Global Ethylene Capacity and Capital Expenditure Outlook to 2030 - Asia Leads Globally in Terms of Ethylene Capacity Additions.

27. Eramo, M. (2019, March 20). Global basic chemicals outlook. IHS Markit. https://ihsmarkit.com/research-analysis/global-basic-chemicals-outlook.html (consulted in 23/02/2021).

28. Propene (Propylene). (2017, January 26). The Essential Chemical Industry - Online. https://www.essentialchemicalindustry.org/chemicals/propene.html (consulted in 23/02/2021).

29. Propylene Uses and Market Data. (2010, May 14). ICIS Explore. https://www.icis.com/explore/resources/news/2007/11/06/9076455/propylene-uses-and-market-data/ (consulted 23/02/2021).

30. Sawyer, G. (2018, Feb. 26). Basics of the Chemical Industry – Propylene & Its Products. AIChE. https://www.aiche.org/academy/videos/basics-chemical-industry-propylene-its-products (consulted in 23/02/2021).

31. Chen, William. "Propylene Industry Developments in Northeast Asia." IHS Markit, 14 Jan. 2021, https://www.ihsmarkit.com/research-analysis/propylene-industry-developments-in-northeast-asia.html (consulted in 27/02/2021).

32. Akah, A., Williams, J., & Ghrami, M. (2019). An Overview of Light Olefins Production via Steam Enhanced Catalytic Cracking. Catalysis Surveys from Asia.doi:10.1007/s10563-019-09280-6

33. Liu, W.-C., Baek, J., & Somorjai, G. A. (2018). The Methanol Economy: Methane and Carbon Dioxide Conversion. Topics in Catalysis, 61(7-8), 530–541. doi:10.1007/s11244-018-0907-4

34. Sherrard, A. (2020, October 25). Belgian stakeholders launch North-C-Methanol project. Bioenergy International. https://bioenergyinternational.com/biochemicals-materials/belgian-stakeholders-launch-north-c-methanol-project

35. Gogate, M. R. (2019). Methanol-to-olefins process technology: current status and future prospects. Petroleum Science and Technology, 1–7.doi:10.1080/10916466.2018.1555589

36. Tian, P., Wei, Y., Ye, M., & Liu, Z. (2015). Methanol to Olefins (MTO): From Fundamentals to Commercialization. ACS Catalysis, 5(3), 1922–1938.doi:10.1021/acscatal.5b00007

37. Yang, M., Fan, D., Wei, Y., Tian, P., & Liu, Z. (2019). Recent Progress in Methanol-to-Olefins (MTO) Catalysts. Advanced Materials, 1902181. doi:10.1002/adma.201902181

38. Salkuyeh, Y., & Il, T. (2015). Co-Production of Olefins, Fuels, and Electricity from Conventional Pipeline Gas and Shale Gas with Near-Zero CO2 Emissions. Part I: Process Development and Technical Performance. Energies, 8(5), 3739–3761. doi: 10.3390/en8053739

State of the Art

39. Hemelsoet, K., Van der Mynsbrugge, J., De Wispelaere, K., Waroquier, M., & Van Speybroeck, V. (2013). Unraveling the Reaction Mechanisms Governing Methanol-to-Olefins Catalysis by Theory and Experiment. ChemPhysChem, 14(8), 1526–1545. doi:10.1002/cphc.201201023

40. BARGER, P. (2002). METHANOL TO OLEFINS (MTO) AND BEYOND. Catalytic Science Series, 239–260. doi:10.1142/9781860949555_0012

41. Boltz, Marilyne & Losch, Pit & Louis, Benoit. (2013). A General Overview on the Methanol to Olefins Reaction: Recent Catalyst Developments. Advanced Chemistry Letters. 1. doi:10.1166/acl.2013.1032

42. Stöcker, M. (1999). Methanol-to-hydrocarbons: catalytic materials and their behavior. Microporous and Mesoporous Materials, 29(1-2), 3–48. doi:10.1016/s1387-1811(98)00319-9

43. "Swiss Company Outlines Methanol-to-Gasoline Option for Alaska North Slope Gas to State Legislature." Green Car Congress, 1 May 2011, www.greencarcongress.com/2011/05/janus-20110501.html (consulted in 27/02/2021).

44. "10.4. Conversion of Methanol to Gasoline." National Energy Technology Laboratory, www.netl.doe.gov/research/coal/energy-systems/gasification/gasifipedia/methanol-to-gasoline (consulted in 27/02/2021).

45. Joe E. Penick, Sergei Y. John, C. Zahner. (1982). Conversion of methanol to gasoline (US4404414A). ExxonMobil Oil Corp.

46. Brownstein, A. M. (2015). Synthesis Gas-Based Fuels. Renewable Motor Fuels, 33–46. doi:10.1016/b978-0-12-800970-3.00004-2

47. Coal to Olefins (CTO) / Methanol to Olefins (MTO) API Production. (2019) Flowserve. Application Solutions Guide.

48. Jasper, S., & El-Halwagi, M. (2015). A Techno-Economic Comparison between Two Methanol-to-Propylene Processes. Processes, 3(3), 684–698. doi:10.3390/pr3030684

49. Koempel, H., & Liebner, W. (2007). Lurgi's Methanol To Propylene (MTP®) Report on a successful commercialisation. Natural Gas Conversion VIII, Proceedings of the 8th Natural Gas Conversion Symposium, 261–267. doi:10.1016/s0167-2991(07)80142-x

50. Nesterenko, N., Aguilhon, J., Bodart, P., Minoux, D., & Dath, J.-P. (2016). Methanol to Olefins. Zeolites and Zeolite-Like Materials, 189–263. doi:10.1016/b978-0-444-63506-8.00006-9

51. Cui, Kelly. "How Are Olefins Made from CTO/MTO?" Wood Mackenzie, 1 Nov. 2017, www.woodmac.com/news/editorial/how-are-olefins-made-from-cto-mto/ (consulted in 27/02/2021).

52. "Methanol to Olefins (DMTO) Process Won State Technological Invention Awards First Prize." Dalian Institute of Chemical Physics (DICP), Chinese Academy of Sciences, 2015, http://english.dicp.cas.cn/ns_17179/icn/201409/t20140921_128249.html.

53. Amghizar, I., Vandewalle, L. A., Van Geem, K. M., & Marin, G. B. (2017). New Trends in Olefin Production. Engineering, 3(2), 171–178. doi:10.1016/j.eng.2017.02.006

54. Ren, T., Patel, M., & Blok, K. (2008). Steam cracking and methane to olefins: Energy use, CO2 emissions and production costs. Energy. doi:10.1016/j.energy.2008.01.002

55. Cui, Kelly. "The Opportunities and Challenges of CTO/MTO Development." Wood Mackenzie, Verisk, 7 Nov. 2017, www.woodmac.com/news/editorial/the-opportunities-and-challenges-of-cto-mto-development/ (consulted in 26/02/2021).

56. Nasr MRJ, Sahebdelfar S, Ravanchi MT, Beshelli MD. (2011). Integration of Petrochemical and Refinery Plants as an Approach to Compete in Hydrocarbon Market.

57. Yarulina, I., Chowdhury, A. D., Meirer, F., Weckhuysen, B. M., & Gascon, J. (2018). Recent trends and fundamental insights in the methanol-to-hydrocarbons process. Nature Catalysis, 1(6), 398–411. doi:10.1038/s41929-018-0078-5

58. Xu, S., Zhi, Y., Han, J., Zhang, W., Wu, X., Sun, T., … Liu, Z. (2017). Advances in Catalysis for Methanol-to-Olefins Conversion. Advances in Catalysis, 37–122. doi:10.1016/bs.acat.2017.10.002

59. Qi, L., Wei, Y., Xu, L., & Liu, Z. (2015). Reaction Behaviors and Kinetics during Induction Period of Methanol Conversion on HZSM-5 Zeolite. ACS Catalysis, 5(7), 3973–3982. doi:10.1021/acscatal.5b00654

60. Hazrati, Hossein. (2018). Selective production of light olefins from methanol over desilicated highly siliceous ZSM-5 nanocatalysts. Polyolefins Journal. 5. doi:10.22063/poj.2017.1501

61. Yarulina, I., Bailleul, S., Pustovarenko, A., Martinez, J. R., Wispelaere, K. D., Hajek, J., … Gascon, J. (2016). Suppression of the Aromatic Cycle in Methanol-to-Olefins Reaction over ZSM-5 by Post-Synthetic Modification Using Calcium. ChemCatChem, 8(19), 3057–3063. doi:10.1002/cctc.201600650

62. Standl, S., & Hinrichsen, O. (2018). Kinetic Modeling of Catalytic Olefin Cracking and Methanol-to-Olefins (MTO) over Zeolites: A Review. Catalysts, 8(12), 626. doi:10.3390/catal8120626

63. Stöcker, M. (2010). Methanol to Olefins (MTO) and Methanol to Gasoline (MTG). Zeolites and Catalysis, 687–711. doi:10.1002/9783527630295.ch22

64. Zhu, J., Li, Y., Muhammad, U., Wang, D., & Wang, Y. (2017). Effect of alkene co-feed on the MTO reactions over SAPO-34. Chemical Engineering Journal, 316, 187–195. doi:10.1016/j.cej.2017.01.090

65. Sun, X., Mueller, S., Shi, H., Haller, G. L., Sanchez-Sanchez, M., van Veen, A. C., & Lercher, J. A. (2014). On the impact of co-feeding aromatics and olefins for the methanol-to-olefins reaction on HZSM-5. Journal of Catalysis, 314, 21–31. doi:10.1016/j.jcat.2014.03.013

66. Martinez-Espin, J. S., Mortén, M., Janssens, T. V. W., Svelle, S., Beato, P., & Olsbye, U. (2017). New insights into catalyst deactivation and product distribution of zeolites in the methanol-to-hydrocarbons (MTH) reaction with methanol and dimethyl ether feeds. Catalysis Science & Technology, 7(13), 2700–2716. doi:10.1039/c7cy00129k

67. Zang, K., Zhang, W., Huang, J., Feng, P., & Ding, J. (2019). First molecule with carbon–carbon bond in methanol-to-olefins process. Chemical Physics Letters, 737, 136844. doi:10.1016/j.cplett.2019.136844

68. Chang, C. (1977). The conversion of methanol and other O-compounds to hydrocarbons over zeolite catalysts. Journal of Catalysis, 47(2), 249–259. doi:10.1016/0021-9517(77)90172-5

69. Peng, Chao & Wang, Hai & Hu, Peijun. (2016). Theoretical Insight into How the First C-C Bond Forms in the Methanol-to-Olefin Process Catalysed by HSAPO-34. Phys. Chem. Chem. Phys. 18. doi:10.1039/C5CP08029K

70. Haw, J. F., & Marcus, D. M. (2005). Well-defined (supra)molecular structures in zeolite methanol-to-olefin catalysis. Topics in Catalysis, 34(1-4), 41–48. doi:10.1007/s11244-005-3798-0

71. Zhang, M., Xu, S., Wei, Y., Li, J., Chen, J., Wang, J., … Liu, Z. (2016). Methanol conversion on ZSM-22, ZSM-35 and ZSM-5 zeolites: effects of 10-membered ring zeolite structures on methylcyclopentenyl cations and dual cycle mechanism. RSC Advances, 6(98), 95855–95864. doi:10.1039/c6ra08884h

72. Jing, B., Li, J., Li, Z., Wang, S., Qin, Z., Fan, W., & Wang, J. (2017). Comparative Study of Methanol to Olefins Over ZSM-5, ZSM-11, ZSM-22 and EU-1: Dependence of Catalytic Performance on the Zeolite Framework Structure. Journal of Nanoscience and Nanotechnology, 17(6), 3680–3688. doi:10.1166/jnn.2017.13986

73. Pit Losch. Synthesis and characterisation of zeolites, their application in catalysis and subsequent rationalisation : methanol-to-olefins (MTO) process with designed ZSM-5 zeolites. Catalysis. Université de Strasbourg, 2016. English. NNT : 2016STRAF035 . tel-01531844

74. Liu, Y., Müller, S., Berger, D., Jelic, J., Reuter, K., Tonigold, M., … Lercher, J. A. (2016). Formation Mechanism of the First Carbon-Carbon Bond and the First Olefin in the Methanol Conversion into Hydrocarbons. Angewandte Chemie International Edition, 55(19), 5723–5726. doi:10.1002/anie.201511678

75. Zang, K., Zhang, W., Huang, J., Feng, P., & Ding, J. (2019). First molecule with carbon–carbon bond in methanol-to-olefins process. Chemical Physics Letters, 737, 136844. doi:10.1016/j.cplett.2019.136844

76. Liu, Y., Müller, S., Berger, D., Jelic, J., Reuter, K., Tonigold, M., … Lercher, J. A. (2016). Formation Mechanism of the First Carbon-Carbon Bond and the First Olefin in the Methanol Conversion into Hydrocarbons. Angewandte Chemie International Edition, 55(19), 5723–5726. doi:10.1002/anie.201511678

77. Gunawardena, D. A., & Fernando, S. D. (2012). Thermodynamic Equilibrium Analysis of Methanol Conversion to Hydrocarbons Using Cantera Methodology. Journal of Thermodynamics, 2012, 1–7. doi:10.1155/2012/125460

78. Dahl, I. M., & Kolboe, S. (1994). On the Reaction Mechanism for Hydrocarbon Formation from Methanol over SAPO-34. Journal of Catalysis, 149(2), 458–464. doi:10.1006/jcat.1994.1312

79. Svelle, S., Joensen, F., Nerlov, J., Olsbye, U., Lillerud, K.-P., Kolboe, S., & Bjørgen, M. (2006). Conversion of Methanol into Hydrocarbons over Zeolite H-ZSM-5: Ethene Formation Is Mechanistically Separated from the Formation of Higher Alkenes. Journal of the American Chemical Society, 128(46), 14770–1477. doi:10.1021/ja065810a

80. Haw, J. F., Song, W., Marcus, D. M., & Nicholas, J. B. (2003). The Mechanism of Methanol to Hydrocarbon Catalysis. Accounts of Chemical Research, 36(5), 317–326. doi:10.1021/ar020006o

81. Lesthaeghe, D., Horré, A., Waroquier, M., Marin, G. B., & Van Speybroeck, V. (2009). Theoretical Insights on Methylbenzene Side-Chain Growth in ZSM-5 Zeolites for Methanol-to-Olefin Conversion. Chemistry - A European Journal, 15(41), 10803–10808. doi:10.1002/chem.200901723

82. Li, C., Paris, C., Martínez-Triguero, J., Boronat, M., Moliner, M., & Corma, A. (2018). Synthesis of reaction-adapted zeolites as methanol-to-olefins catalysts with mimics of reaction intermediates as organic structure-directing agents. Nature Catalysis, 1(7), 547–554. doi:10.1038/s41929-018-0104-7

83. Peng, C., Wang, H., & Hu, P. (2016). Theoretical insights into how the first C–C bond forms in the methanol-to-olefin process catalysed by HSAPO-34. Physical Chemistry Chemical Physics, 18(21), 14495–14502. doi:10.1039/c5cp08029k

84. McCann, D. M., Lesthaeghe, D., Kletnieks, P. W., Guenther, D. R., Hayman, M. J., Van Speybroeck, V., Waroquier, M., & Haw, J. F. (2008). A Complete Catalytic Cycle for Supramolecular Methanol-to-Olefins Conversion by Linking Theory with Experiment. Angewandte Chemie International Edition, 47(28), 5179–5182. doi:10.1002/anie.200705453

85. Fečík, M., Plessow, P. N., & Studt, F. (2021). Theoretical investigation of the side-chain mechanism of the MTO process over H-SSZ-13 using DFT and ab initio calculations. Catalysis Science & Technology, 11(11), 3826–3833. doi:10.1039/d1cy00433f

86. Xu, S., Zheng, A., Wei, Y., Chen, J., Li, J., Chu, Y., Zhang, M., Wang, Q., Zhou, Y., Wang, J., Deng, F., & Liu, Z. (2013). Direct Observation of Cyclic Carbenium Ions and Their Role in the Catalytic Cycle of the Methanol-to-Olefin Reaction over Chabazite Zeolites. Angewandte Chemie International Edition, 52(44), 11564–11568. doi:10.1002/anie.201303586

87. Olsbye, U., Svelle, S., Bjørgen, M., Beato, P., Janssens, T. V. W., Joensen, F., Bordiga, S., & Lillerud, K. P. (2012). Conversion of Methanol to Hydrocarbons: How Zeolite Cavity and Pore Size Controls Product Selectivity. Angewandte Chemie International Edition, 51(24), 5810–5831. doi:10.1002/anie.201103657

88. Bjorgen, M., Svelle, S., Joensen, F., Nerlov, J., Kolboe, S., Bonino, F., Palumbo, L., Bordiga, S., & Olsbye, U. (2007). Conversion of methanol to hydrocarbons over zeolite H-ZSM-5: On the origin of the olefinic species. Journal of Catalysis, 249(2), 195–207. doi: 10.1016/j.jcat.2007.04.006

89. Schmidt, F., Hoffmann, C., Giordanino, F., Bordiga, S., Simon, P., Carrillo-Cabrera, W., & Kaskel, S. (2013). Coke location in microporous and hierarchical ZSM-5 and the impact on the MTH reaction. Journal of Catalysis, 307, 238–245. doi:10.1016/j.jcat.2013.07.020

90. Rodríguez-González, L., Hermes, F., Bertmer, M., Rodríguez-Castellón, E., Jiménez-López, A., & Simon, U. (2007). The acid properties of H-ZSM-5 as studied by NH3-TPD and ^{27}Al-MAS-NMR spectroscopy. Applied Catalysis A: General, 328(2), 174–182. doi:10.1016/j.apcata.2007.06.003

91. Al-Dughaither, A. S., & de Lasa, H. (2014). HZSM-5 Zeolites with Different SiO2/Al2O3Ratios. Characterization and NH_3 Desorption Kinetics. Industrial & Engineering Chemistry Research, 53(40), 15303–15316. doi:10.1021/ie4039532

92. Abdelrahman, O. A., Vinter, K. P., Ren, L., Xu, D., Gorte, R. J., Tsapatsis, M., & Dauenhauer, P. J. (2017). Simple quantification of zeolite acid site density by reactive gas chromatography. Catalysis Science & Technology, 7(17), 3831–3841. doi:10.1039/c7cy01068k

93. Puértolas, B., Veses, A., Callén, M. S., Mitchell, S., García, T., & Pérez-Ramírez, J. (2015). Porosity-Acidity Interplay in Hierarchical ZSM-5 Zeolites for Pyrolysis Oil Valorization to Aromatics. ChemSusChem, 8(19), 3283–3293. doi:10.1002/cssc.201500685

94. Castellanos-Beltran, I. J., Assima, G. P., & Lavoie, J.-M. (2018). Effect of temperature in the conversion of methanol to olefins (MTO) using an extruded SAPO-34 catalyst. Frontiers of Chemical Science and Engineering, 12(2), 226–238. doi:10.1007/s11705-018-1709-8

95. Wang, Y., Chen, S.-L., Jiang, Y.-J., Cao, Y.-Q., Chen, F., Chang, W.-K., & Gao, Y.-L. (2016). Influence of template content on selective synthesis of SAPO-18, SAPO-18/34 intergrowth and SAPO-34 molecular sieves used for methanol-to-olefins process. RSC Advances, 6(107), 104985–104994. doi:10.1039/c6ra23048b

96. Zhao, Xingling; Xu, Jun; Deng, Feng (2020). Solid-state NMR for metal-containing zeolites: From active sites to reaction mechanism. Frontiers of Chemical Science and Engineering.. doi:10.1007/s11705-019-1885-1

97. Kianfar, E. (2019). Comparison and assessment of zeolite catalysts performance dimethyl ether and light olefins production through methanol: a review. Reviews in Inorganic Chemistry, 39(3), 157–177. doi:10.1515/revic-2019-0001

98. Bailleul, S., Yarulina, I., Hoffman, A. E. J., Dokania, A., Abou-Hamad, E., Chowdhury, A. D., Pieters, G., Hajek, J., De Wispelaere, K., Waroquier, M., Gascon, J., & Van Speybroeck, V. (2019). A Supramolecular View on the Cooperative Role of Brønsted and Lewis Acid Sites in Zeolites for Methanol Conversion. Journal of the American Chemical Society, 141(37), 14823–14842. doi:10.1021/jacs.9b07484

99. Aranzabal, A., González-Marcos, J. A., Romero-Sáez, M., González-Velasco, J. R., Guillemot, M., & Magnoux, P. (2009). Stability of protonic zeolites in the catalytic oxidation of chlorinated VOCs (1,2-dichloroethane). Applied Catalysis B: Environmental, 88(3–4), 533–541. doi:10.1016/j.apcatb.2008.10.007

100. Ma, J., Si, Z., Wu, X., Weng, D., & Ma, Y. (2016). Optimizing the crystallinity and acidity of H-SAPO-34 by fluoride for synthesizing Cu/SAPO-34 NH3-SCR catalyst. Journal of Environmental Sciences, 41, 244–251. doi:10.1016/j.jes.2015.05.024

101. Hu, S., Shan, J., Zhang, Q., Wang, Y., Liu, Y., Gong, Y., Wu, Z., & Dou, T. (2012). Selective formation of propylene from methanol over high-silica nanosheets of MFI zeolite. Applied Catalysis A: General, 445–446, 215–220. doi:10.1016/j.apcata.2012.08.032

102. Chen, X., Jiang, R., Hou, H., Zhou, Z., & Wang, X. (2020). Synthesis of ZSM-5/SAPO-34 zeolite composites from LAPONITE® and their catalytic properties in the MTO reaction. CrystEngComm, 22(37), 6182–6188. doi:10.1039/d0ce01002b

103. Wang, M., Wang, Z., Liu, S., Gao, R., Cheng, K., Zhang, L., Zhang, G., Min, X., Kang, J., Zhang, Q., & Wang, Y. (2021). Synthesis of hierarchical SAPO-34 to improve the catalytic performance of bifunctional catalysts for syngas-to-olefins reactions. Journal of Catalysis, 394, 181–192. doi:10.1016/j.jcat.2020.08.020

104. Lesthaeghe, D., De Sterck, B., Van Speybroeck, V., Marin, G. B., & Waroquier, M. (2007). Zeolite Shape-Selectivity in thegem-Methylation of Aromatic Hydrocarbons. Angewandte Chemie International Edition, 46(8), 1311–1314. doi:10.1002/anie.200604309

105. "ZSM-22 - Microporous Molecular Sieve." ACS MATERIAL, www.acsmaterial.com/zsm-22.html (consulted in 2/06/2021).

106. Teketel, S., Svelle, S., Lillerud, K.-P., & Olsbye, U. (2009). Shape-Selective Conversion of Methanol to Hydrocarbons Over 10-Ring Unidirectional-Channel Acidic H-ZSM-22. ChemCatChem, 1(1), 78–81. doi:10.1002/cctc.200900057

107. Li, J., Wei, Y., Qi, Y., Tian, P., Li, B., He, Y., Chang, F., Sun, X., & Liu, Z. (2011). Conversion of methanol over H-ZSM-22: The reaction mechanism and deactivation. Catalysis Today, 164(1), 288–292. doi: 10.1016/j.cattod.2010.10.095

108. Hereijgers, B. P. C., Bleken, F., Nilsen, M. H., Svelle, S., Lillerud, K.-P., Bjørgen, M., Weckhuysen, B. M., & Olsbye, U. (2009). Product shape selectivity dominates the Methanol-to-Olefins (MTO) reaction over H-SAPO-34 catalysts. Journal of Catalysis, 264(1), 77–87. doi: 10.1016/j.jcat.2009.03.009

109. Ibáñez, M.; Pérez-Uriarte, P.; Sánchez-Contador, M.; Cordero-Lanzac, T.; Aguayo, A.T.; Bilbao, J.; Castaño, P. (2017). Nature and Location of Carbonaceous Species in a Composite HZSM-5 Zeolite Catalyst during the Conversion of Dimethyl Ether into Light Olefins. Catalysts 2017, 7, 254. doi: 10.3390/catal7090254

110. Xianyong Sun. (2013). Catalytic Conversion of Methanol to Olefins over HZSM-5 Catalysts. Thesis to achieve Complete imprint of the from the Faculty of Chemistry at the Technical University of Munich (Germany) to obtain the academic degree of Doctor of Natural Sciences (Dr. rer. Nat.) (2013).

111. Gayubo, A. G., Aguayo, A. T., Morán, A. L., Olazar, M., & Bilbao, J. (2002). Role of water in the kinetic modeling of catalyst deactivation in the MTG process. AIChE Journal, 48(7), 1561–1571. doi:10.1002/aic.690480718

112. Ilias, S., Khare, R., Malek, A., & Bhan, A. (2013). A descriptor for the relative propagation of the aromatic- and olefin-based cycles in methanol-to-hydrocarbons conversion on H-ZSM-5. Journal of Catalysis, 303, 135–140. doi:10.1016/j.jcat.2013.03.021

113. Zhang, M., Xu, S., Wei, Y., Li, J., Wang, J., Zhang, W., Gao, S., & Liu, Z. (2016). Changing the balance of the MTO reaction dual-cycle mechanism: Reactions over ZSM-5 with varying contact times. Chinese Journal of Catalysis, 37(8), 1413–1422. doi:10.1016/s1872-2067(16)62466-x

114. Losch, P., Boltz, M., Louis, B., Chavan, S., & Olsbye, U. (2015). Catalyst optimization for enhanced propylene formation in the methanol-to-olefins reaction. Comptes Rendus Chimie, 18(3), 330–335. doi:10.1016/j.crci.2014.06.007

115. Wang, S., Chen, Y., Wei, Z., Qin, Z., Ma, H., Dong, M., Li, J., Fan, W., & Wang, J. (2015). Polymethylbenzene or Alkene Cycle? Theoretical Study on Their Contribution to the Process of Methanol to Olefins over H-ZSM-5 Zeolite. The Journal of Physical Chemistry C, 119(51), 28482–28498. doi:10.1021/acs.jpcc.5b10299

116. H. U., H., A. A., J., T. J., S., A. A., A., N. A. A., F., I., H., & M. S., A. (2019). Effect of ZSM-5 Acidity in Enhancement of Methanol-to-Olefins Process. Journal of Energy and Safety Technology (JEST), 2(1). doi:10.11113/jest.v2n1.37

117. Khare, R., Liu, Z., Han, Y., & Bhan, A. (2017). A mechanistic basis for the effect of aluminum content on ethene selectivity in methanol-to-hydrocarbons conversion on HZSM-5. Journal of Catalysis, 348, 300–305. doi:10.1016/j.jcat.2017.02.022

118. Huang, H., Zhu, H., Zhang, S., Zhang, Q., & Li, C. (2019). Effect of silicon to aluminum ratio on the selectivity to propene in methanol conversion over H-ZSM-5 zeolites. Journal of Fuel Chemistry and Technology, 47(1), 74–82. doi:10.1016/s1872-5813(19)30005-2

119. Feng, R., Yan, X., Hu, X., Wu, J., & Yan, Z. (2020). Direct synthesis of b-axis oriented H-form ZSM-5 zeolites with an enhanced performance in the methanol to propylene reaction. Microporous and Mesoporous Materials, 302, 110246. doi:10.1016/j.micromeso.2020.110246

120. Sazama, P., Dedecek, J., Gabova, V., Wichterlova, B., Spoto, G., & Bordiga, S. (2008). Effect of aluminium distribution in the framework of ZSM-5 on hydrocarbon transformation. Cracking of 1-butene. Journal of Catalysis, 254(2), 180–189. doi:10.1016/j.jcat.2007.12.005

121. Liang, T., Chen, J., Qin, Z., Li, J., Wang, P., Wang, S., Wang, G., Dong, M., Fan, W., & Wang, J. (2016). Conversion of Methanol to Olefins over H-ZSM-5 Zeolite: Reaction Pathway Is Related to the Framework Aluminum Siting. ACS Catalysis, 6(11), 7311–7325. doi:10.1021/acscatal.6b01771

122. Gorzin, F., & Yaripour, F. (2018). Production of light olefins from methanol over modified H-ZSM-5: effect of metal impregnation in high-silica zeolite on product distribution. Research on Chemical Intermediates, 45(2), 261–285. doi:10.1007/s11164-018-3601-z

123. Chen, C., Zhang, Q., Meng, Z., Li, C., & Shan, H. (2015). Effect of magnesium modification over H-ZSM-5 in methanol to propylene reaction. Applied Petrochemical Research, 5(4), 277–284. doi:10.1007/s13203-015-0129-7

124. Zhang, S., Zhang, B., Gao, Z., & Han, Y. (2010). Ca modified ZSM-5 for high propylene selectivity from methanol. Reaction Kinetics, Mechanisms and Catalysis. doi:10.1007/s11144-009-0131-0

125. Mohammadrezaei, A., Papari, S., Asadi, M., Naderifar, A., & Golhosseini, R. (2012). Methanol to propylene: the effect of iridium and iron incorporation on the HZSM-5 catalyst. Frontiers of Chemical Science and Engineering, 6(3), 253–258. doi:10.1007/s11705-012-0902-4

126. Valecillos, José; Epelde, Eva; Albo, Jonathan; Aguayo, Andrés T.; Bilbao, Javier; Castaño, Pedro (2019). Slowing down the deactivation of H-ZSM-5 zeolite catalyst in the methanol-to-olefin (MTO) reaction by P or Zn modifications. Catalysis Today, 348, 243–256. doi:10.1016/j.cattod.2019.07.059

127. Liu, B., France, L., Wu, C., Jiang, Z., Kuznetsov, V. L., Al-Megren, H. A., Al-Kinany, M., Aldrees, S. A., Xiao, T., & Edwards, P. P. (2015). Methanol-to-hydrocarbons conversion over MoO3/H-ZSM-5 catalysts prepared via lower temperature calcination: a route to tailor the distribution and evolution of promoter Mo species, and their corresponding catalytic properties. Chemical Science, 6(9), 5152–5163. doi:10.1039/c5sc01825k

128. Wang, X., Meng, F., Chen, H., Gao, F., Wang, Y., Han, X., Fan, C., Sun, C., Wang, S., & Wang, L. (2017). Synthesis of a hierarchical ZSM-11/5 composite zeolite of high SiO 2 /Al 2 O 3 ratio and catalytic performance in the methanol-to-olefins reaction. Comptes Rendus Chimie, 20(11–12), 1083–1092. doi:10.1016/j.crci.2017.10.004

129. Dugkhuntod, P., & Wattanakit, C. (2020). A Comprehensive Review of the Applications of Hierarchical Zeolite Nanosheets and Nanoparticle Assemblies in Light Olefin Production. Catalysts, 10(2), 245. doi:10.3390/catal10020245

130. Weissenberger, T., Machoke, A. G. F., Bauer, J., Dotzel, R., Casci, J. L., Hartmann, M., & Schwieger, W. (2020). Hierarchical ZSM-5 Catalysts: The Effect of Different Intracrystalline Pore Dimensions on Catalyst Deactivation Behaviour in the MTO Reaction. ChemCatChem, 12(9), 2461–2468. doi:10.1002/cctc.201902362

131. Bernardo Pessanha. (2019). A Steady State Study: Effect of Zeolite and Operating Conditions on Methanol-to-Olefins. Thesis to obtain the Master of Science Degree in Chemical Engineering. Instituto Superior Técnico (IST, UL), Portugal.

132. Marie-Elisabeth Lissens (2021). Unpublished work. Universiteit Gent (UGent), Belgium.

133. Tingjun Lei. (2020). On Reaching Steady-State in Methanol-To-Olefins Experimentation: Effect of Hydrocarbon Pool Species. Master's dissertation submitted in order to obtain the academic degree of Master of Science in Chemical Engineering. Universiteit Gent (UGent), Belgium.

134. Zahara, Z., Krisnandi, Y. K., Wibowo, W., Nurani, D. A., Rahayu, D. U. C., & Haerudin, H. (2018). Synthesis and characterization of hierarchical ZSM-5 zeolite using various templates as cracking catalysts. Proceedings Of The 3rd International Symposium On Current Progress In Mathematics And Sciences 2017 (Iscpms2017). doi:10.1063/1.5064085

135. "Nano H-ZSM-5." ACS MATERIAL, ACS MATERIAL, www.acsmaterial.com/nano-zsm-5.html (consulted in 4/07/2021).

136. Abbasian, S., Taghizadeh, M. (2014). Preparation of H-ZSM-5 Nano-Zeolite Using Mixed Template Method and its Activity Evaluation for ethanol to DME Reaction. International Journal of Nanoscience and Nanotechnology, 10(3), 171-180.

137. "Gas Chromatography (GC) with Flame-Ionization Detection." JoVE Science Education (source: Laboratory of Dr. B. Jill Venton - University of Virginia), JoVE, www.jove.com/v/10187/gas-chromatography-gc-with-flame-ionization-detection (consulted in 4/07/2021).

138. Peak Scientific. "How Does an FID Work?" Peak Scientific, Peak Scientific, 28 Nov. 2019, www.peakscientific.com/discover/news/how-does-an-fid-work/ (consulted in 4/07/2021).

139. Dietz, W. A. (1967). Response Factors for Gas Chromatographic Analyses. Journal of Chromatographic Science, 5(2), 68–71. doi:10.1093/chromsci/5.2.68

140. EUROKIN Spreadsheet For Assessment Of Transport Limitations In Gas-Solid Fixed Beds. http://www.eurokin.org/wp-content/uploads/webtool/EUROKIN_fixed-bed_html.htm (last accessed August 29, 2021).

141. EUROKIN (2012). EUROKIN spreadsheet on requirements for measurement of intrinsic kinetics in the gas-solid fixed-bed reactor. Background information on the spreadsheet EUROKIN_fixed-bed_html developed for the assessment of transport limitations requirements for measurement of intrinsic kinetics in the gas-solid fixed-bed reactor.

142. Fernández-Sánchez, M. L. (2018). Optical Atomic Emission Spectrometry—Inductively Coupled Plasma. In Reference Module in Chemistry, Molecular Sciences and Chemical Engineering. Elsevier. doi:10.1016/b978-0-12-409547-2.14542-1

143. Pramanik, S., & Das, P. (2019). Metal-Based Nanomaterials and Their Polymer Nanocomposites. In Nanomaterials and Polymer Nanocomposites (pp. 91–121). Elsevier. doi:10.1016/b978-0-12-814615-6.00003-5

144. "ZSM-5." Zeolyst International, Zeolyst, www.zeolyst.com/our-products/standard-zeolite-powders/zsm-5.html (consulted in 4/07/2021)

145. Reis Bernardes, F., Jakeline Cunha Rezende, M., de Oliveira Rodrigues, V., Sandra Veiga Nascimento, R., & Pereira da Silva Ribeiro, S. (2019). Synthesis and Application of H-ZSM-5 Zeolites with Different Levels of Acidity as Synergistic Agents in Flame Retardant Polymeric Materials. Polymers, 11(12), 2110. doi:10.3390/polym11122110

146. "X-Ray Powder Diffraction (XRD)." Geochemical Instrumentation and Analysis, SERC. www.serc.carleton.edu/research_education/geochemsheets/techniques/XRD.html (consulted in 07/07/2021)

147. Heiney, Paul A. XRD Basics, Physics Upenn, www.physics.upenn.edu/~heiney/datasqueeze/basics.html (consulted in 17/07/2021)

148. "Diffraction Basics." Chemical Instrumentation Facility, Iowa State University, www.cif.iastate.edu/services/acide/xrd-tutorial/xrd (consulted in 07/07/2021)

149. "ZSM-5." ACS Material Store, ACS Materia, www.acsmaterial.com/blog-detail/zsm-5-molecular-seive.html (consulted in July, 2021)

150. Peng, P., Wang, Y., Rood, M. J., Zhang, Z., Subhan, F., Yan, Z., Qin, L., Zhang, Z., Zhang, Z., & Gao, X. (2015). Effects of dissolution alkalinity and self-assembly on ZSM-5-based micro-/mesoporous composites: a study of the relationship between porosity, acidity, and catalytic performance. CrystEngComm, 17(20), 3820–3828. doi: 10.1039/c5ce00384a

151. Krisnandi, Y. K., Samodro, B. A., Sihombing, R., & Howe, R. F. (2015). Direct Synthesis of Methanol by Partial Oxidation of Methane with Oxygen over Cobalt Modified Mesoporous H-ZSM-5 Catalyst. Indonesian Journal of Chemistry, 15(3), 263–268. doi:10.22146/ijc.21194

152. Sotomayor, Francisco & Cychosz, Katie & Thommes, Matthias. (2018). Characterization of Micro/Mesoporous Materials by Physisorption: Concepts and Case Studies.

153. Thommes, M., Kaneko, K., Neimark, A. V., Olivier, J. P., Rodriguez-Reinoso, F., Rouquerol, J., & Sing, K. S. W. (2015). Physisorption of gases, with special reference to the evaluation of surface area and pore size distribution (IUPAC Technical Report). Pure and Applied Chemistry, 87(9–10), 1051–1069. doi:10.1515/pac-2014-1117A

154. Khalfaoui, M., Knani, S., Hachicha, M. A., & Lamine, A. B. (2003). New theoretical expressions for the five adsorption type isotherms classified by BET based on statistical physics treatment. Journal of Colloid and Interface Science, 263(2), 350–356. doi:10.1016/s0021-9797(03)00139-5

155. Zelenka, T. (2016). Adsorption and desorption of nitrogen at 77 K on micro- and meso- porous materials: Study of transport kinetics. Microporous and Mesoporous Materials, 227, 202–209. doi:10.1016/j.micromeso.2016.03.009

156. Sing, K. S. W., & Williams, R. T. (2004). Physisorption Hysteresis Loops and the Characterization of Nanoporous Materials. Adsorption Science & Technology, 22(10), 773–782. doi:10.1260/0263617053499032

157. Thommes, M. (2010). Physical Adsorption Characterization of Nanoporous Materials. Chemie Ingenieur Technik, 82(7), 1059–1073. doi:10.1002/cite.201000064

158. Belskaya, Olga B.; Danilova, Irina G.; Kazakov, Maxim O.; Mironenko, Roman M.; Lavrenov, Alexander V.; Likholobov, Vladimir A. (2013). ChemInform Abstract: FTIR Spectroscopy of Adsorbed Probe Molecules for Analyzing the Surface Properties of Supported Pt (Pd) Catalysts. ChemInform, 44(51), doi:10.1002/chin.201351237

159. Zholobenko, Vladimir; Freitas, CÃ¡tia; Jendrlin, Martin; Bazin, Philippe; Travert, Arnaud; Thibault-Starzyk, Frederic (2020). Probing the acid sites of zeolites with pyridine: Quantitative AGIR measurements of the molar absorption coefficients. Journal of Catalysis, 385(), 52–60. doi:10.1016/j.jcat.2020.03.003

160. S. Bordiga; C. Lamberti; F. Bonino; A. Travert; F. Thibault-starzyk (2015). Probing zeolites by vibrational spectroscopies. Chem. Soc. Rev., 2015,44, 7262-7341. doi:10.1039/C5CS00396B

161. Weber, C D; Bradley, C; Lonergan, M C (2014). Solution phase n-doping of C60 and PCBM using tetrabutylammonium fluoride. Journal of Materials Chemistry, 2(2), 303–.doi:10.1039/x0xx00000x

162. Gabrienko, Anton A.; Danilova, Irina G.; Arzumanov, Sergei S.; Pirutko, Larisa V.; Freude, Dieter; Stepanov, Alexander G. (2018). Direct Measurement of Zeolite Brønsted Acidity by FTIR Spectroscopy: Solid-State ^{1}H MAS NMR Approach for Reliable Determination of the Integrated Molar Absorption Coefficients. J. Phys. Chem. C 2018, 122, 44, 25386–25395. doi:10.1021/acs.jpcc.8b07429

163. Newland, Stephanie H.; Sinkler, Wharton; Mezza, Thomas; Bare, Simon R.; Raja, Robert (2016). Influence of dopant substitution mechanism on catalytic properties within hierarchical architectures. Proceedings of the Royal Society A: Mathematical, Physical and Engineering Science, 472(2191), 20160095–.doi:10.1098/rspa.2016.0095

164. Fang Jin; Yongdan Li (2009). A FTIR and TPD examination of the distributive properties of acid sites on ZSM-5 zeolite with pyridine as a probe molecule. Catalysis Today 145(1-2), 101–107. doi:10.1016/j.cattod.2008.06.007

165. Anton A. Gabrienko; Irina G. Danilova; Sergei S. Arzumanov; Alexander V. Toktarev; Dieter Freude; Alexander G. Stepanov (2010). Strong acidity of silanol groups of zeolite beta: Evidence from the studies by IR spectroscopy of adsorbed CO and ^{1}H MAS NMR. Microporous and Mesoporous Materials 131(1-3), 210–216. doi:10.1016/j.micromeso.2009.12.025

166. Zambare, Abhay Suresh; Ou, John; Hill Wong, David Shan; Yao, Ching-Wen; Jang, Shi-Shang (2019). Controlling the product selectivity in the conversion of methanol to the feedstock for phenol production. RSC Advances, 9(41), 23864–23875. doi:10.1039/c9ra03723c

167. Barzetti, Tommy; Selli, Elena; Moscotti, Daniele; Forni, Lucio (1996). Pyridine and ammonia as probes for FTIR analysis of solid acid catalysts. Journal of the Chemical Society, Faraday Transactions, 92(8), 1401. doi:10.1039/FT9969201401

168. Mendes, Pedro S.F.; Lapisardi, Grégory; Bouchy, Christophe; Rivallan, Mickaël; Silva, João M.; Ribeiro, M. Filipa (2015). Hydrogenating activity of Pt/zeolite catalysts focusing acid support and metal dispersion influence. Applied Catalysis A: General, 504(), 17-28. doi:10.1016/j.apcata.2015.03.027

169. Popova, M.; Szegedi, Á.; Oykova, M.; Lazarova, H.; Koseva, N.; Mihályi, M.R.; Shestakova, P. Selective Production of Phenol on Bifunctional, Hierarchical ZSM-5 Zeolites. Molecules 2021, 26, 3576. doi:10.3390/molecules26123576

170. Wu, Weiqiang; Weitz, Eric (2014). Modification of acid sites in ZSM-5 by ion-exchange: An in-situ FTIR study. Applied Surface Science, 316(), 405–415. doi:10.1016/j.apsusc.2014.07.194

171. Hartanto, Djoko; Sin Yuan, Lai; Mutia Sari, Sestriana; Sugiarso, Djarot; Kris Murwarni, Irmina; Ersam, Taslim; Prasetyoko, Didik; Nur, Hadi (2016). The Use Of The Combination Of Ftir, Pyridine Adsorption, ^{27}Al and ^{29}Si MAS NMR To Determine The Brönsted And Lewis Acidic Sites. Jurnal Teknologi, 78(6). doi:10.11113/jt.v78.8821

172. C.A. Emeis (1993). Determination of Integrated Molar Extinction Coefficients for Infrared Absorption Bands of Pyridine Adsorbed on Solid Acid Catalysts. , 141(2), 347–354. doi:10.1006/jcat.1993.1145

173. Omojola, T., Cherkasov, N., McNab, A.I. et al. Mechanistic Insights into the Desorption of Methanol and Dimethyl Ether Over ZSM-5 Catalysts. Catal Lett 148, 474–488 (2018). doi:10.1007/s10562-017-2249-4

174. Schroeder, Christian; Siozios, Vassilios; Hunger, Michael; Hansen, Michael Ryan; Koller, Hubert (2020). Disentangling BrÃ¸nsted Acid Sites and Hydrogen-Bonded Silanol Groups in High-Silica Zeolite H-ZSM-5. J. Phys. Chem. C 2020, 124, 42, 23380–23386. doi:10.1021/acs.jpcc.0c06113

175. Luz Rodríguez-González; Florian Hermes; Marko Bertmer; Enrique Rodríguez-Castellón; Antonio Jiménez-López; Ulrich Simon (2007). The acid properties of H-ZSM-5 as studied by NH3-TPD and ^{27}Al-MAS-NMR spectroscopy. , 328(2), 174–182.doi:10.1016/j.apcata.2007.06.003

176. Epelde, Eva; Santos, José I.; Florian, Pierre; Aguayo, Andrés T.; Gayubo, Ana G.; Bilbao, Javier; Castaño, Pedro (2015). Controlling coke deactivation and crackig selectivity of MFI zeolite by H3PO4 or KOH modification. Applied Catalysis A: General 505. doi:10.1016/j.apcata.2015.07.022

177. Phung, Thanh Khoa; Busca, Guido (2014). On the Lewis acidity of protonic zeolites. Applied Catalysis A: General, (2014). doi:10.1016/j.apcata.2014.11.031

178. Petr Sazama; Blanka Wichterlova; Jiri Dedecek; Zdenka Tvaruzkova; Zuzana Musilova; Luisa Palumbo; Stepan Sklenak; Olga Gonsiorova (2011). FTIR and ^{27}Al MAS NMR analysis of the effect of framework Al- and Si-defects in micro- and micro-mesoporous H-ZSM-5 on conversion of methanol to hydrocarbons. Microporous and Mesoporous Materials, 143(1), 87–96. doi:10.1016/j.micromeso.2011.02.013

179. Palcic, Ana; Ordomsky, Vitaly V.; Qin, Zhengxing; Georgieva, Veselina; Valtchev, Valentin (2018). Tuning zeolite properties for highly efficient synthesis of propylene from methanol. Chemistry - A European Journal 24(50). doi:10.1002/chem.201803136

180. Losch, Pit; Hoff, Thomas; Kolb, Joy; Bernardon, Claire; Tessonnier, Jean-Philippe; Louis, Benoît (2017). Mesoporous ZSM-5 Zeolites in Acid Catalysis: Top-Down vs. Bottom-Up Approach. Catalysts, 7(8), 225. doi:10.3390/catal7080225

181. Ravinayagam, Vijaya; Rabindran Jermy, B. (2018). Fabricating hierarchical ZSM-5 to induct long chain antioxidant coenzyme Q10 for biomedical application. Journal of Saudi Chemical Society, 461-476.doi:10.1016/j.jscs.2018.09.001

182. Meng, Xiaojing; Zhang, Minxiu; Chen, Chunlin; Li, Chunyi; Xiong, Wei; Li, Min (2018). Insights into the role of silanols in methanol to propene reaction over silicalite-2 zeolite through post-treatments. Applied Catalysis A: General, 558(), 122–130. doi:10.1016/j.apcata.2018.04.001

183. Wang, S., Wang, J., Jia, Y., Ding, C., Gao, P., Li, Y., … Meng, Y. (2021). Tandem catalysts for the conversion of methanol to aromatics with excellent selectivity and stability. New Journal of Chemistry, 45(18), 7999–8007.doi:10.1039/d1nj00592h

184. Jia, Yanming; Wang, Junwen; Zhang, Kan; Feng, Wei; Liu, Shibin; Ding, Chuanmin; Liu, Ping (2017). Nanocrystallite self-assembled hierarchical ZSM-5 zeolite microsphere for methanol to aromatics. Microporous and Mesoporous Materials, 247, 103–115.doi:10.1016/j.micromeso.2017.03.035

185. Li, T., Shoinkhorova, T., Gascon, J., & Ruiz-Martínez, J. (2021). Aromatics Production via Methanol-Mediated Transformation Routes. ACS Catalysis, 11(13), 7780–7819.doi:10.1021/acscatal.1c01422

186. Lin, S., Zhi, Y., Chen, W., Li, H., Zhang, W., Lou, C., … Liu, Z. (2021). Molecular Routes of Dynamic Autocatalysis for Methanol-to-Hydrocarbons Reaction. Journal of the American Chemical Society, 143(31), 12038–12052.doi:10.1021/jacs.1c03475

187. Róbert Barthos; Tamás Bánsági; Tímea Süli Zakar; Frigyes Solymosi (2007). Aromatization of methanol and methylation of benzene over Mo2C/ZSM-5 catalysts. Journal of Catalysis 247 (2007) 368–378. doi:10.1016/j.jcat.2007.02.017

188. Lezcano Castillo, Gontzal. (2018). Kinetic modelling of the dimethyl ether to olefins reaction over a HZSM-5 based catalyst. Thesis to obtain the Bachelor's degree in Chemical Engineering. Universidad del País Vasco.

189. Van Speybroeck, Veronique; De Wispelaere, Kristof; Van der Mynsbrugge, Jeroen; Vandichel, Matthias; Hemelsoet, Karen; Waroquier, Michel (2014). First principle chemical kinetics in zeolites: the methanol-to-olefin process as a case study. Chem. Soc. Rev., 43(21), 7326–7357. doi:10.1039/C4CS00146J

190. Stian Svelle; Per Ola Rønning; Unni Olsbye; Stein Kolboe (2005). Kinetic studies of zeolite-catalyzed methylation reactions. Part 2. Co-reaction of [12C]propene or [12C]n-butene and [13C]methanol. , 234(2), 385–400.doi:10.1016/j.jcat.2005.06.028

191. Hu, Min; Wang, Chao; Gao, Xiuzhi; Chu, Yueying; Qi, Guodong; Wang, Qiang; Xu, Guangtong; Xu, Jun; Deng, Feng (2020). Establishing a Link Between the Dual Cycles in Methanol-to-Olefins Conversion on H-ZSM-5: Aromatization of Cycloalkenes. ACS Catalysis, (), 4299–4305.doi:10.1021/acscatal.0c00838

Annex

Annex A – Procedures and Fundamentals

Annex A1 – High-Throughput Kinetic Setup

Feed Section

The feeding section is composed of both gas and liquid feeding.

There can be found three different gas feeding sections for each reactor, associated with different thermal mass flow controllers (Bronkhorst ®). These originate from the common high-pressure lines: nitrogen, hydrogen, and methane. In this experimental setting, nitrogen is used as a diluent gas and its flow is adjusted to maintain the reactant's partial pressure throughout all experiments.

The liquid feeding (methanol) is stored in a glass vessel connected to a metering liquid pump (2LMP by Eldex Laboratories) which supplies the feed for both reactor systems. After this pump there can be found a pressurized four-way connection that divides the feed in three parts: two connect to the reaction zone lines and the other recycles part of the pumped liquid back to the glass vessel. The amount of feed that goes through the first two lines is regulated by a mass flow controller located after the parting of the common line and regulated by the input on the software, whereas the recycling rate is regulated by the pressure in the four-way connection by a needle valve (most preferably between 20-50 bar). The liquid stream then follows to the common line together with the gas feed to the reactor.

In **table 7** is presented the scale of operation for the liquid and gas feeds according to the mechanical limitations of the equipment and calibration.

Table 7 – Feed section limitations for gas and liquid flowrates.

Liquid feed flow rate (g/h)		Gas feed flow rate (NL/h)	
MeOH	1-50	N_2	100-1000
		H_2	10-100
		CH_4	10-100

Reactor block

The two parallel tubular reactors are contained in a heating block with a common heating oven (IR-oven) at the bottom that heats the reactor's effluent up to 140º C. Each tubular reactor (780 x 11 mm) is equipped with an internal thermocouple with 3 mm of diameter. The temperature controlled by the software is evaluated by an external thermocouple which measures three equally

parted sections along the reactor's length. The catalyst bed loading considers the intrinsic kinetics of each experiment and should not have loads higher than 10 g (catalyst and inert). The filling of the reactor uses spherical particles from 2-5 mm and 1-2 mm near the catalyst bed.

The reaction conditions ensure a constant methanol partial pressure (by adjustment of nitrogen flow rate) and by changing the amount of catalyst load and methanol flow rate and catalyst load different space-times were studied, aiming for conversions lower than 70% as to acquire reliable kinetic data without the effect of catalyst deactivation. The range of operating conditions studied can be found in **table 8**.

Table 8 – Experimental conditions summary used during MTO catalytic studies.

Temperature (º C)	300 - 450
Total pressure (bar)	3.5
Methanol partial pressure (bar)	0.4
Space time, W/F ($kg_{cat}.s/mol_{MeOH}$)	0.5 - 110.0

The initiation of every experimental campaign starts with the pressure/leak test at 5 bar and room temperature with a flow of nitrogen of 20-100 NL/h. In these conditions, a pressure drop of 1.0-1.5 bar is usually observed but decreases down to 0.5-1.0 bar once the entire system, the major reason being the requirement to have the MM membranes working properly. In addition, the temperature control is regulated by a PID controller that has been selected in the software to be controlled by the (N-type) thermocouples inside the reactor. The software input sends a feedback signal to the temperature controller which regulates the power of the electric heaters in a control loop (with a parallel safety loop).

Effluent Section

After leaving the reactor, passing through the IR-oven, the effluent lines are heated by a tracing until they reach the pressure control valve, responsible to regulate and maintain the pressure inside the reactor through backpressure. The effluent passes through the bottom part of the membrane where a flow of nitrogen (regulated by an independent system) is passed on the other end. Both the MM and all subsequent lines are also heated to maintain the effluent in the gas phase (as it remains throughout the entire process).

During this experimental period, the possibility of bypass of the effluent to the liquid flash drum was removed to reduce the number of points with possible pressure drop. At this point location, the effluent pressure decreases to atmospheric pressure. It follows a set of lines where the effluent is once again pressurized between 4-5 bar (with a valve and a needle valve) before reaching a 10-way valve (one for each reactor in the setup) and the GC. The selection of the adequate port in the 10-way valve followed by the pressurizing of the line must occur at least 15 minutes before the GC

analysis to flush the lines of other effluents. With a suitable method selected, a fraction of the sample is injected into the online GC (by Agilent Technologies) which encompasses a flame ionizing detector (FID) and an Rtx-DHA-150 column (fused silica). All the gases are continuously sent to the central ventilation during the process.

Troubleshooting

Safe to say that troubleshooting was a major component during this experimental work. Mechanical workings, organizational problems, and were responsible for about two-thirds of the experimental period.

At an initial stage of the experiments, multiple situations of complete pressure drop occurred and had to be investigated. The recurrent substitution of the MM and the MM membranes was demonstrated to be an inviable solution after several incidents. The main problem was tracked down to three intertwined elements: pressure variations in the common gas feed lines (caused by another user opening their valves, the substitution of the nitrogen bottles, or an incorrect procedure of turning off the feed). Any of these were responsible for causing a momentary surge in the nitrogen flow passing through the mass flowmeter which, due to the effluent lines between the reactor and the MM having a smaller diameter, resulted in the increase of the superficial velocity of the fluid, displacing the MM membrane. As a result, the MM membrane could no longer properly regulate the pressure.

The sudden increase in pressure in the system was also found to be responsible for the dragging of the catalyst bed (which could also be dragged potentially throughout the rest of the effluent zone). Not only the practice of turning off the valves in any potentially problematic situation was adopted, but this was also responsible for the implementation of the quartz wool layer at the bottom of the catalyst bed to act as a filter. Furthermore, contamination between streams in the effluent zone was also a major adversity.

All setup users have products in the range of C_2-C_{12} so, heavier hydrocarbons are more prone to condensate if the heating of the lines is malfunctioning or if the heating is not sufficient. Condensation in the lines may take up to 4 days to fully clean/flush which heavily delays all experimental work. In consequence, during multiple weeks the setup was only used by one user at the time. To maximize the setup usability, it was essential to find a functional, long-term, solution. Steps were taken to find the true origin of the contamination: insufficient flushing time or condensation from one of the users.

Since the contamination problems were only observed with the switching of the 10-way valve position, the rotor of the equipment was replaced as with time the alignment with the entries and the sealing may be compromised. This approach had no success in solving the problem, nor increasing the flushing of the lines between the 10-way valve and the GCs with pressurization times up to 30 minutes (which was already a completely impracticable option). A proposal was made for a bypass

of the 10-way valve for the present setup, but as it did not present a practical solution for the rest of the users, it was not adopted.

The previous lines were then changed for ones with lower length and inferior diameter, the heating tracing was replaced with one at higher temperatures and unnecessary three-way valves were removed as they present potential locations for the accumulation of condensates, which solved the problem to a satisfactory level.

Annex A3 – Intrinsic Kinetics

In order to satisfy the intrinsic kinetic boundaries, inlet flow range, dilution ratio, catalyst mass, and particle size, were adjusted. The reduction of the pressure-drop over the catalyst bed is related to the decrease of the first four parameters, whereas the internal diffusion and temperature gradient are heavily dependent on compromise in the reduction of the particle size which negatively affects the previous. As these are the hardest parameters to adjust, with emphasized challenges at higher temperatures and lower Si/Al ratios (as activity also increases), a careful study with a compromise between all of these is essential.

With respect to the previously stated, the aimed space times/conversions, and the setup limitations (catalyst loadings between 0.1-2.5 g), **table 9** depicts the loading range of catalyst particle size and inert, as well as typical catalyst mass, for each catalyst tested under intrinsic kinetics regime.

Table 9 – Catalyst bed composition with respect for intrinsic kinetic data acquisition at a given temperature.

Temperature	350	375	400	450
Si/Al = 25				
Catalyst mass (g)	0.10-0.20	0.10-0.20	0.10-0.15	
Particle size (μm)	50-100	20-70	20-70	
Inert/catalyst mass ratio	5-10	5-10	5-10	
Si/Al = 140				
Catalyst mass (g)		1.5-2.5	0.5-1.5	0.5
Particle size (μm)		200-212	150-200	100-150
Inert/catalyst mass ratio		2.5	5-7	7

EUROKIN Input Data

In **figure 57** it follows an example of the kinetic parameters used for the EUROKIN simulations of Si/Al of 140 at 375º C.

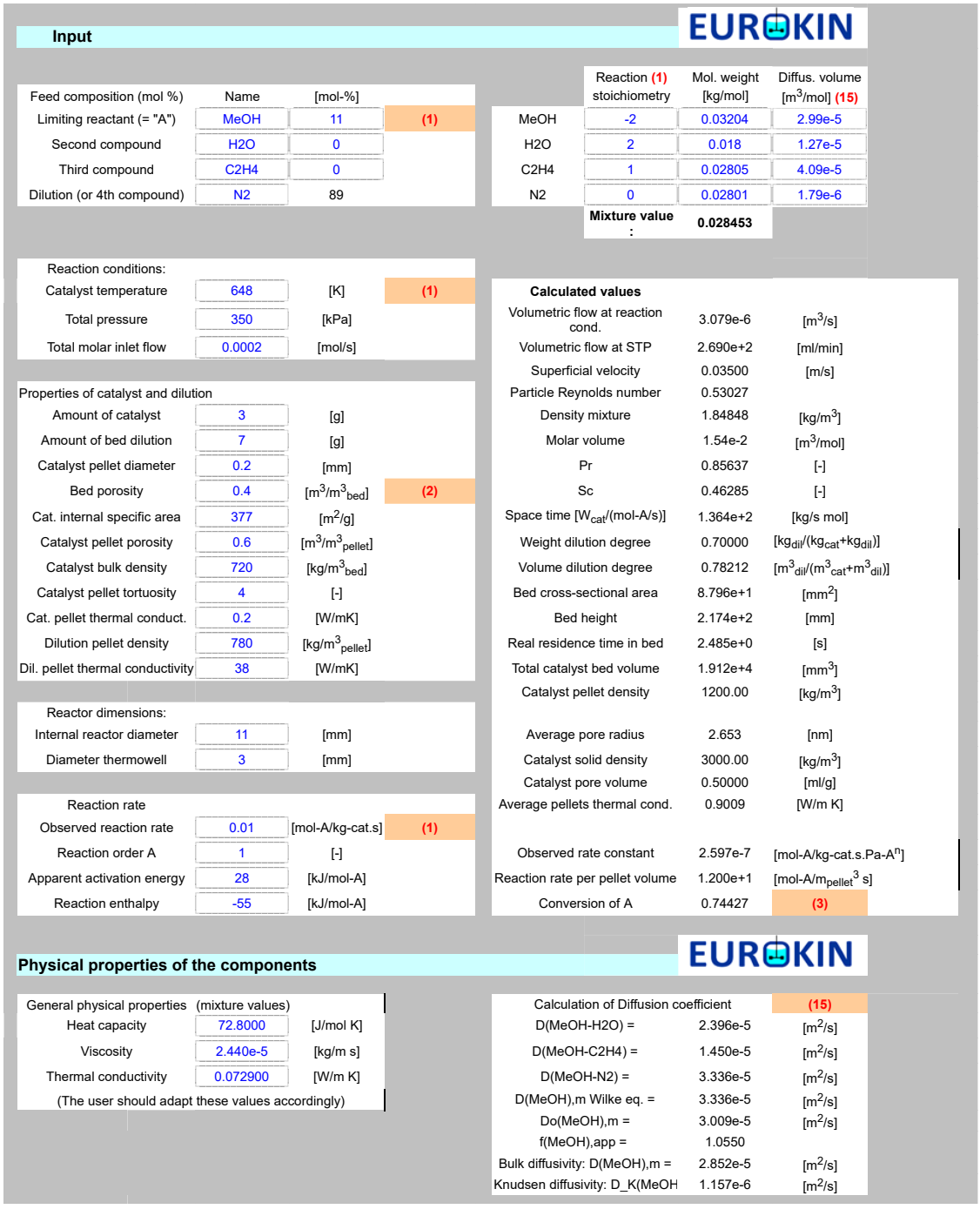

Input

Feed composition (mol %)	Name	[mol-%]	
Limiting reactant (= "A")	MeOH	11	(1)
Second compound	H2O	0	
Third compound	C2H4	0	
Dilution (or 4th compound)	N2	89	

	Reaction (1) stoichiometry	Mol. weight [kg/mol]	Diffus. volume [m^3/mol] (15)
MeOH	-2	0.03204	2.99e-5
H2O	2	0.018	1.27e-5
C2H4	1	0.02805	4.09e-5
N2	0	0.02801	1.79e-6
	Mixture value :	**0.028453**	

Reaction conditions:			
Catalyst temperature	648	[K]	(1)
Total pressure	350	[kPa]	
Total molar inlet flow	0.0002	[mol/s]	

Properties of catalyst and dilution			
Amount of catalyst	3	[g]	
Amount of bed dilution	7	[g]	
Catalyst pellet diameter	0.2	[mm]	
Bed porosity	0.4	[m^3/m^3_{bed}]	(2)
Cat. internal specific area	377	[m^2/g]	
Catalyst pellet porosity	0.6	[m^3/m^3_{pellet}]	
Catalyst bulk density	720	[kg/m^3_{bed}]	
Catalyst pellet tortuosity	4	[-]	
Cat. pellet thermal conduct.	0.2	[W/mK]	
Dilution pellet density	780	[kg/m^3_{pellet}]	
Dil. pellet thermal conductivity	38	[W/mK]	

Reactor dimensions:		
Internal reactor diameter	11	[mm]
Diameter thermowell	3	[mm]

Reaction rate			
Observed reaction rate	0.01	[mol-A/kg-cat.s]	(1)
Reaction order A	1	[-]	
Apparent activation energy	28	[kJ/mol-A]	
Reaction enthalpy	-55	[kJ/mol-A]	

Calculated values		
Volumetric flow at reaction cond.	3.079e-6	[m^3/s]
Volumetric flow at STP	2.690e+2	[ml/min]
Superficial velocity	0.03500	[m/s]
Particle Reynolds number	0.53027	
Density mixture	1.84848	[kg/m^3]
Molar volume	1.54e-2	[m^3/mol]
Pr	0.85637	[-]
Sc	0.46285	[-]
Space time [W_{cat}/(mol-A/s)]	1.364e+2	[kg/s mol]
Weight dilution degree	0.70000	[$kg_{dil}/(kg_{cat}+kg_{dil})$]
Volume dilution degree	0.78212	[$m^3_{dil}/(m^3_{cat}+m^3_{dil})$]
Bed cross-sectional area	8.796e+1	[mm^2]
Bed height	2.174e+2	[mm]
Real residence time in bed	2.485e+0	[s]
Total catalyst bed volume	1.912e+4	[mm^3]
Catalyst pellet density	1200.00	[kg/m^3]
Average pore radius	2.653	[nm]
Catalyst solid density	3000.00	[kg/m^3]
Catalyst pore volume	0.50000	[ml/g]
Average pellets thermal cond.	0.9009	[W/m K]
Observed rate constant	2.597e-7	[mol-A/kg-cat.s.Pa-A^n]
Reaction rate per pellet volume	1.200e+1	[mol-A/m^3_{pellet} s]
Conversion of A	0.74427	(3)

Physical properties of the components

General physical properties	(mixture values)	
Heat capacity	72.8000	[J/mol K]
Viscosity	2.440e-5	[kg/m s]
Thermal conductivity	0.072900	[W/m K]
(The user should adapt these values accordingly)		

Calculation of Diffusion coefficient		(15)
D(MeOH-H2O) =	2.396e-5	[m^2/s]
D(MeOH-C2H4) =	1.450e-5	[m^2/s]
D(MeOH-N2) =	3.336e-5	[m^2/s]
D(MeOH),m Wilke eq. =	3.336e-5	[m^2/s]
Do(MeOH),m =	3.009e-5	[m^2/s]
f(MeOH),app =	1.0550	
Bulk diffusivity: D(MeOH),m =	2.852e-5	[m^2/s]
Knudsen diffusivity: D_K(MeOH	1.157e-6	[m^2/s]

Figure 57 – EUROKIN spreadsheet parameters for H-ZSM-5 Si/Al of 140 simulations at 375° C, P_{MeOH}=0.4 bar, at steady-state.

Annex B – Zeolite Characterization

Annex B1 – py-FTIR Acid Density Concentrations

Py-FTIR results were obtained from 150-450º C for S25 and S40. However, the experimental results at 350º C and 450º C were not available in time for the submission of this project. Due to the difficulty in finding equivalent results in the literature, from Zeolyst or other origin, at this specific desorption temperature.

The work performed by Busca (2014) presents py-FTIR data from 150-450º C for H-ZSM-5 of Si/Al of 25 and 140 **[177]**. It results that Si/Al of 140 not only preserved approximately all of its Lewis acidity, but also best preserved it Brønsted acidity. Evidently, this results in a higher B/L ratio as well as higher strong/weak acidity. It follows the conservative hypothesis, to be use hereon, that the Si/Al of 140 preserved twice the Brønsted acidity than Si/Al of 25. This result appears correct from the structural similarities between S25 and S140 in comparison with S40.

Table 10 exhibits all the values used in the graphic representation in **Chapter 4.4.2**, during the py-FTIR acid density analysis and S140 extrapolated data.

Table 10 – Acid site concentrations obtained by py-FTIR for H-ZSM-5 of Si/Al of 25, 40 and 140 at 150º, 250º, 350º and 450º C. Comparison with literature references.

T (º C)	**150**				**250**		**350**		**450**	
n (µmol/g)	**n_{LAS}**	**n_{BAS}**	**B/L**	**n_{total}**	**B/L**	**n_{total}**	**B/L**	**n_{total}**	**B/L**	**n_{total}**
S25	**31**	**238**	**7.6**	**269**	**8.5**	**243**	**7.6**	**188**	**2.5**	**88**
	31 [a]	200 [a]	6.5c	231c						
	61 [b]	413 [b]	6.7d	474d						
	150 [c]	356 [c]	2.4e	496e						
S40	**23**	**214**	**9.1**	**238**	**9.9**	**217**	**7.7**	**178**	**0.9**	**48**
	35 [d]	232 [d]	6.6a	267a						
	61 [e]	315 [e]	5.2b	376b						
	25 [a]	114 [a]	5.7c	140c						
	80 [c]	117 [c]	1.5e	197e						
S140	**6**	**57**	**9.6**	**63**	**11.8**	**50**	**-**	**-**	**5.0 [f]**	**36 [f]**
	13 [a]	98 [a]	7.5c	111c						
	30 [c]	78 [c]	2.6	108e						

All references used the acidic from of ZSM-5 from Zeolyst International, with similar calcination methods, except when referred otherwise.

[a] **Represented as "o".** Puértolas et al. (2015) recorded at 150º C, with Emeis's extinction coefficients **[93]**.

[b] **Represented as "□".** Peng et. al. (2015) recorded at 150º C, H-ZSM-5 Si/Al=28 from Nankai Catalyst Company, with Emeis's extinction coefficients **[149]**.

[c] **Represented as "⊞".** Omojola et al. (2018) recorded at 100º C, H-ZSM-5 Si/Al=25 from Zeolyst International and H-ZSM-5 Si/Al=[36, 135] from BP Chemicals, with Emeis's extinction coefficients **[173]**.

[d] **Represented as "△".**Yarulina et al. (2018) recorded at 160º C, with Emeis's extinction coefficients **[57]**.

[e] **Represented as "◊".** Valecillos et al. (2019) recorded at 150º C, with Emeis's extinction coefficients **[125]**.

[f] Extrapolated data according to the previously described method.

Annex C – Catalytic Activity

Annex C1 – Considerations

Pessanha (2019) calculated 66.2 kJ/mol for the apparent activation energy from Bjørgen's et al. (2007) studies on H-ZSM-5 Si/Al 140 **[88, 130]**. Data was acquired at methanol partial pressure of 0.13 bar, between 290-390º C (constant 16 $kg_{cat}.s/mol_{MeOH}$ space-time) with high particle size (250-420 µm) and low catalyst loadings (60 mg). This study used did not specify reactor dimensions or regime, nor the specific attention for intrinsic kinetics. As it will be explored, product distribution at 375º C was also very different from the present work. This suggests incompatible studies, possible due to experimental conditions.

Studies have determined that DME hydrolysis is meaningly faster than any other reaction, followed by the autocatalytic conversion of oxygenates into olefins (DME kinetic constants with a higher magnitude order than methanol) **[188, 189]**. Moreover, hydrogen transfer reactions become increasingly important as temperature and zeolite aluminium content increase, with an apparent activation energy reported as 93 kJ/mol (Si/Al=90) **[109, 188]**.

The primary formation of ethylene and propylene share very similar formation activation energies, approximately 200 and 210 kJ/mol **[87]**. Speybroeck and her colleagues (2014) in a thorough work on H-ZSM-5 kinetics based on Svelle et al. (2006) experimental studies (Si/Al of 45), identified the methylation of ethylene's activation energy as 1.5 times larger than propylene's (91 kJ/mol and 64 kJ/mol) **[189, 190]**. Butadiene methylation was found with an activation energy of 45 kJ/mol **[189]**. Moreover, the first elemental step of the ring contraction from ciclohexene to the aromatic cycle has lower activation energy (33 kJ/mol) – even though the complete process has higher activation energy barriers **[191]**.

Since these estimations are based on BAS, it is necessary to identify the role of LAS on methanol activation and precursors **[173]**.

Annex C2 – Activity Plots

All kinetic studies used the ANOVA tool in Microsoft Excel (version 16.53). The following table presents the considered data and the retrieved statistic parameters. All calculations were performed according to the methods described in **Chapter 3**.

Table 11 – Catalytic activity (-slope ± St. Error) calculated for H-ZSM-5 Si/Al of 25, 40, 140.

Si/Al	T (º C)	W/F ($kg_{cat}.s/mol_{MeOH}$)	R^2	Slope	St. Error
25	350	2.51, 1.38, 6.26	0.982578	-0.214408	0.020187
	375	1.89, 1.04, 0.55	0.992955	-0.298931	0.017805
	400	1.04, 1.89, 2.25	0.999862	-0.320695	0.002659
40	350	5.49, 2.87, 4.02	0.996801	-0.261739	0.010485
	400	1.09, 2.54, 2.01, 1.65	0.987751	-0.885660	0.056942
	450	1.44, 0.74, 0.44, 1.22	0.984213	-1.104623	0.080773
140	375	5.84, 10.51, 18.75, 28.74	0.998041	-0.047344	0.001211
	400	37.55, 15.08, 10.13	0.998719	-0.045777	0.001159
	450	2.07, 3.47, 20.91, 15.68	0.999459	-0.057839	0.000777

Table 12 – Apparent activation energy ($E_{A,app}$) and pre-exponential factor (k_0) calculated parameters.

Si/Al	T (º C)	Slope	Intercept	$E_{A,app}$ (kJ/mol)	k_0 ($mol/kg_{cat}.s.Pa$)
25	350, 375	-5.369340×10^3	-3,520076	44.64	2.96×10^{-2}
40	350, 400	-1.022663×10^4	4,474146	85.02	8.77×10^{1}
140	375, 450	-1.251404×10^3	-11,716228	10.40	8.16×10^{-6}
	400, 450	-2.277133×10^3	-10,297810	18.93	3.37×10^{-5}

Annex D – Catalytic Studies

Annex D1 – Dual-cycle mechanism reactions

Through **equations (8-18)** is depicted the main general equations that describe the alkene and aromatic cycle according to the dual-cycle mechanism concept.

Alkene Cycle

Methylation	$C_x + CH_3OH \rightarrow C_{x+1} + H_2O$	$x = [2,6]$	(8)
Cracking &	$2C_x \rightleftharpoons C_{2x}$	$x = 3,4,5$	(9)
Oligomerization	$C_{2x+1} \rightleftharpoons C_x + C_{x+1}$		(10)
	$C_{2x} \rightleftharpoons C_{x-1} + C_{x+1}$		(11)
	$C_{8=} \rightleftharpoons C_{3=} + C_{5=}$		(12)
	$C_{6=} + C_{3=} \rightleftharpoons C_{4=} + C_{5=}$		(13)
	$C_{10=} \rightleftharpoons C_{6=} + C_{4=} \rightleftharpoons C_{2=} + 2C_{4=}$		(14)

Aromatic Cycle

Methylation	$Bz + 3CH_3OH \rightarrow triMB + 3H_2O$	(15)
	$Bz + 4CH_3OH \rightarrow tetraMB + 4H_2O$	(16)
Dealkylation	$tetraMB + 2CH_3OH \rightarrow tetraMB + C_2 + 2H_2O$	(17)
	$tetraMB + 3CH_3OH \rightarrow tetraMB + C_3 + 3H_2O$	(18)

Annex D2 – Conversion Effect

The following figures (**figures 58-60**) depict the experimental results for selectivity, E/Isob, and AA ratios, obtained for H-ZSM-5 with different SI/Al ratios for the tested temperatures

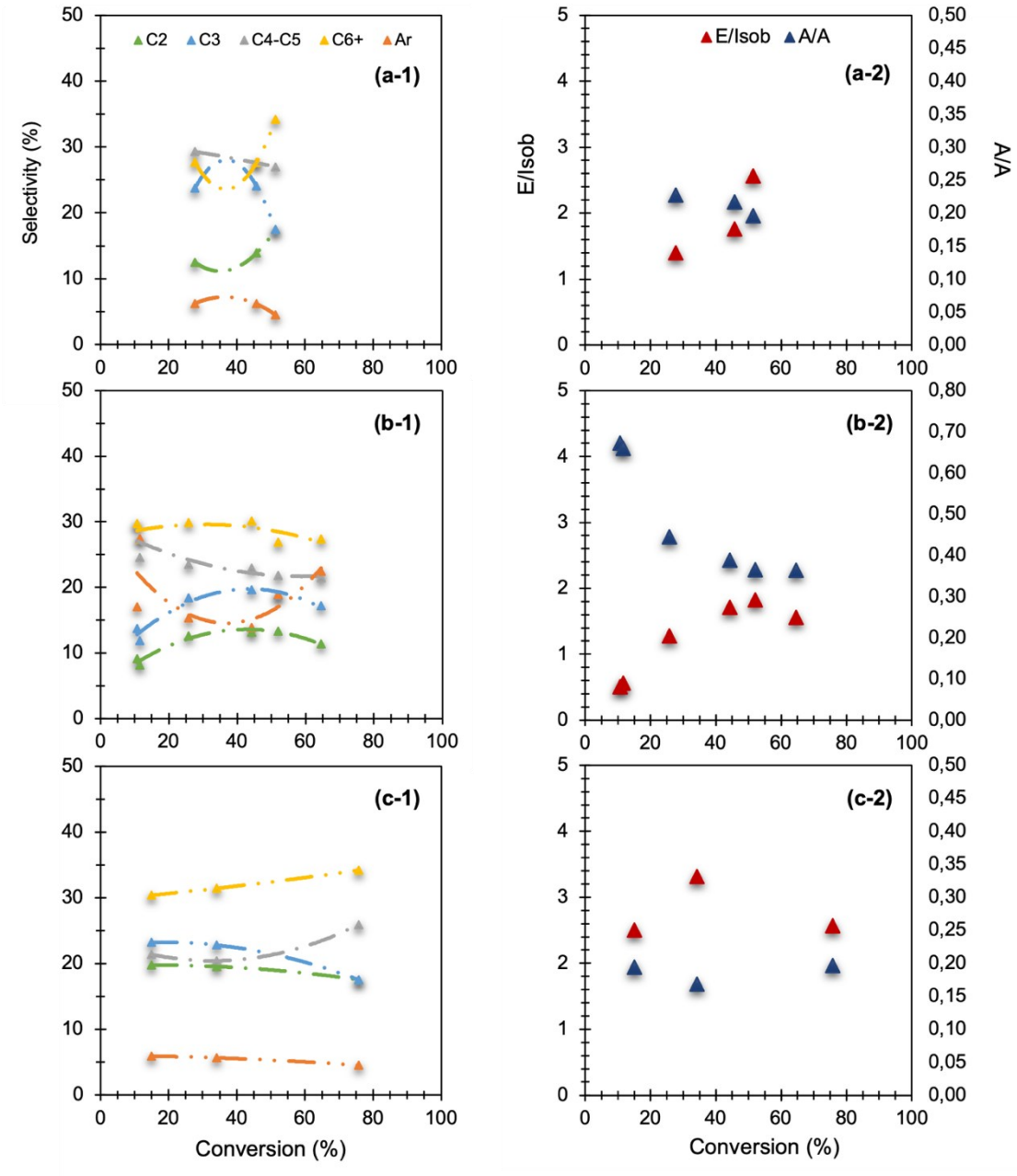

Figure 58 – MTO reaction (/-1) selectivity, (/-2) E/Isob and A/A ratios; as functions of oxygenate conversion for H-ZSM-5 Si/Al of 25 (P_{MeOH}=0.4 bar) at (a-/) 400º C, (b-/) 375º C, and (c-/) 350º C.

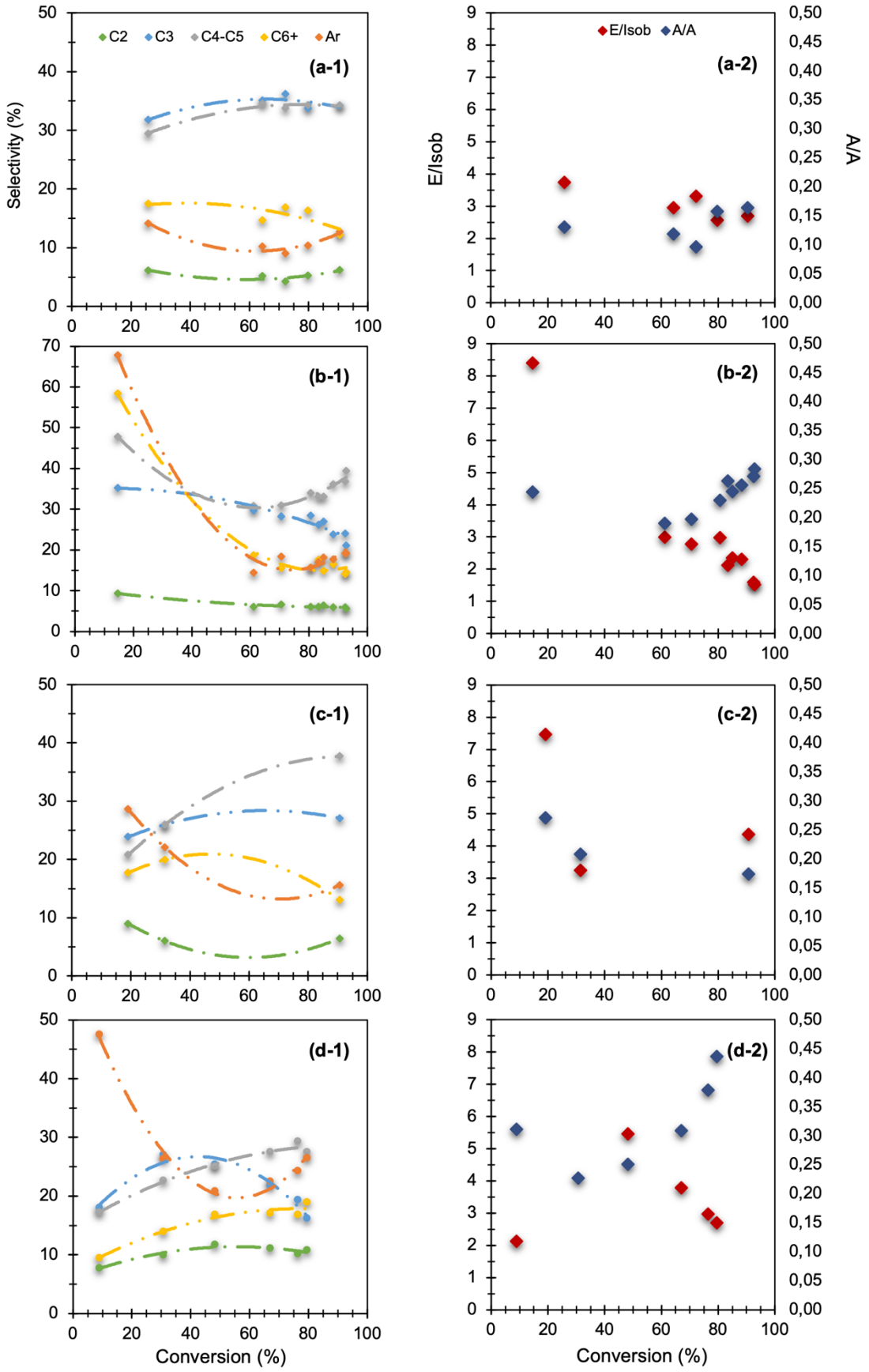

Figure 59 – MTO reaction (/-1) selectivity, (/-2) E/Isob and A/A ratios; as functions of oxygenate conversion for H-ZSM-5 Si/Al of 40 (P_{MeOH}=0.4 bar) at (a-/) 450° C, (b-/) 400° C, (c-/) 375° C, and (d-/) 350° C.

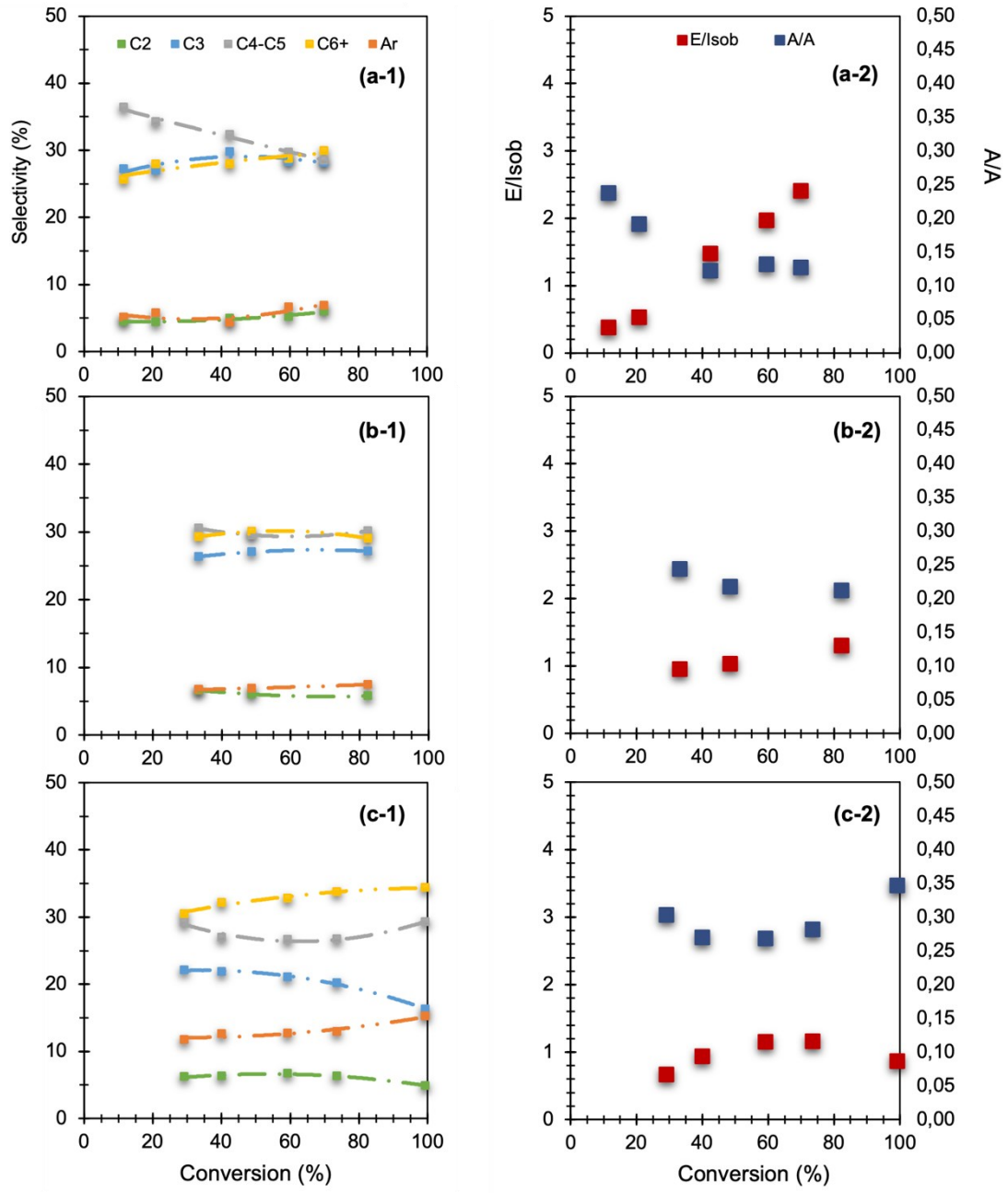

Figure 60 – MTO reaction (/-1) selectivity, (/-2) E/Isob and A/A ratios; as functions of oxygenate conversion for H-ZSM-5 Si/Al of 140 (P_{MeOH}=0.4 bar) at (a-/) 450° C, (b-/) 400° C, and (c-/) 375° C.

Annex E – Reformulations (After Submission)

Pyridine-FTIR results for S140 at 350º and 450º C were received after the submission of the dissertation. As a result, a reformulation of some of the conclusions presented earlier in this work was necessary. The results for all three catalysts are resumed in **table 13**.

Table 13 – Total active acid site concentrations obtained by py-FTIR for H-ZSM-5 of Si/Al of 25, 40 and 140 at 150º, 250º, 350º and 450º C.

T (º C)	150				250		350		450	
n (µmol/g)	n_{LAS}	n_{BAS}	B/L	n_{total}	B/L	n_{total}	B/L	n_{total}	B/L	n_{total}
S25	31	238	7.6	269	8.5	243	7.6	188	2.5	88
S40	23	214	9.1	238	9.9	217	7.7	178	0.9	48
S140	7	54	7.4	62	7.1	50	4.9	35	0.6	7

Figure 61 represents the graphic interpretation of this data, taking into account the ratio between strong and weak acidity. Strong acidity refers to the active sites present above 350º C, and weak acidity refers to the active sites that are only available at 150º C (difference between total acidity at 150º C and total acidity at 250º C).

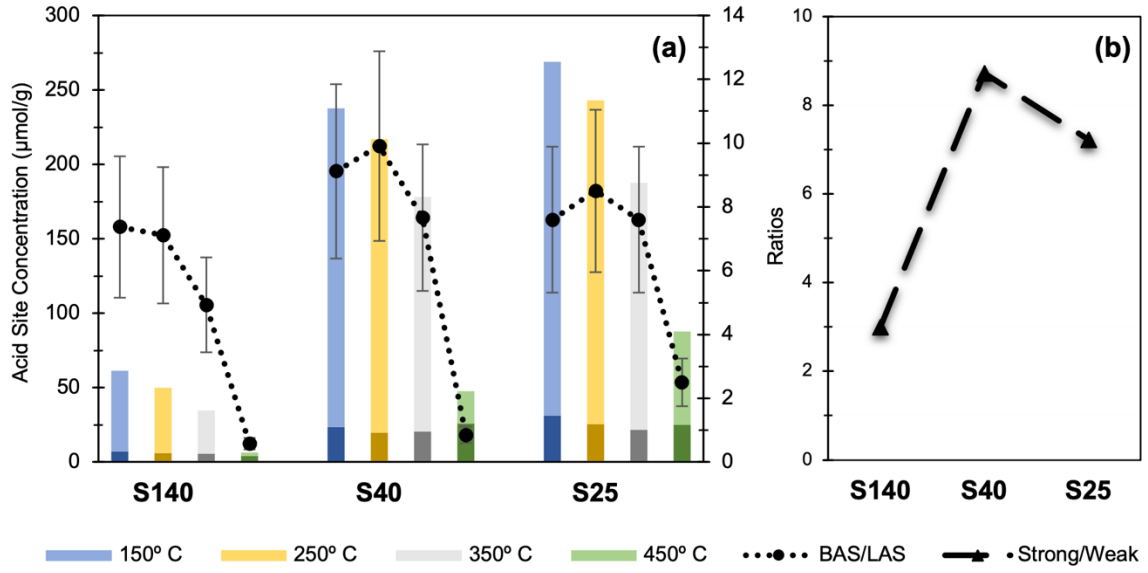

Figure 61 – (a) TAS concentrations (bars, with BAS and LAS referred to with lighter and darker colour) and BAS/LAS ratio (points) from py-FTIR experiments, as functions of temperature and H-ZSM-5 Si/Al ratios. (b) Ratio between strong/weak acidity as a function of H-ZSM-5 Si/Al ratios.

From the analysis of both **table 13** and **figure 61**, it is possible to determine S140's TAS density is over four times lower than S25's. BAS/LAS ratios at 450º C monotonically decrease with increasing Si/Al ratio, contrasting with the hypothesis presented in **Annex B1**. However, the strong/weak ratio presents a maximum for S40, a significant difference in behaviour to be considered for the conclusions in this work.

Accordingly, the findings of this work suggest that the higher strong/weak ratio is responsible for the increased propagation of the aromatic cycle and higher propylene yields, contrasting with the BAS_{strong}/LAS_{total} ratio presented in the conclusions. The similarity between conversion profiles at 375º/400º C were linked to the swift decrease in active acid sites available (transition between medium and strong active acid sites to only strong active sites). This effect was more influential than increasing temperature, thus, the non-verification of an increase in catalytic activity per the expected.

Furthermore, Lewis acidity cannot be directly correlated to the higher apparent activation energy (from aromatization reactions), although several works strongly support this conclusion as stated previously **[183, 184, 187]**. In contrast with the work by Huang et al. (2019), it is concluded that active acid site-reaction-selectivity is not only related to acid site nature but also acid site strength **[118]**. In Huang's work, active strong acid sites were linked to the higher propagation of the aromatic cycle reactions whereas weaker active acid sites were responsible for the promotion of the alkene cycle reactions. Therefore, the compromise between the two effects (acid site nature and strength) should be studied in future work.

Although the structural defective acid sites can no longer be linked to the stabilization of either LAS or BAS, remains valid the conclusion that these defects cause diffusion limitations of product molecules **[182]**. Thus, resulting in catalyst pore blocking and coke deposition, responsible for S25 higher deactivation rate when compared to S40. This effect was not observed by S140 due to the compromise with the higher mesoporosity (which extends catalyst lifetime).

From the works of Khare et al. (2017), higher aluminum content (lower Si/Al) and lower crystallite size, will decrease the average number of interactions between MB and catalyst active sites before these molecules exit the zeolite crystallite **[117]**. These two effects are expressed by the ratio between crystallite size and Si/Al ratio, in which higher values were linked to the propagation of the aromatic cycle relative to the alkene cycle.

In addition to the supplementary quantification of silanol groups and aluminium species (framework and extra-framework) by ^{29}Si and ^{27}Al MAS NMR, it is proposed that crystallite size and particle size distribution are also included in further catalyst characterization studies. The latter can be characterized by either TEM/SEM/XRD techniques in order to determine if all catalysts share similar dimensions. Insight on these properties would confirm that no other phenomena were at play besides the effect of catalyst acidity.